Blackett Laboratory

Imperial College London, United Kingdom

MSci Physics Year in Europe

Project Report

Stuart Higgins

2009

Implementation of a Deceleration Beamline for the Investigation of Charge Exchange Processes using Highly Charged Ions

Diese MSci Thesis wurde angefertigt von Stuart Higgins am
Max-Planck-Institut für Kernphysik, Heidelberg
unter der Betreuung von:

This MSci Thesis was completed by Stuart Higgins at the
Max-Planck-Insitut für Kernphysik, Heidelberg
under the supervision of:

PD Dr. José Ramón Crespo López-Urrutia

Zusammenfassung:

An der Heidelberg Electron Beam Ion Trap (EBIT) ist eine neue Beamline konstruiert worden, sodass Ladungsaustausch zwischen langsamen hochgeladenen Ionen und einem neutralen Gas-target erforscht werden kann. Diese Messungen haben astrophysikalische Relevanz. Das hier vorgestellte Experiment wurde konstruiert, um Ionen aus einer EBIT abzubremsen und den Prozess des Ladungsaustausches zu untersuchen.

Die ionenoptischen Eigenschaften der neuen Beamline und die Eigenschaften des abgebremsten Ionenstrahls sind mit dem Softwarepaket SIMION simuliert worden. Simulationen zeigen, dass die Verteilung der kinetischen Energie der Ionen beim Abbremsen nur wenig verbreitert wird. Die Winkelverteilung nimmt mit steigender Abbremmsspannung zu. Des Abbremspotential, als Funktion vom Fokalabstand, zeigt einen parabolischen Verlauf. Performance-Messungen der neuen Beamline unterstützen die Ergebenisse der Simulation und zeigen qualitiv die ionenoptischen Eigenschaften des neuen Abbremssystem.

Erste Experimente mit Ar^{18+} und Ar^{17+} auf einen neutrales Argon-Target sind erfolgreich durchgeführt worden. K-α Strahlung und Übergänge höherer Ordnung konnten in beiden Fällen beobachtet werden. Der Zerfall des metastabilen $^3S_1$ Zustandes in Ar^{16+} konnte durch Koinzidenz-Spektroskopie als wesentlicher Zerfallskanal identifiziert werden. Die berechneten Hardness-Ratios für die beiden Spektren (0.186 ± 0.010 für Ar^{18+} und 0.090 ± 0.005 für Ar^{17+}) weichen im Vergleich zu Ergebnissen anderer Forschungsgruppen deutlich nach unten ab. Diese Abweichung kann durch den Einsatz der Koinzidenz Technik und den daraus resultierenden unterdrückten Untergrund erklärt werden.

Abstract:

A new experimental beamline has been constructed at the Heidelberg Electron Beam Ion Trap (EBIT) for the investigation of charge exchange processes between slow Highly Charged Ions (HCIs) and a neutral gas target, which are measurements of astrophysical relevance. In order to study this process in detail in the laboratory, the new experiment is designed to decelerate ions extracted from the EBIT.

The ion optical properties of the new beamline and the properties of decelerated ions have been simulated using the program SIMION. Simulations show that ions are decelerated without any major broadening of their kinetic energy distribution, whereas angular distribution increases with deceleration voltage. The deceleration potential as a function of focal distance is shown to follow a parabolic relationship. Performance tests of the new beamline support the results of the simulation and qualitatively demonstrate the ion optical-like properties of the deceleration system.

First experiments with Ar^{18+} and Ar^{17+} incident upon a neutral argon target have been successfully completed, with the observation of the K-α peak and higher order transitions in both cases. The decay of the metastable state $^3S_1$ of Ar^{16+} could be identified as an important decay channel using coincidence spectroscopy. Calculated hardness ratios for the spectra (0.186 ± 0.010 for Ar^{18+} and 0.090 ± 0.005 for Ar^{17+}) are lower than those found in previous experiments by different groups. This deviation is most likely a consequence of lower background events as a result of the coincidence spectroscopy technique employed.

Contents

Chapter 1

Introduction

On January 30th, 1996 the Röntgen Satellite (ROSAT) observed X-ray emission from the Comet Hyakutake C/1996 B2, the first known detection of X-rays from a comet [L$^+$96]. This was initially a surprising discovery as comets are known to be cold objects [Cra02], and so the source of energy for these X-ray emissions was unclear. It was then proposed later that year, by Lisse et al. [L$^+$96], that the source of these X-rays was from charge exchange reactions between neutral molecules and elements in the comet's coma (a mixture of organic compounds such as H_2O, CO, and CO_2) and Highly Charged Ions (HCIs) from the solar wind.

HCIs are one of the most abundant types of visible matter in the universe [HFB97]. In the laboratory they are particularly useful, as they can be used to study many radiative and collisional processes [BS03], such as those found in astrophysical plasmas. In this project, the charge exchange process, whereby an HCI captures one or more electrons from a neutral atom, was investigated using neutral and highly charged argon. The capture, as discussed later, is most likely into a highly excited state, which subsequently decays in a cascade to the ground state. The last transition in this de-excitation process emits a photon in the X-ray range.

Subsequent observations [L$^+$01, KCK$^+$02] and experiments in the laboratory by Beiersdorfer et al. [B$^+$03], and Allen et al. [ABR$^+$08] have added evidence that charge exchange reactions are likely to be predominate cause of X-ray emission from comets. There are however discrepancies between laboratory results obtained by similar experiments[1], highlighting the need for further data. Recent astrophysical papers [KLR$^+$09] again state the requirement for further atomic data about charge exchange processes, for conditions similar to those found in the solar wind. This information is required to interpret astrophysical spectra, allowing a better understanding of the composition of the solar wind and the conditions surrounding comets.

As a result of this demand, a new experiment at the Heidelberg Electron Beam Ion Trap (EBIT) was proposed. An EBIT is a machine that allows the generation of a wide range of HCIs, reaching charge states as high as U^{92+} [MEK94]. Whilst other production techniques for ions exist, such as the Electron Cyclotron Resonance Ion Source (ECRIS), an EBIT has the advantage of being able to provide a highly stable source of ions, with well defined (typically less than $\pm$ 10 eV/q) kinetic energies over a large range of charge

---

[1]Discussed further in section 2.

states [Bei08]. The EBIT is discussed later in further detail in section 3.1.

The new experiment is designed to reduce the kinetic energy of ions produced by the EBIT. In the solar wind, HCIs travel at speeds of between 200 and 800 km/s [WBB08], which corresponds to kinetic energies of 0.2 - 3.3 keV/amu, much slower than those extracted from the EBIT. This is important, as the quantum l as well as the n state into which an electron is captured during charge exchange is dependent upon the collision energy of the projectile and target atoms [BMN86]. An electron involved in higher energy collisions is often captured into states with a non-zero angular momentum l. This affects the decay pathways available to the electron, and hence the wavelengths and energies of emitted photons (discussed later in greater detail in section 2.2). As of 2002, fourteen such comets had been discovered emitting X-rays [Cra02], some from further studies of the ROSAT data [DET97] and, as in the case of Comet C/LINEAR 1999 S4, from newer searches of data from the Chandra and XMM-Newton missions.
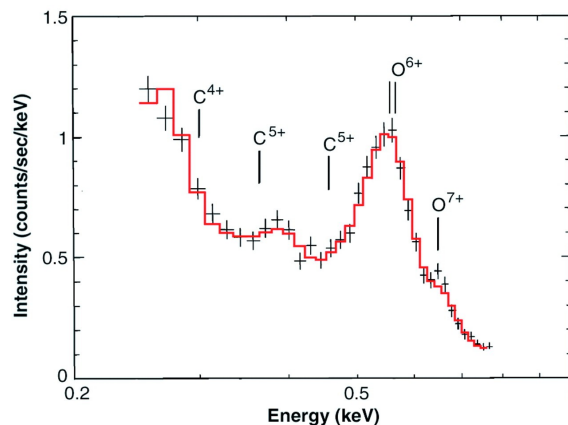
Figure 1.1: Chandra ACIS spectrum for Comet C/LINEAR 1999 S4, from a review of X-ray emission from comets, adapted by Cravens [Cra02] from the work of Lisse et al. [L+01], © The American Physical Society.

Figure 1.1 shows the spectrum of Comet C/LINEAR 1999 S4 as observed by the Advanced CCD Imaging Spectrometer (ACIS) on-board the Chandra satellite. In 2001 this provided the first observation of distinct X-ray emission lines in a spectrum, which were unresolvable for Comet Hyakutake C/1996 B2.

In this project argon was chosen to provide both the incoming projectile ion and the neutral target gas for the first charge exchange experiments. Whilst argon is found in relatively low abundance in the solar wind [G+04], it is well understood and relatively easy to use with EBITs [Tra05]. Argon has also been used in previous experiments by Beiersdorfer et al. and Allen et al. providing a benchmark for the data obtained here. As these were the first measurements to be made with the new experiment, in comparison to existing data they give an indication of the performance of the setup, as well as providing further evidence to help resolve current discrepancies.

In summary the main roles of this project were:

- to construct and install a new experimental beamline at the Heidelberg EBIT, designed to decelerate ions from the EBIT down to 10 eV/q,

- to simulate the ion optical properties of the beamline to provide data for optimising the beamline's performance,

- to collect experimental data on the performance of the beamline,

- to use a decelerated argon ion beam to investigate charge exchange processes between highly charged ions and neutral argon atoms, similar to the reaction of ions in the solar wind interacting with the coma of comets and planetary atmospheres.

Chapter 2

Theory

2.1 Classical Over-Barrier Model

The main mechanism studied in this project is charge exchange between a hydrogen-like or bare HCI with a neutral gas atom. An HCI, in close enough proximity to a neutral atom, is able to capture an electron from the atom into a high energy level. This state then subsequently decays via photon emission in a two stage process

$$
\begin{aligned}
A^{q+} + B &\rightarrow A^{(q-1)*} + B^+ \\
A^{(q-1)*} &\rightarrow A^{(q-1)} + h\nu
\end{aligned}
\tag{2.1}
$$
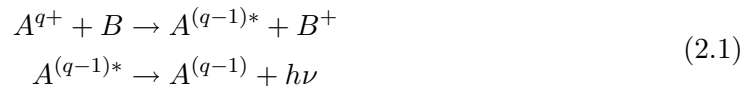
where A is the incident HCI with charge state q, the $*$ indicates the excited state of the ion before it decays, B is the neutral target and $h\nu$ is the emitted photon. In this treatment only single electron capture is considered. It is also possible for multiple electron capture to occur, however this cannot be distinguished from single electron capture in this experiment.

This reaction can be described using the Classical Over-Barrier model (COB), developed by Ryufuku et al. in 1980 [RSW80], and later extended by Niehaus [Nie86]. The model gives estimations of the electron capture cross-sections for the charge exchange reactions, that agree well with experimental data (as shown later).

In the model, an electron is bound in a target atomic potential with energy E_b. An approaching charged projectile perturbs this energy level, due to the superposition of the two coulombic potentials. This has the effect of reducing the energy level of the bound electron by an amount proportional to both the charge of the projectile and with the inverse of the separation between them. Formally this can be described as

$$
E^* = E_b - \frac{q}{R}
\tag{2.2}
$$

where q is the charge state of the projectile and R is the internuclear separation of the two nuclei[1].

The effective potential now experienced by the electron in the target atom is given by

$$
V(r) = -\frac{1}{r} - \frac{q}{R-r} \qquad \text{for } r > r_a
\tag{2.3}
$$

---

[1]**Note:** These derivations use atomic units.

where r is the radial distance from the centre of the target nuclei, and r_a is the classical radius of the target. This potential is shown in figure 2.1. The maximum barrier between the target and projectile occurs when the derivative of this potential is zero,

$$\frac{\partial V}{\partial r} = 0 \Rightarrow V_{max} = -\frac{(1+\sqrt{q})^2}{R} \ . \tag{2.4}$$

The electron remains bound in the target atom until $V_{max} = E^*$ giving

$$\begin{aligned}
E_b - \frac{q}{R} &= -\frac{(1+\sqrt{q})^2}{R} \\
&= -\frac{1+2\sqrt{q}+q}{R} \\
\Rightarrow E_b &= \frac{q}{R} - \frac{1}{R} - \frac{2\sqrt{q}}{R} - \frac{q}{R} \\
\Rightarrow E_b &= -\frac{1}{R}(1+2\sqrt{q}) \\
\Rightarrow R &= \frac{1+2\sqrt{q}}{E_b} \equiv R_1 \ .
\end{aligned} \tag{2.5}$$

Radius R_1 is a condition stipulating the distance at which the electron can move freely between the two nuclei, forming a quasi-molecular system. The geometrical cross-section for this process is given by

$$\sigma_{R_1} \approx \pi R_1^2 \ . \tag{2.6}$$

However this does not necessarily mean that the electron will eventually remain trapped in the projectile potential. In the frame of the projectile, the electron has an initial kinetic energy of

$$E_{kin} = \frac{1}{2}\nu_p^2 \tag{2.7}$$

where ν_p is the velocity of the projectile.

If this kinetic energy is greater than the target nucleus' coulombic potential then an electron will not remain captured, but will be ionised to the continuum, as a result of the conservation of energy. This gives a second constraint on the radius,

$$\begin{aligned}
E_{kin} &= V_{proj} \\
\Rightarrow \frac{1}{2}\nu_p^2 &= \frac{q}{R} \\
\Rightarrow R_2 &= \frac{2q}{\nu_p^2}
\end{aligned} \tag{2.8}$$

where V_{proj} is the potential of the projectile.

This gives a further cross section of

$$\sigma_c \propto \pi R_2^2 = \pi \frac{4q^2}{\nu_p^4} \tag{2.9}$$

which drops inversely with the fourth power of the projectile's velocity.

This behaviour of the cross section is well supported experimentally [KHH81], as shown in figure 2.2. Importantly, the cross-section for electron capture remains constant up to
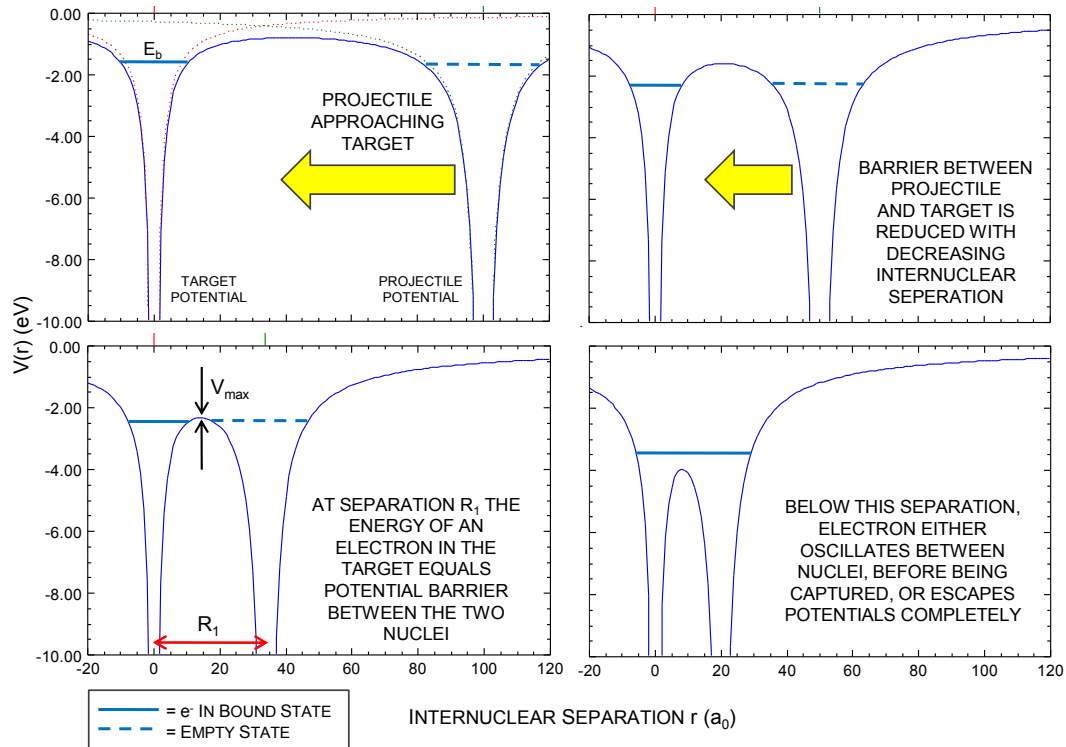
Figure 2.1: The effect of an approaching HCI on the coulomb potential surrounding a neutral target atom. The energy levels shown here are arbitrary. The potential field graphs are adapted from the work of Aumayr [Aum09].

approximately 10 keV/amu (standardised to the ions charge state). So for the collision experiments being carried out here (in the range of 0.2 - 3 keV/amu), the cross-section for capture into the projectile is proportional to the projectile's charge state q. Numerically this cross section is approximately $\sigma_c \approx q.10^{-15}$ cm^2, as shown in the figure.

2.2 Angular Momentum Considerations

The model so far however, fails to consider into what n-state an electron would be captured. This can be estimated as

$$n_c \approx \frac{q^{3/4}}{\sqrt{\frac{E_b}{13.6}}} \approx 8 \tag{2.10}$$

for argon [GWSC01], which has a ionisation potential of 15.8 eV for the outermost electron of a neutral atom [CL78]. However this again only considers the n quantum state into which an electron could be captured, not taking into account the possible angular momentum states, which can take the possible integer range from $0 \rightarrow (n-1)$.

The Classical Over-Barrier model was modified again by Burgdörfer et al. [BMN86] in 1986 to include a description of the angular momentum distribution of electrons captured by highly charged projectiles. Further studies by Dijkkamp et al. [DGB+85] and Janev
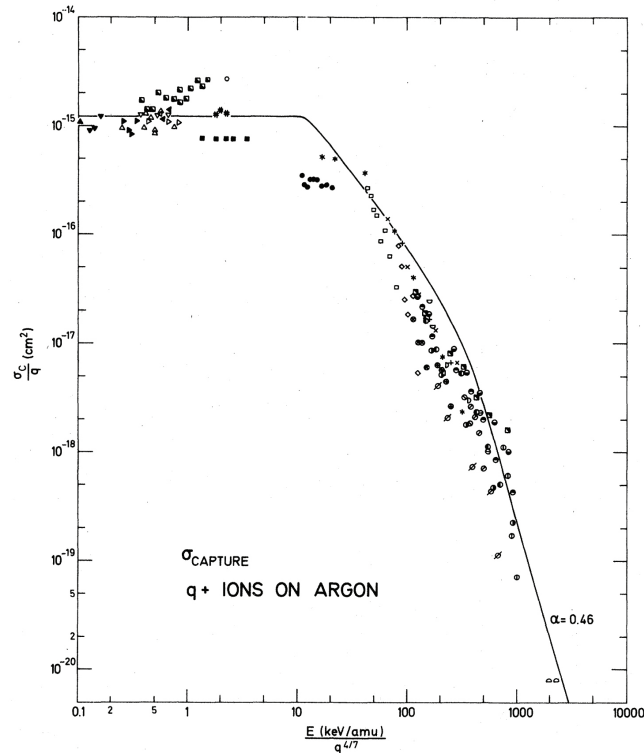
Figure 2.2: Experimentally observed, standardised cross sections for q^+ ions incident upon argon. Figure taken from a review of capture cross sections by Knudsen et al. [KHH81].

& Winter [JW85] showed that the distribution of l-states for capture into an n-shell is highly dependent upon the incident projectiles collision energy. A low incident energy means that the electron has not enough energy to populate higher l-states and that the most probably capture state is $\langle l \rangle = 1$ [BMN86].

The studies mentioned above support models by Otranto et al. [OOB06], which use Classical Trajectory Monte Carlo (CTMC) methods to simulate the l distribution for a captured electron as a function of collision energy, in this case for an O^{8+} projectile incident on H_2O. Figure 2.3 shows how the distribution shifts from high l-states at high 100 keV/amu collision energies down to a distribution predominantly peaked at $l = 1$ for 0.001 keV/amu collisions.

The importance of the l-state manifests itself in the decay pathway taken by the captured electron. Quantum selection rules state that transitions between n quantum states may only take place where the change in l number obeys $\Delta l = \pm 1$. An electron captured during a high energy collision, is more likely to have an $l > 1$, due to rotational coupling [BMN86]. This electron is then forced to cascade down to the 2p ($n = 2$, $l = 1$) state before undergoing the K-α[2] transition from the 2p $\rightarrow$ 1s ground state, as shown in figure 2.4. The cascade transitions typically occur in the visible, Vacuum Ultra Violet (VUV) and Extreme Ultra Violet (EUV) energy range, whereas the K transitions lie in

---

[2]In this project Lyman-α,-β, etc transitions in hydrogen-like systems are referred to as K-α transitions for consistency and clarity.
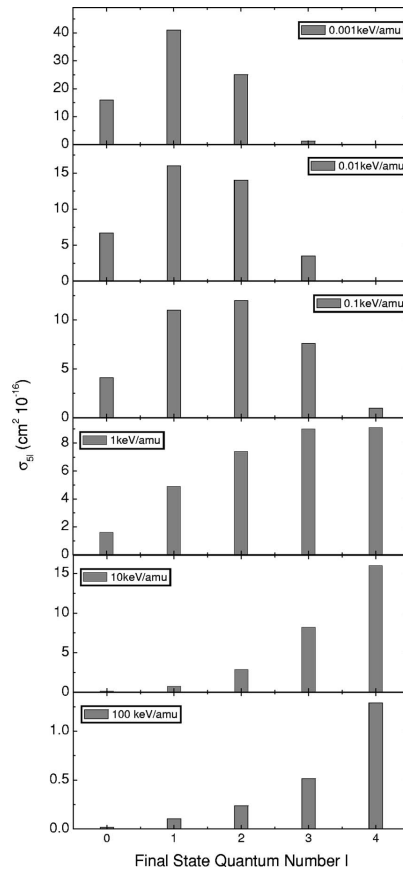
Figure 2.3: CTMC calculation of the electron capture cross sections into five l-states for O^{8+} incident upon H_2O, for different collision energies. From the work of Otranto et al. [OOB06], © The American Physical Society.

the soft X-ray range. Electrons captured during low energy collisions into the $l = 1$ state can decay directly into the 1s state, resulting in the emission of higher order K lines, as shown in the simulated emission cross sections by Otranto et al. in figure 2.5.

Unfortunately, experimentally it is not always possible to resolve the individual higher order K transitions (K-β, K-γ, etc) in X-ray spectra, due to the limited energy resolution of the detector. However a so-called hardness ratio can be calculated to allow quantitative comparison between spectra. This ratio is defined as

$$\mathcal{H} = \frac{\sigma_e \ (np \to 1s)}{\sigma_e \ (2p \to 1s)} \qquad \text{for} \qquad n > 2 \qquad (2.11)$$

where σ_e is the emission cross section for the respective transitions. In the experimental spectra this is seen as the relative intensities of the spectral peaks.

2.3 Discrepancies in Existing Data

Otranto et al. have used their CTMC model for the l distribution of electron capture to estimate the hardness ratio as a function of collision energy. Whilst this model matches well
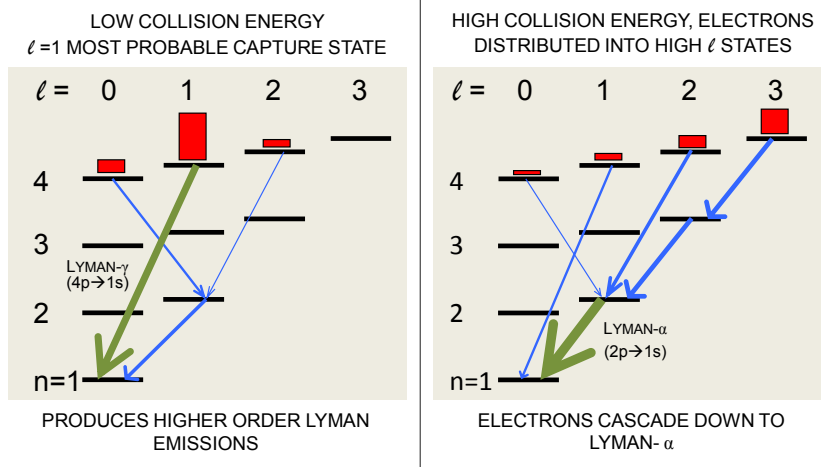
Figure 2.4: Illustration of the difference in the angular momentum probability distribution of a captured electron and the subsequent effect this has on the radiative decay pathway. Figure adapted from Wargelin et al. [WBB08].
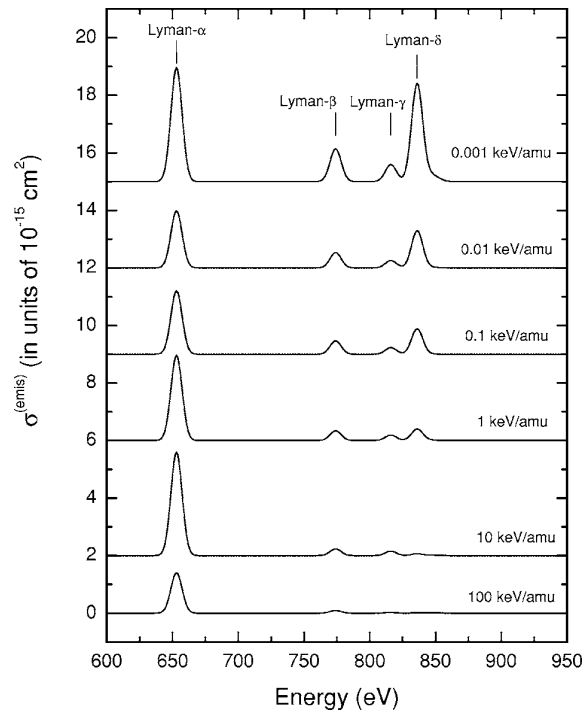
Figure 2.5: CTMC calculations of the emission cross-sections for one electron capture by O^{8+} projectiles from a hydrogen-like system, for decreasing collision energy. The baselines for the 10 keV/amu and above collisions are shifted for better viewing, originally lying at 0 on the y-axis. Figure from Otranto et al. [OOB06], © The American Physical Society.

with the data of Beiersdorfer et al. (at Lawrence Livermore National Laboratory) [B$^+$03], and that of Greenwood et al. (at Queen's University Belfast) [GWSC01], it remains at odds

with similar experiments conducted by Allen et al. (at Humboldt-Universität in Berlin) [ABR$^+$08].

Allen et al. express caution in using the CTMC model to interpret astrophysical observations, believing that its rate at which the hardness ratio increases with decreasing collision energy is exaggerated [ABR$^+$08]. Experiments with Ar^{18+} ions in Berlin show good agreement with the CTMC model, however for Ar^{17+} the hardness ratios are approximately half of the predicted value.

This discrepancy in results, plus the requirement for more and better atomic data for the astrophysical community show the need for further experiments in this area, to better clarify how these processes work. As mentioned in the introduction, the experiments completed here aimed to re-create those under discussion, as well as to provide comparative to assess the performance of the new beamline.

Chapter 3

Experimental Method

This chapter follows the progression of ions through the entire experimental setup, from formation in the EBIT, through to extraction and selection of the desired ion species, before being transported through to the deceleration beamline. Figure 3.1 shows an overhead view of the experiment to show the layout of the different sections of the experiment, as described here. In the later part of this chapter the deceleration beamline is discussed in detail, along with the detectors and equipment used during experiments. The final section contains the explicit method used to observe charge exchange reactions, however before this can be achieved, there are a significant number of intermediate steps, all beginning with the EBIT.

3.1   The Electron Beam Ion Trap (EBIT)

The first EBIT was constructed at the Lawrence Livermore National Laboratory in the USA, and entered service in the autumn of 1986 [LMH$^+$88]. The EBIT, a further development of the Electron Beam Ion Source (EBIS) [Don97], was originally conceived to be a source of X-rays, emitted from any desired HCI, which is not possible with an EBIS, due to the physical constraints of the design.

Since the invention of the EBIT, many experiments were developed that utilise this source for studying the interactions of HCIs with solids, gases, and photons in greater detail [Bei08]. Some interactions can be studied in situ, whilst the ions are still contained within the trap, however ions can also be extracted from the EBIT for transport into other experiments, or to do analysis on the trap contents.

Figure 3.2 shows a simplified schematic of the EBIT apparatus in used at the Heidelberg EBIT[1]. An electron beam, emitted from the cathode of an electron gun, is accelerated towards the trapping region by an electrostatic potential. As it does so the beam is highly compressed by an 8 Tesla magnetic field, generated by a pair of Helmholtz superconducting coils. This field compresses the electron beam to below 50 μm in diameter, giving an electron beam density of up to $\approx$ 12,000 A/cm^2 for the Heidelberg EBIT [Mar05]. This high density beam collides with atoms inside the trapping region, which are ionised by

---

[1]In this report the term EBIT refers to the high-energy, cryogenic generation of EBITs, such as the Heidelberg EBIT. Other types of EBIT exist, which operate under different conditions and have varying designs [C$^+$09, LMH$^+$88].
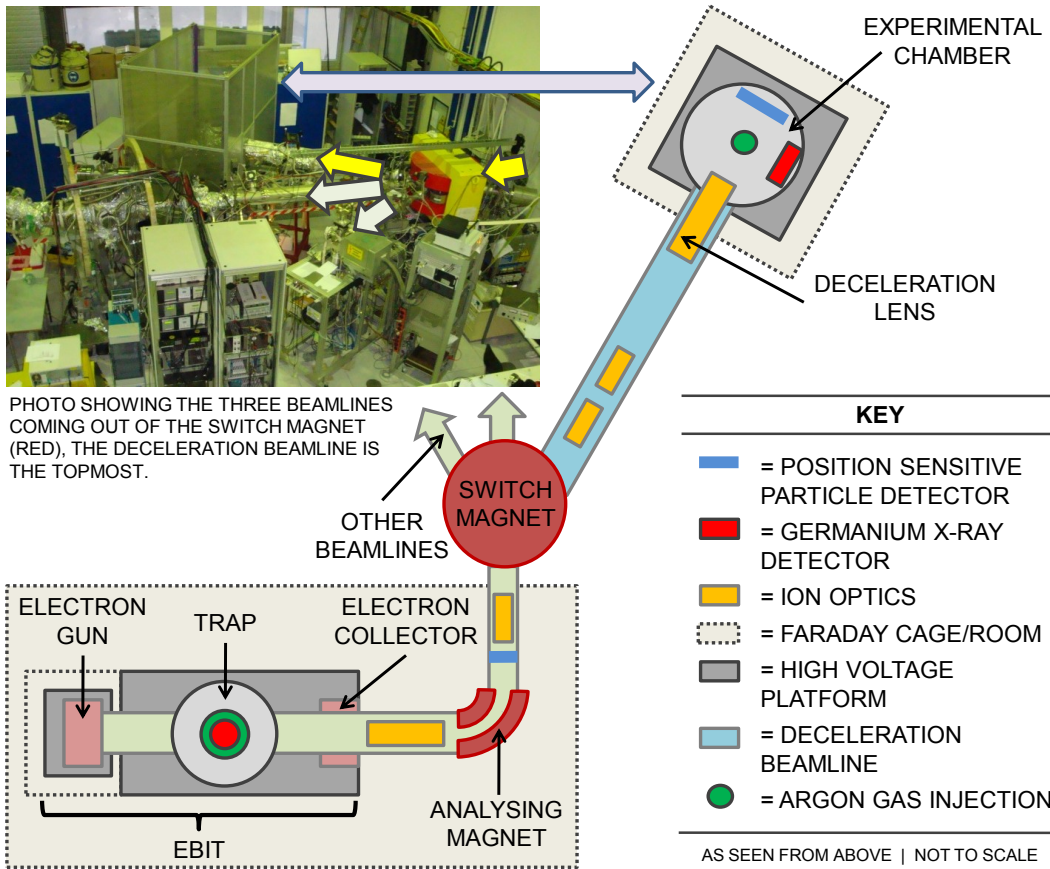
Figure 3.1: Overview of the entire experimental setup. The photo is provided to give a sense of scale for the beamline. The EBIT is not shown in the photo, but is housed in an adjoining Faraday room.

successive electron impact. The electron beam then passes out of the trap where it is decelerated into the electron collector, and is subsequently dumped onto the inner walls of this cylindrical electrode.

Inside the trap atoms are ionised stepwise continuing up until an equilibrium is reached between the rate of electron impact ionisation and loss processes within the trap. The three main ion loss processes within an EBIT are radiative recombination (RR), dielectric recombination (DR) and charge exchange due to ion-atom collisions within the trap[2].

The produced ions are confined axially within the trapping region by an electric potential produced by nine cylindrical electrodes mounted within the superconducting coils. These so-named *drift tubes* have different diameters, as shown in figure 3.3, which form a shallow trapping potential when a voltage is applied to them. This potential can be altered independently, allowing control over the trap depth and the shape of the poten-

---

[2]Whilst RR and DR are important processes in understanding the inner-workings of an EBIT, they are not directly relevant to this work, and are not discussed in depth here. Descriptions of these processes can be found in the book of Beyer and Shevelko [BS03], which also gives a short introduction to the EBIS and EBIT.
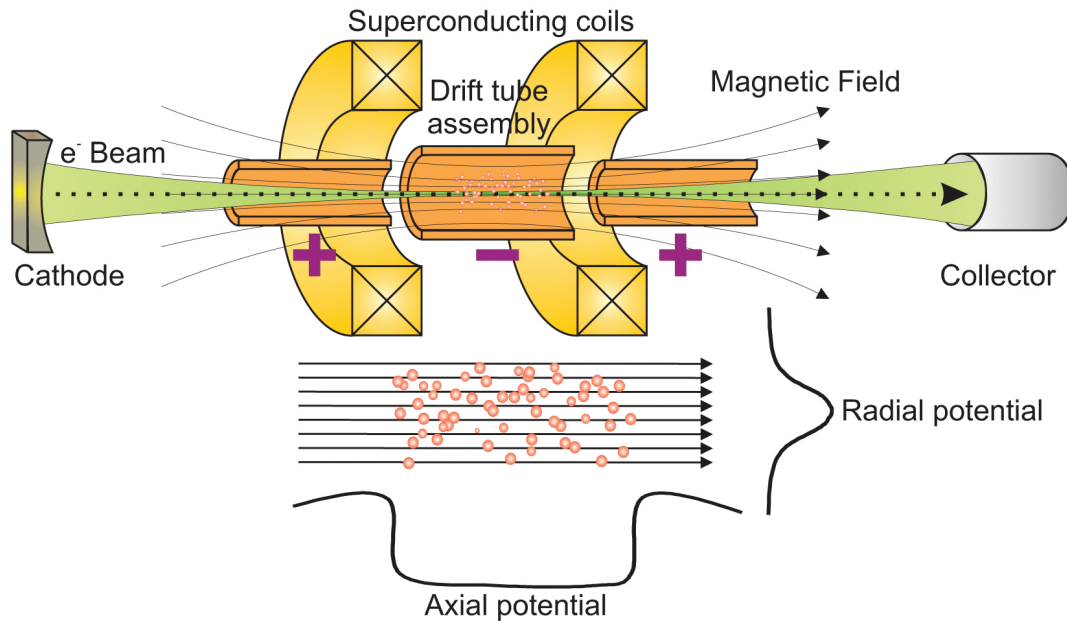
Figure 3.2: Simplified diagram of the basic EBIT principle. Underneath the radial and axial potentials experienced by the ions are also given. **Note:** Only three of the nine drift tubes are shown. Image taken from Bruhns [Bru05].

tials around it. Radially the ions are confined by the negative space charge of the dense electron beam. The magnetic field also provides a weaker radial trapping potential.

Atoms or molecules to be ionised are injected directly into the trapping region using a vacuum leak valve, or after being vaporised by an oven mounted underneath the EBIT. In this project argon 5.0 (99.999% purity) was injected into both the EBIT, to feed the ion production, and into the experiment as a neutral target gas.

The higher the desired charge state, the longer the required ionisation time and the greater the electron beam energy required, as successive ionisations require progressively more and more energy. For comparison the length of time to ionise uranium fully is about 60 s [MEK94], whereas for a lighter element such as argon, as used in this project, the time is significantly less at approximately 300 ms [LU09].

3.1.1   Electron Beam Space Charge

It is important to be able to accurately determine the kinetic energy of the ions extracted from the EBIT as it, along with the magnitude of deceleration, gives the final kinetic energy of the ion used in the charge exchange experiments. Ions gain kinetic energy as they are extracted from the EBIT and accelerated by a +10 kV potential difference between the trapping region and the extraction beamline which is on ground potential, as shown in figure 3.3. The ions have a small excess energy, which is the kinetic energy they possessed prior to escaping the trap, which gives the extracted ion beam a Gaussian kinetic energy distribution, with a FWHM of ± 10 eV/q and a mean value equal to the extraction potential multiplied by the charge of the ion [Bei08].
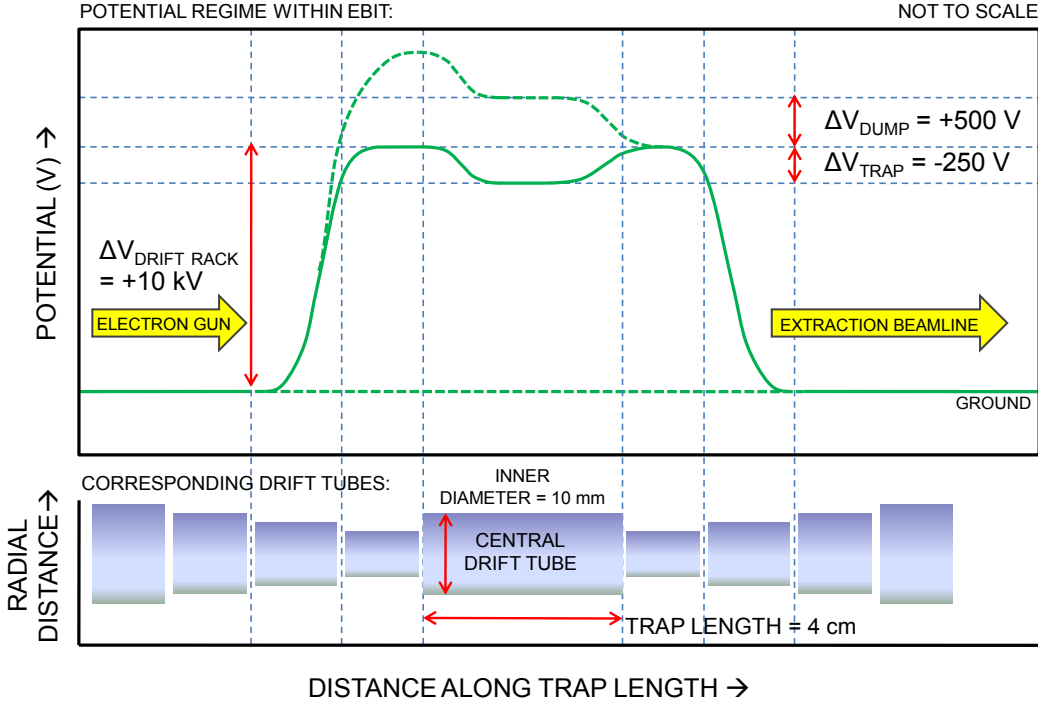
Figure 3.3: The potential field within the EBIT, showing how the whole trapping region can be raised to a higher potential, in this project 10 kV. The dashed green line indicates the momentary (400 ms) potential applied to flush the trap during a dump, described later.

This extraction potential is reduced by the effect of the electron beam space charge. A full derivation of the quantitative estimation of the electron beam space charge is beyond the scope of this project, however some generalised existing equations for EBITs, taken from the work of Currell et al. [Cur00] and González Martínez [Mar05] can be used.

Assuming that the electron beam has a uniform profile distribution along the length of the trap, the electron beam charge density is given by

$$\rho = \frac{I_e}{\nu_e}\frac{1}{A} = \frac{I_e}{\pi r_e^2 \nu_e} \tag{3.1}$$

where I_e is the electron beam current, ν_e is the velocity of the electrons, A is the beam cross-section and r_e is the Herrmann radius, defined as enclosing 80% of the electron beam.

By solving the differential form of Poisson's equation

$$\nabla^2 V = -\frac{\rho}{\epsilon_0} \tag{3.2}$$

it is possible to determine the electric field and potential as a function of r inside the trap. Given the boundary conditions that the potential at the wall of a drift tube must be zero, and is continuous at $r = r_e$, the space charge in Volts at the centre of the trap can be expressed as

$$V_{sp} \approx \frac{30 I_e[A]}{\sqrt{1 - (\frac{E_e[keV]}{511} + 1)^{-2}}} (\ln{(\frac{r_e}{r_{dt}})}^2 - 1) \tag{3.3}$$

where r_{dt} is the inner radius of the central drift tube. An electron beam energy and current of 11.5 keV and 300 mA respectively were used, the radius of the inner drift tube of the Heidelberg EBIT is 5 mm, and the radius of the beam is ≈ 50 μm. The electron beam energy results from acceleration due to the difference in potential of the drift tubes and the cathode (+10 kV and -1.5 kV respectively). The space charge contribution for these parameters is

$$V_{sp} \approx -440 \text{ V}. \tag{3.4}$$

This value is compensated by approximately 20% [Cur00] due to space charge of the ion cloud, giving a corrected space charge reduction of

$$V_{sp}^* \approx -350 \text{ V}. \tag{3.5}$$

Therefore ions extracted from the EBIT during this experiment experience gain a kinetic energy of

$$E_{kin} = qe(V_{dt} - V_{sp}^*) = 9650q \text{ [eV]} \tag{3.6}$$

where V_{dt} is the potential of the drift tube rack relative to ground and q is the charge state of an extracted ion.

3.2 Extracting Ions

Charge exchange experiments can also be carried out directly inside the EBIT, without having to extract the ions first [ABR$^+$08, B$^+$03]. However there is no direct control over many of the experimental parameters. By extracting ions from the EBIT the energy of the HCI projectile is tunable, by varying the retarding potential used to decelerate the ions. A single charge state of the projectile can be selected and investigated, and secondary particles, such as recoil ions and electrons can also be observed. It is therefore highly beneficial to extract ions from the EBIT.

3.2.1 Ion Extraction from the Trap

Ions are first removed from the trapping region using one of two possible techniques: pulsed extraction or continuous extraction, referred to in EBIT literature as *leaky mode*. The latter technique has been developed for EBITs, and uses ions which escape the trapping potential due a normal Maxwell-Boltzmann distribution of particle speeds within the trap. An EBIT operating in leaky mode produces a continuous supply of ions with a well defined energy and low energy spread, as mentioned previously. This is an advantage over the pulsed extraction mode, where the trap contents are frequently flushed by momentarily altering the trapping potentials. This sudden change in potentials gives the extracted ions a much greater kinetic energy distribution, which would increase the experimental uncertainty in the projectile collision energy.

One drawback of this method is the gradual filling of the trap with heavier ions, usually barium and tungsten emitted from the surface of the electron gun cathode. In the case of argon, the barium ions limit the argon charge state that can be achieved before it escapes the trap. Effectively argon gas is being used to evaporatively cool heavy barium ions. This is undesirable as this experiment requires the highest charge states of argon, so to

maintain a continuous levels of Ar^{17+} and Ar^{18+} the trap was periodically emptied, as the rate of argon gas injection is much higher than the flow of heavier elements into the trap. This process, is known as a *dump*, whereby momentarily (400 ms) the potential of the central drift tube is raised by $+500$ V, see figure 3.3. This causes the entire contents of the trap to be expelled, which then flows down the potential gradient towards the extraction beamline. Simultaneously raising the potential of another drift tube, between the gun and trap, helps avoid dumping half the contents of the trap into the electron gun, a process that can damage the cathode.
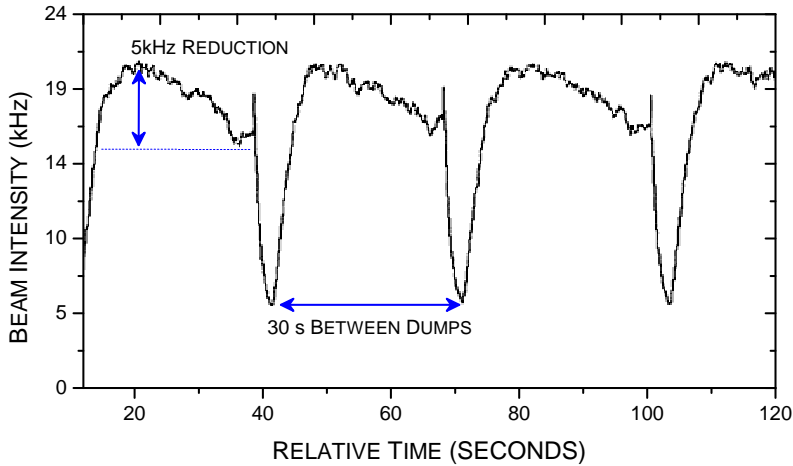
Figure 3.4: Beam count rate as a function of time, showing a dump every 30 seconds.

The dump is controlled automatically using control software, and for this experiment the trap was dumped initially every 30 s, although this was later extended to 60 s. The interval between dumps is justified by monitoring the count rate of argon ions from the EBIT. Figure 3.4 shows the periodic dump of the EBIT, followed by the quick rising escape of freshly ionised argon from the trap. The count rate then begins to slowly decrease over time, due to the filling of the trap once again with heavier elements. This decrease in count rate between dumps is on the order of 5 kHz (compared to a typical peak count rate of 20 kHz) allowing for long dumping time intervals.

3.2.2   Extraction Beamline

Figure 3.5 shows the extraction beamline attached to the Heidelberg EBIT. Ions ejected from the EBIT first pass through two electrostatic ion lenses: a steering and focusing lens (referred to as a Sikler lens); and an Einzel lens, which provides rudimentary focusing. A Micro-Channel Plate detector with delay line anodes, referred to herein as a Position Sensitive Detector (PSD)[3] is mounted directly after a 90° bending magnet. The PSD provides spatial information about detected ions, and the magnet allows the selection of ion species based on their charge-to-mass ratio. A set of apertures before the magnet is used to reduce the beam flux, increasing the resolution that can be achieved by the charge-to-mass analysing system.

---

[3]Further details in section 3.4.1
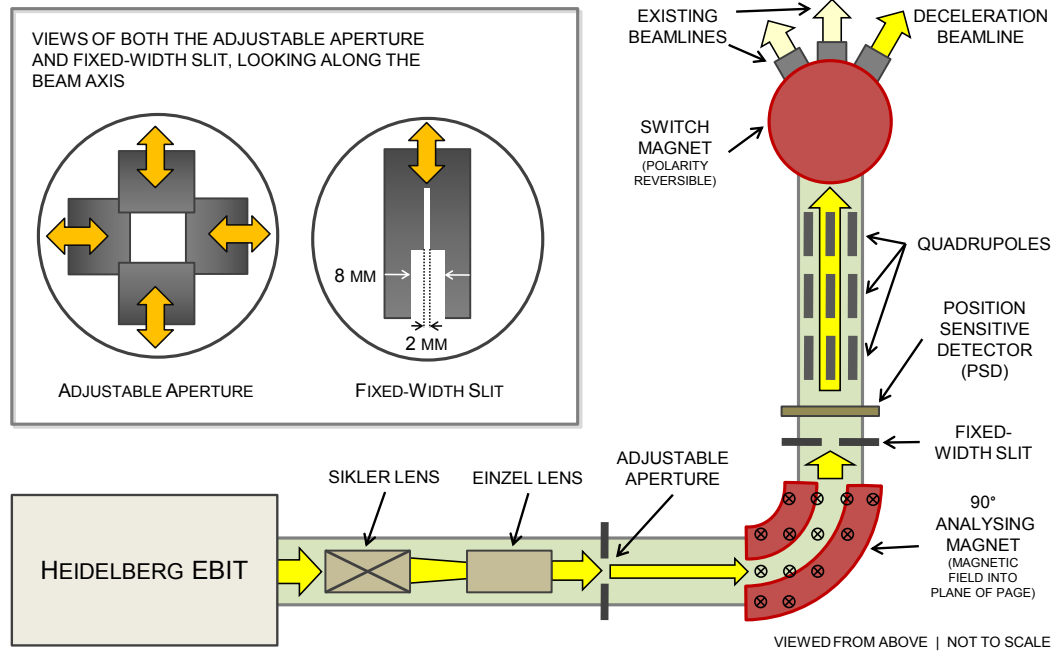
Figure 3.5: Schematic of the extraction beamline attached to the Heidelberg EBIT, with detail of the beam shaping apertures and slits used.

Different ion species can be isolated from the beam leaving the EBIT by varying the strength of the bending magnet. The magnetic field strength is controlled by changing the amount of current passing through coils wound around an iron core, which form an electromagnet. Charged particles entering the magnet experience the Lorentz force, the strength of which is directly proportional to the particles charge and its velocity, as given by[4]

$$\vec{F} = qe(\vec{E} + \vec{\nu} \times \vec{B}) \tag{3.7}$$

where $\vec{F}$ is the force on the particle, q is the particle's charge state, e is the elementary charge, $\vec{E}$ is the electric field strength, $\vec{\nu}$ is the velocity of the particle, and $\vec{B}$ is the magnetic field strength.

As the electric field within the analysing magnet is zero the equation simplifies to

$$
\begin{aligned}
\vec{F}_{\text{Lorentz}} &= qe(\vec{\nu} \times \vec{B}) \\
\Rightarrow \left| \vec{F} \right| &= qe \left| \vec{\nu} \right| \left| \vec{B} \right|
\end{aligned}
\tag{3.8}
$$

where in the case of the EBIT it can be assumed that $\vec{\nu}$ and $\vec{B}$ are perpendicular, i.e. that particles entering the analysing magnet have no upward or downward component to their velocity.

---

[4]Note that this formula is often written in terms of the total charge of the particle in coulombs, frequently also notated q, however we wish to calculate a charge-to-mass ratio as a dimensionless term.

The ions can also be described as experiencing a centripetal force, with a magnitude given by

$$F_{\text{centripetal}} = \frac{M\nu^2}{r} \tag{3.9}$$

where $F_{\text{centripetal}}$ is the force acting upon mass M, rotating distance r from a point, with velocity ν.

By equating these two forces it is possible to derive a relationship between the charge to mass ratio of an ion passing through the magnet and the magnetic field strength. It follows that

$$qe\nu B = \frac{M\nu^2}{r} \ . \tag{3.10}$$

The velocity ν of the particle entering the analysing magnet can be determined with knowledge of the EBIT operating parameters. Classically

$$E_{kin} = \frac{1}{2}M\nu^2 \tag{3.11}$$

and a particle from the EBIT has an energy

$$E_{kin} = qeU_{EBIT} \tag{3.12}$$

where U_{EBIT} is the extraction potential of the EBIT, minus space charge losses (see section 3.1.1 for further detail). Equating these two expressions gives

$$\nu^2 = \frac{2qeU_{EBIT}}{M} \tag{3.13}$$

Substituting equation 3.13 into 3.10 gives

$$\frac{2U_{EBIT}}{r} = \nu B \ . \tag{3.14}$$

It then follows that

$$\begin{aligned}
\Rightarrow \frac{2U_{EBIT}}{r} &= \sqrt{\frac{2qeU_{EBIT}}{M}}B \\
\Rightarrow \frac{4U_{EBIT}^2}{r^2} &= \frac{2qeU_{EBIT}}{M}B^2 \\
\Rightarrow \frac{q}{M} &= \frac{2U_{EBIT}}{r^2 e B^2}.
\end{aligned} \tag{3.15}$$

Here M is the mass of the particle in kg, whereas we wish to express the ratio with the atomic mass number, denoted m in this derivation. The final stage is then

$$M = mu \tag{3.16}$$

where u is the value of one atomic mass unit in kilograms ($1u \approx 1.66 \times 10^{-27}$ kg), finally leading to

$$\frac{q}{m} = \frac{2uU_{EBIT}}{er^2 B^2} = 7.615\frac{U_{EBIT} \ [\text{V}]}{B^2 \ [\text{G}]} \tag{3.17}$$

where u, e, U_{EBIT} and r are all known. The values used here are given in appendix A.1.

Only ions with the correct degree of deflection will pass through the analysing magnet. If the magnetic field is too weak or too strong the ions may strike an aperture, the magnet or other surfaces within the beamline and be neutralised. Ions that have passed through the analysing magnet are then detected by the PSD, with every ion producing one count. The data acquisition system is capable of assigning every ion hit on the detector its position and corresponding magnetic field. Although the magnetic field is not directly accessible to the data acquisition system, the control voltage of the magnet power supply is. This voltage is a to a good approximation, directly proportional to the magnetic field strength.

By systematically ramping the current passing through the analysing magnet it is therefore possible to scan through the different ion species being produced by the EBIT, thanks to their differing q/m. By recording particle counts according to their position along the direction of dispersion (x-axis), and correlating this with the control voltage applied to the magnet one sees an image such as figure 3.6. Each stripe on the image represents ions with differing q/m. The intensity of the line is related to the relative abundance of the ion species, however in some cases high intensities can also be the result of species with similar q/m passing through the magnet simultaneously. The slant of each line is a result of each ion passing over the finite area of the detector (diameter 40 mm). The line width also gives an indication of the amount of energy broadening of ions from the EBIT, and is also the result of the EBIT not being a point source of particles. The trapping region has a diameter of approximately several hundred μm [Cur00] and a length of ≈ 30 mm.
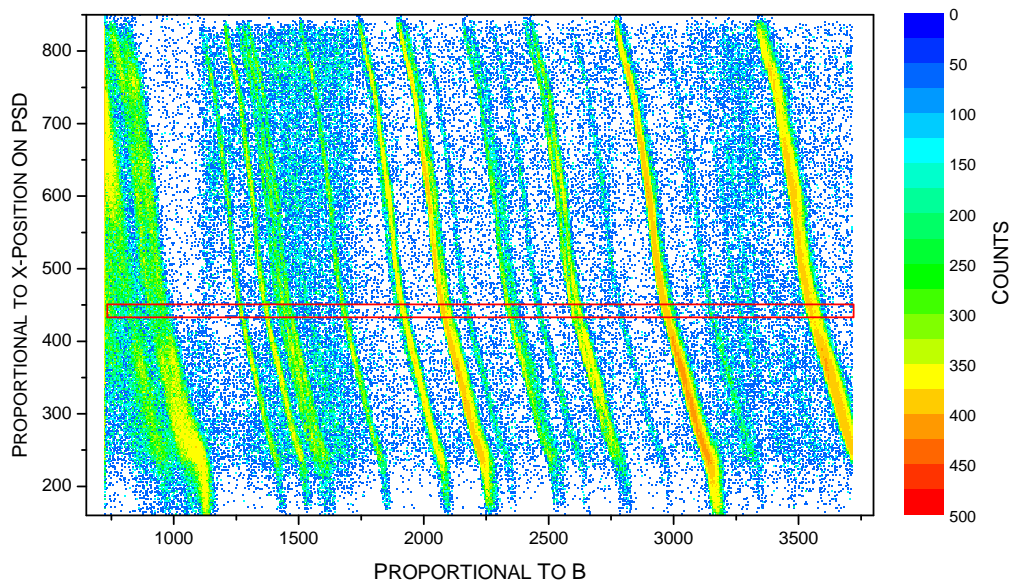
Figure 3.6: Particle counts seen by the PSD as a function of control voltage, which is proportional to the magnetic field within the analysing magnet. The region marked in red, indicates approximately the area projected onto the x-axis in figure 3.7. **Note:** The width and height of this region is exaggerated for illustrative purposes.
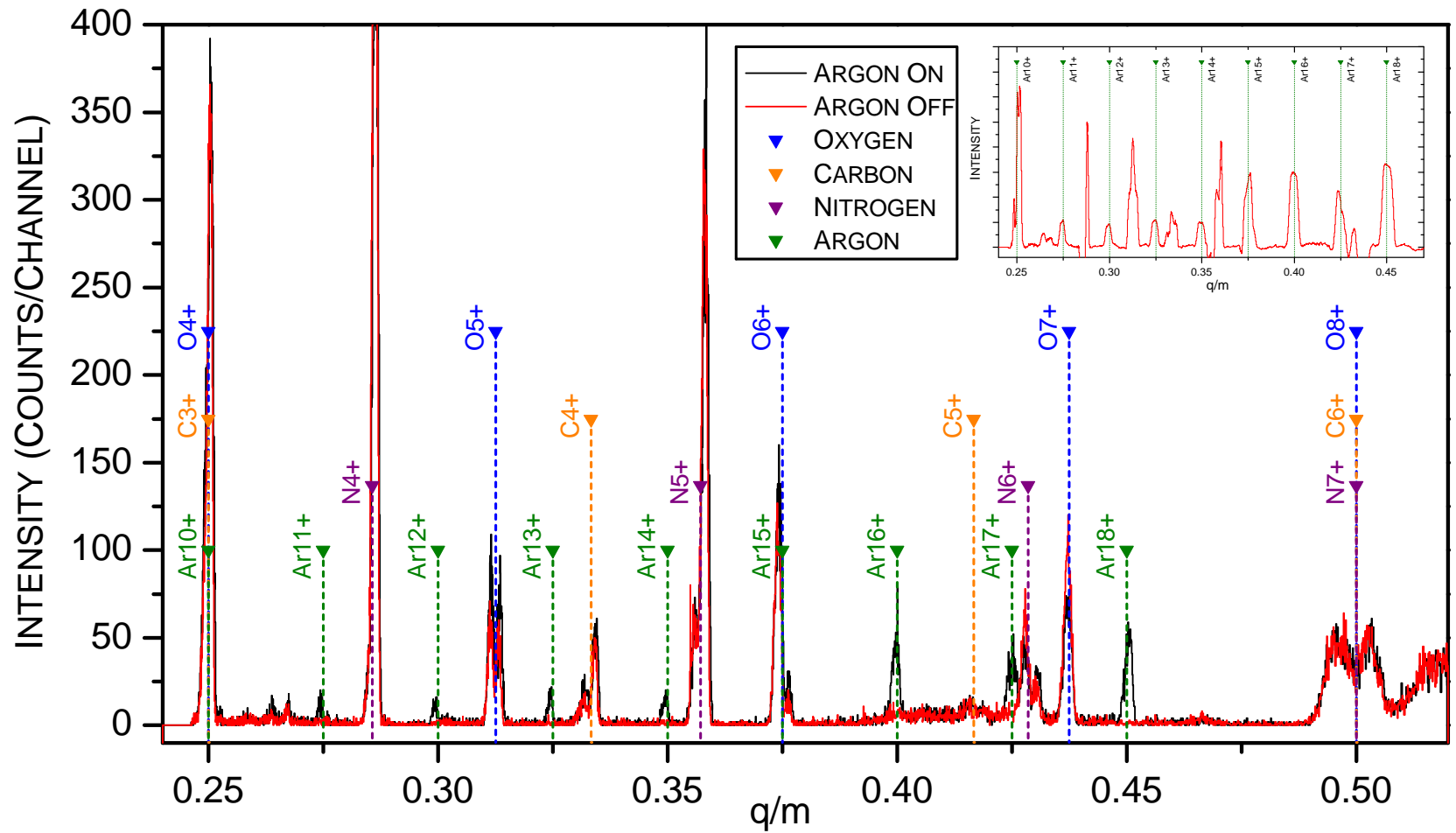
Figure 3.7: 1D information extracted from figure 3.6, used to identify the ion species. The q/m ratios for a number of reference species were theoretically calculated for comparison. The argon ion species are indicated by the peaks which only occur whilst the element is being injected into the EBIT. **Inset:** Difference spectra showing just argon peaks, with some statistical fluctuations.

Once an image such as figure 3.6 has been obtained, a suitable slice of the data can be taken and projected onto the x-axis to produce a spectra, as seen in figure 3.7. Equation 3.17 is used to calibrate the q/m spectra, in conjunction with another derived relationship between the control voltage of the power supply for the magnet and the magnetic field (numerical details in appendix A.1).

Once the peak has been identified, the range of the magnet scan can be reduced to cover a small area around the desired q/m species. The scan speed can also be reduced, and halted directly on top of the peak in the spectra. This is important to maintain good ion count rates through to the experiment. A variable metal slit, that sits directly before the PSD can be used to block other nearby ion species. For example, Ar^{17+} has a very similar q/m value to N^{6+}, with 0.425 and 0.429 respectively. Nitrogen is a common element to find in the EBIT, forming one of the residual gases always present in the system. During the experiment with Ar^{17+} it was possible to stop the majority of N^{6+} from passing through into the beamline by introducing an 8 mm wide aperture in front of the PSD.

Once satisfied that the correct ion species has been identified and isolated the PSD is removed from the beam path (it is mounted on a 100 mm linear manipulator) and the beam passes through a triplet of quadrupoles. The quadrupoles provide another method of focusing the beam before it reaches the experimental beamlines, using equipotential fields generated by four cylindrical rods positioned symmetrically around the beam axis. A single quadrupole is able to focus the beam well in one axis, at the cost of diverging the beam in the other plane, an effect known as astigmatism. Astigmatism is whereby a lens has a different resolving power in two different axis [Sep67], resulting in the incoming rays, or beam in this case, being focused at two different places, depending upon the axis. This causes the average focal point to be broadened, and in terms of an ion beam, results in larger non-circular beam profiles. However a triplet array of quadrupoles can be used to compensate for astigmatism, allowing for effective focusing of the beam[5] [Gre09].

After passing through the quadrupoles the beam enters a switching magnet which, in a similar fashion to the analysing magnet, is used to deflect an incoming charged particles. The strength and polarity of this magnet can be changed to deflect the beam into one of three experimental beamline set at $\pm 30°$, and $0°$ respectively. Once an ion beam has been deflected into the desired beamline, the user's focus can shift to the experimental setup. The EBIT and extraction will deliver an consistent ion beam for almost a week without the need to alter any machine parameters[6].

3.3 Deceleration Beamline

3.3.1 Overview

The deceleration beamline was designed by Rainer Ginzel [Gin09] as a part of his PhD thesis. Construction began in October 2008 and the first successful charge exchange

---

[5]Further detail into how quadrupoles function can be found in the book *Focusing of Charged Particles*, Academic Press, Inc. 1967 [Sep67].

[6]The limiting factor is the liquid helium bath which cools the superconducting magnets. Every 6 days the EBIT has to be shut down and the helium tank refilled.
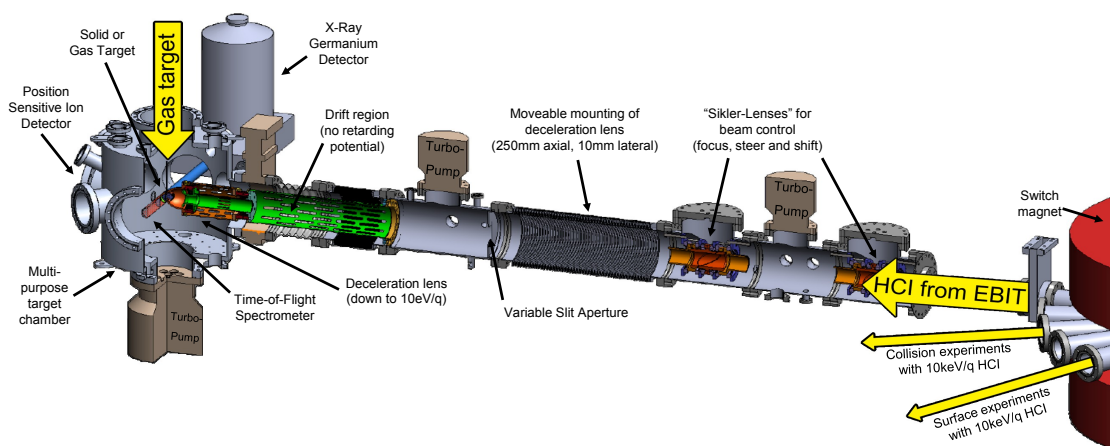
Figure 3.8: The deceleration beamline, as rendered from original CAD drawings, highlighting the important elements of the design. The deceleration lens is shown entering the chamber, green corresponding to electrodes at ground potential, orange to those held at a retarding potential.

experiments were carried out in May 2009. Preparing, installing and testing the beamline were major parts of this project and the work completed.

At its simplest, the deceleration beamline is a ≈ 3 m long vacuum tube which terminates with a 370 mm diameter target chamber, see figure 3.8. As the ions reach the end of the beamline they pass through a 600 mm long, 100 mm outer diameter cylindrical electrode, held at ground potential. This shields the beam from stray electromagnetic fields as it enters into the target chamber. The last 200 mm of the shielding cylinder is narrower in diameter (40 mm) and surrounded by a so-called deceleration lens. A high retarding potential applied to the deceleration lens produces an electrical field gradient that decelerates ions as they enter the chamber (further details in section 3.3.2). A ceramic cylinder electrically isolates the beamline, at ground potential, from the target chamber which is mounted on a high voltage platform. This allows the chamber, all attached detectors and other equipment to be raised to the same potential as the deceleration lens. Ions leaving the lens are therefore not re-accelerated and remain at low kinetic energies.

Figure 3.9 shows the potential experienced by an ion flying through the beamline. With its current configuration, this high voltage platform can be raised to a maximum of $+25$ kV, with the facility of changing the lens potential relative to the platform by ± 5 kV. The final kinetic energy of a decelerated ion changes according to the size of the voltage applied to the platform, and the charge state of of the ion.

In the target chamber are two detectors: a PSD, similar to that used in the extraction beamline, which detects charged incident particles and records their position over a 40 mm diameter area; and a germanium X-ray detector, see section 3.4.2. The detectors are mounted such that the PSD faces the incoming beam, and the X-ray detector is mounted perpendicularly the beam path, a few centimetres back from the target region. A simple schematic of the detector layout is shown later in figure 3.18.

Mounted on top of the target chamber is a three-dimensional translation stage and linear manipulator, which supports the gas target system (section 3.3.2). This system
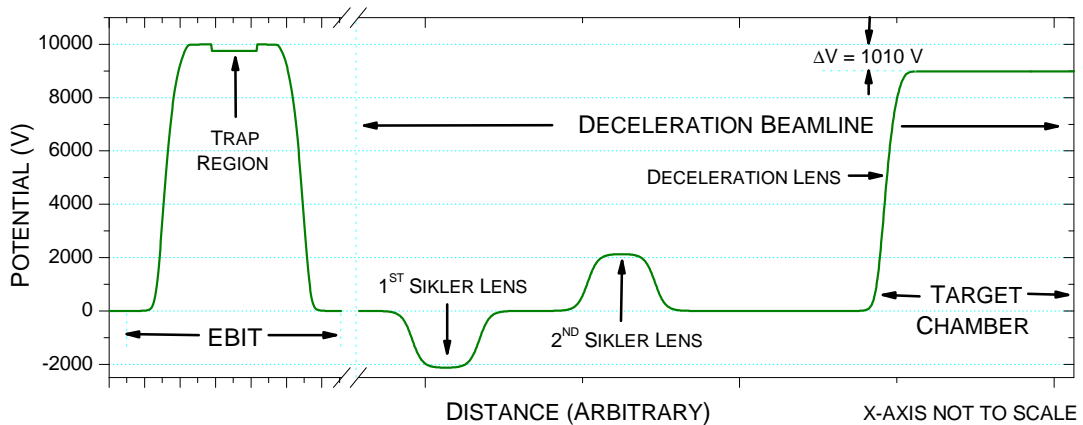
Figure 3.9: Simulation of the potential field felt by a charged particle travelling along the central axis of the beamline, showing the three major variations caused by the two ion lenses and the deceleration lens.

allows a jet of a neutral target gas to be injected directly into the chamber. The position of the tip of the system can be altered in order to optimise the amount of beam incident upon the gas.

Just after the entrance to the beamline are two so-named Sikler lenses, a special type of Einzel lens developed by Gunther Sikler, and later by Rainer Ginzel of the Max-Planck-Institut für Kernphysik, in Heidelberg. These lenses are able to provide preliminary focusing and steering of the incoming ion beam. There is a set of four slits, similar to that used in the extraction system, as shown previously in figure 3.5, used for collimating the beam. The plates are electrically isolated from ground and connected via signal wires to BNC vacuum feedthroughs. Using an electrometer (a highly sensitive type of ammeter) it is then possible to measure currents induced on the plates by an ion beam striking them. This is useful for beam diagnostics, however these plates must remain grounded during normal use, to avoid the possibility of charge accumulating on the plates, which could deflect the beam as well as posing a safety risk to the user.

3.3.2 Detail of the Main Components of the Beamline

Sikler Lens

The beamline is fitted with two ion-optical lenses, so-named *Sikler-Lenses*, the lens is an adaptation of an Einzel lens, which traditionally consists of three cylinders mounted with their central axis aligned to the beam path. By placing the central cylinder at a higher or lower potential relative to the beamline, the potential field within the cylinder acts to focus charged particles entering the lens, see figure 3.10a which shows this effect.

In a Sikler lens however, the central cylinder is twice cut diagonally to produce four electrodes, see figure 3.10b, and then reassembled once again into a cylinder, as shown in figure 3.10c. The voltage applied to these four electrodes can then be altered independently, allowing for example a positive bias to be applied to the left hand side of the lens, which would steer incoming particles to the right (along the orientation of the beam

(a) Electrostatic potential and simulated ion trajectories

(b) Cut electrodes

(c) CAD image of the assembled electrodes
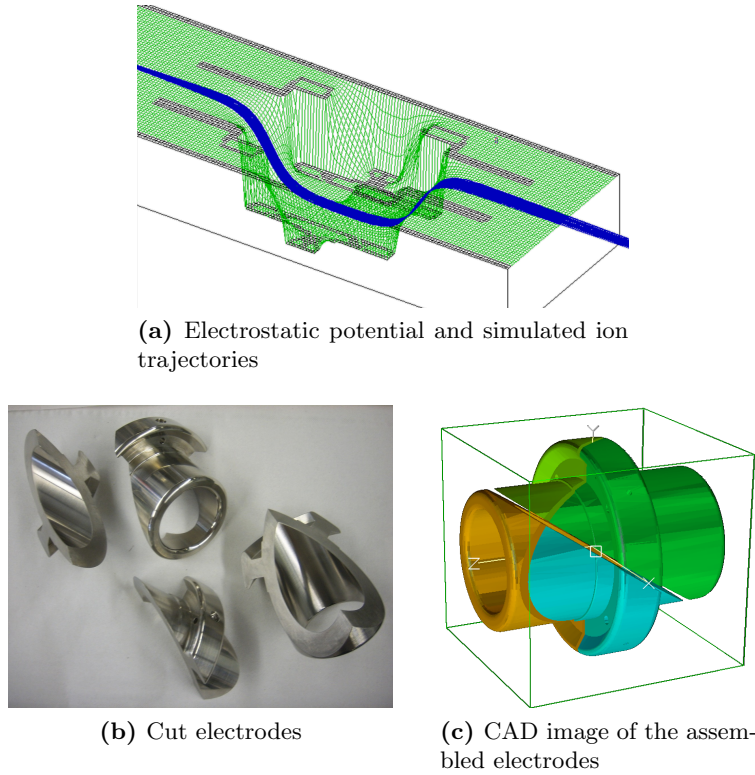
Figure 3.10: The construction of a Sikler lens, note that two further cylindrical electrodes, mounted before and after the central lens, plus the mounting brackets, are not shown for clarity.

axis). This two-dimensional steering of the beam can be performed using small relative differences in the electrode potentials, which all sit on top of a larger focusing potential, thus allowing the beam to be focused and steered simultaneously, as described by

$$U_{focus} \equiv \underbrace{\frac{U_{top} + U_{bottom}}{2}}_{\text{vertical focus}} = \underbrace{\frac{U_{left} + U_{right}}{2}}_{\text{horizontal focus}} \qquad (3.18)$$

where U is the potential of the respective electrodes and overall focus voltage.

Another advantage of the system is that it allows for astigmatism in the beam to be corrected, in this case by breaking the relation shown in equation 3.18 and altering the relative focal strength of the left/right and top/bottom electrodes. This effectively stretches or squeezes the lens in that axis, which can be used to bring the two focal points into coincidence.

Deceleration Lens

Figure 3.11 shows the deceleration lens in greater detail. The cutaway section shows the grounded trumpet that the ions travel through, before they experience the retarding potential in the final few centimetres of the lens. A large earthed section (indicated in green) is attached to the back of the deceleration lens (indicated in orange) to initially

(a) CAD drawing **(b)** Real lens
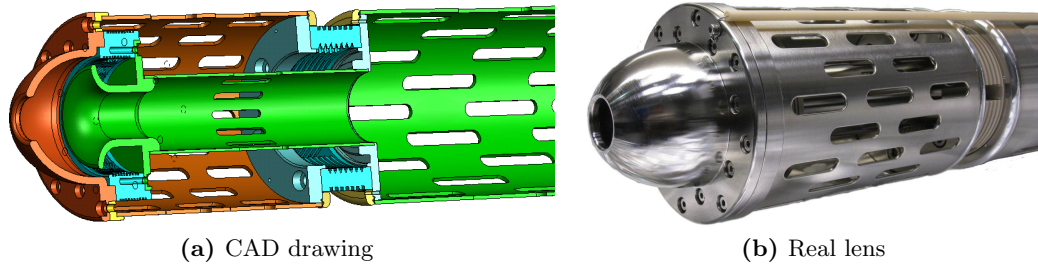
Figure 3.11: Cutaway of the CAD drawing for the deceleration lens, showing the inner components and a photograph of the real lens, before being mounted into the beamline. The photo shows the ceramic rod housing the high voltage connection for the lens tip.

shield the ions from the chamber field before they reach the tip, when the lens is extended fully into the target region. This ensures that the only field experienced by the ions is that of the deceleration lens, which is an experimentally controllable parameter.
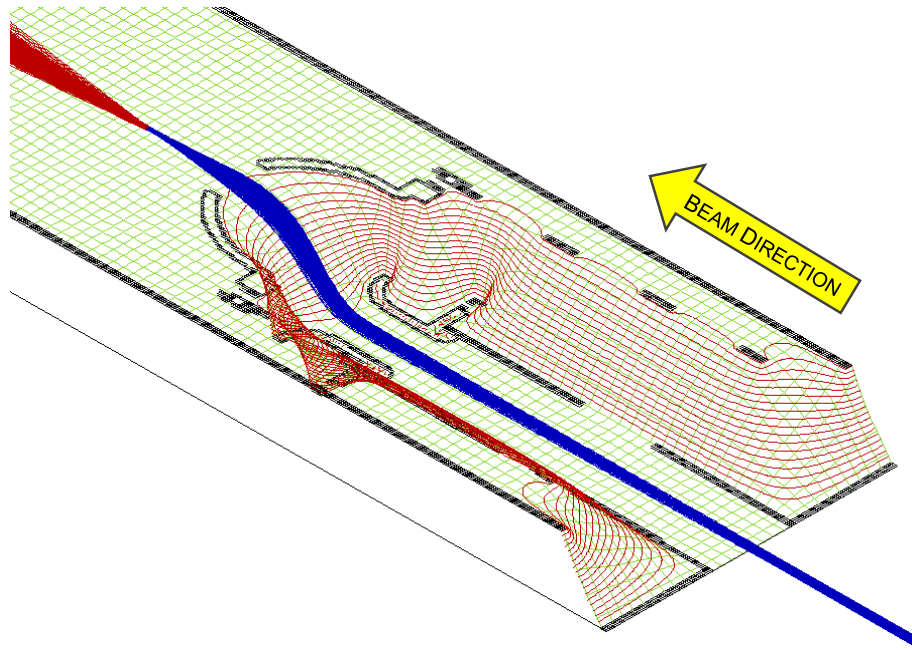
Figure 3.12: Simulation of the electrostatic field generated by the deceleration lens and the surrounding target chamber, plus its effect on an incoming ion beam.

The shape of the lens is designed to provide a smooth electrical field gradient and is also responsible for focusing the beam. Figure 3.12 shows a simulation of the potential field experienced by an ion entering the lens. The red contours are lines of equipotential, and the incoming beam is seen in blue. The saddle-like nature of the potential is shown, responsible for the focusing effect.

The lens is held together with PolyarylEtherEtherKetone (PEEK) isolating rings, ribbed to increase surface resistance and reducing the risk of discharge. During high-voltage conditioning of the beamline, these were shown to be effective at isolating the lens

up to at least $+25$ kV (the maximum test voltage) at pressures of $\leq 10^{-7}$ Torr.

Gas Injection System

Figure 3.13: Photograph taken looking into the target chamber. The tip of the gas injection capillary is shown in the centre of the image, entering from above. The capillary is mounted below a steel plate with varying known hole sizes, used for beam diagnostics. To the left is the germanium X-ray detector and behind is the tip of the deceleration lens.

The gas injection system currently in use consists of a 0.1 mm (inner diameter) capillary tube, mounted on a linear manipulator extended into the chamber, see figure 3.13. The opening of the capillary is orientated vertically down into the turbomolecular vacuum pump mounted below the target chamber, whilst the other is connected to a flexible Teflon pipe. This pipe is connected to a larger capillary which is welded to a vacuum gas dosing valve. This system allows the capillary to be moved within the chamber without placing strain on any of the components.

Connected to the non-vacuum side of the gas dosing valve is a metal T-piece, enclosing a small volume that can be filled with the target gas. One outlet connects to the valve, one to the gas flask, and one to the chamber pre-vacuum pumping system, thus allowing gas to be expelled from the system without having to flow through target chamber. This is a benefit when changing target gases, as it also means that the capillary can more effectively be pumped free of residue gas.

One of the problems with this system, is that it is very difficult to determine exactly how much gas is being injected into the system. The density of the gas target at the tip and the evolution of the gas cloud can only be estimated by calculations and comparison

with literature, and is not directly accessible to measurement. Whilst the gas dosing valve itself features an arbitrary scale, a more reliable method of injecting the same quantity of gas into the system was by increasing the gas flow until the chamber pressure had risen a given amount from its constant baseline pressure (typically in the region of 10^{-9} Torr).

3.4 Beamline Detectors and Equipment

3.4.1 Position Sensitive Detector (PSD)
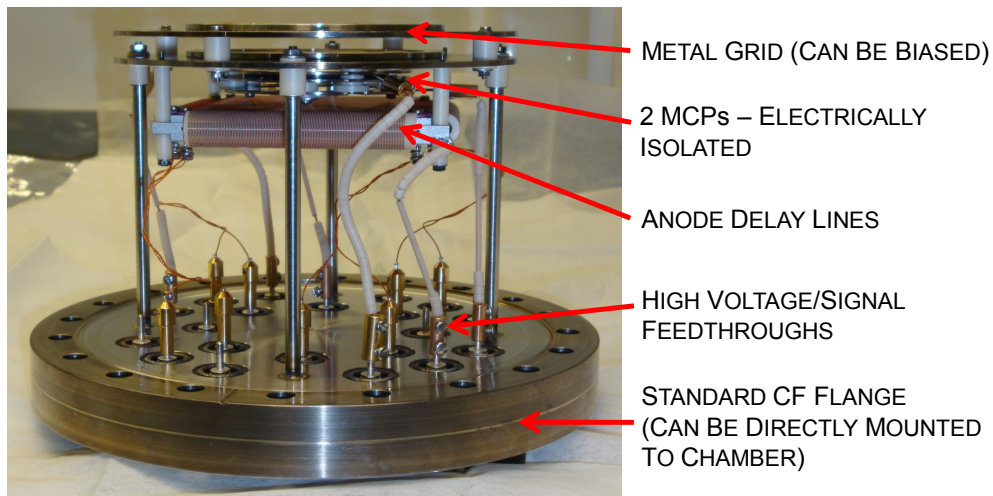
Figure 3.14: Photo of the Position Sensitive Detector used in the experiment. Two sets of delay lines (only one seen here) allow the 2D position of an incoming charged particle to be determined. The effective detector diameter is 40 mm.

Two Micro Channel Plate (MCP) detectors with two anode delay lines, referred to as a PSD, were used to detect ions. The detectors used at the Heidelberg EBIT[7] use two stacked MCPs fitted in front of two perpendicularly orientated anode delay lines (see figure 3.14).

The MCPs are finely perforated glass plates (typically 160,000 holes per cm^2) which form tubes through the material [Mos09]. The glass plate is coated with a conductive material. In principal they function similarly to many miniature photomultiplier tubes stacked together. A particle striking the inside wall of one of the tubes causes secondary emission of electrons. These are accelerated by the potential gradient into another part of the tube, and so forth (see figure 3.15). The tubes do not pass perpendicularly through the plate, but an angle of approximately 8° [Roe09]. By stacking two plates in a chevron configuration, it is possible to ensure that an incident particle cannot pass through the detector without striking a surface.

A charged particle, incident upon the first MCP causes a cascade of electrons to be produced. The electrons are accelerated towards the second MCP by a potential gain

---

[7]In the extraction system is a 40mm diameter RoentDek Position Sensitive Detector, the deceleration beamline detector was constructed in house.

applied to the detector. Upon striking the second MCP another cascade is formed, in effect amplifying the original signal generated by the projectile. Both MCPs combined give an gain factor of $\approx 10^6$ [Roe09]. This then passes through two sets of delay lines. Each comprises of two thin wires wrapped side by side around a retaining framework. One is a signal wire, whilst the other acts as a reference wire, which is used to subtract background noise detected equally by both reference and signal wires. The signal wire is biased by $\approx$ 20 - 100 V [Arn08] which causes the electron cascade to be captured by the signal, as opposed to reference wire. A current is generated in the signal line that then flows to both ends of the wire. This generates two signal pulses at either end of the wire, which arrive at different times, depending upon where the particle struck (see figure 3.15a). This time interval is measured using a Time-to-Digital Converter, and the collected data can be used to generate an image of particles striking the detector. The second anode delay line performs the same task, but is orientated perpendicularly to the first in order to obtain the position in the second dimension.

(a) Signal wire shown in purple, reference wire in lighter colour.

(b) Chevron arrangement of the MCPs
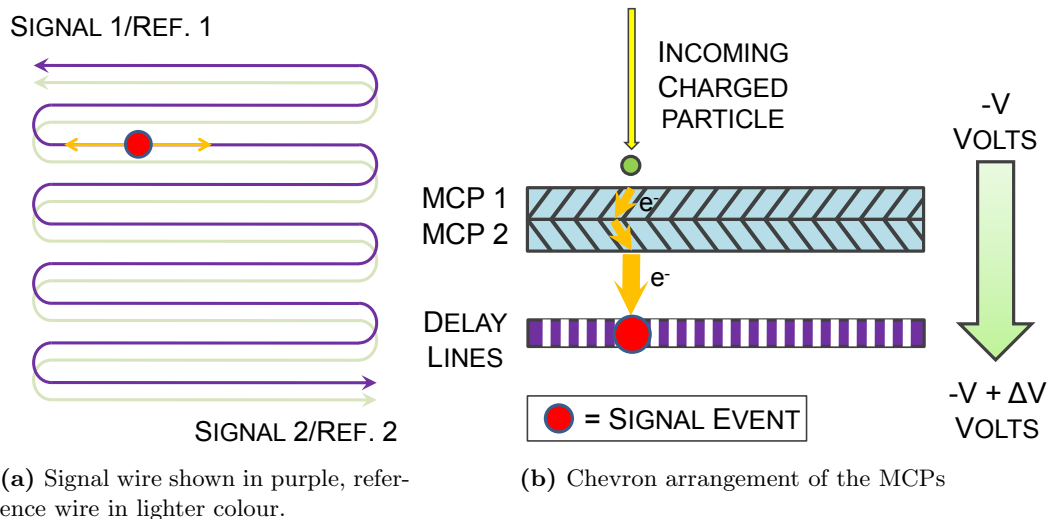
Figure 3.15: The left graphic is seen looking along the beam axis towards the detector, and the right is a schematic cross-section through the detector plane.

3.4.2   Germanium X-ray Detector (IGLET)

The other major detector used during this project was a High Purity Germanium (HPGe) X-ray detector[8]. This detects incident photons in the energy range from $\approx$ 1 - 30 keV, with an active detector diameter of 11 mm. With the detector $\approx$ 20 mm away from the target region, this gives a solid angle acceptance of approximately 100 milli-steradians, or 0.8% of the total solid angle encompassed by the target region. This is estimated by treating the detector area approximately as the fraction of the surface of a sphere, as given

---

[8]An ORTEC GLP Series High-Purity Germanium Detector (IGLET).

by

$$\Omega \approx 4\pi \frac{A_{detector}}{4\pi r^2} \tag{3.19}$$

where $A_{detector}$ is the area of the detector and r is equal to the distance between detector and target region.

Photons enter the detector through a thin ($\approx 25\ \mu m$ [Epp07]) beryllium window and strike a germanium semiconductor. An incoming photon excites electrons from the semiconductor's valence bands, into the conduction band. A bias of $\approx$-1 kV applied to the crystal causes these electrons to flow out of the crystal and the resultant current pulse is measured. As the energy needed to create an electron-hole pair in the crystal is constant, and the total energy of a photon is used to produce electron-hole pairs, the magnitude of this pulse is directly proportional to the energy of the incident photon. A photon of higher energy will excite more electrons and therefore a larger pulse.

The signal from the detector is initially pre-amplified with a fixed gain and the amplified again by a spectroscopic amplifier. The latter allows the amplitude and shape of the signal pulse to be changed. Altering the gain of the signal determines partly the resolution of the measured signal, as the signal is digitised by a system that samples pulse heights between 0 - 10 V. Increasing the gain causes the loss of information about higher energy photons, however it also spreads the lower energy range over a greater number of sampling channels, improving the energy resolution. During commissioning of the beamline, tests using a ^{57}Co calibration source and spectroscopic amplifier were used to optimise the photon energy resolution seen by the data acquisition system in the range 2 - 5 keV. This corresponds to the region of interest for argon X-ray emissions. For the shaping time (6 μs) used, the specified energy resolution of the detector for the Ar K-α peak is ≈ 130 eV [ORT07].

The detector used in this project was limited by its efficiency to resolve lower energies. Figure 3.16 gives the relative efficiency of the detector used as a function of photon energy. Below 3 keV, the detector efficiency quickly drops, with an efficiency of less than 5% for photons below 1 keV. For charge exchange reactions, emitted photons lie around and below the 3 keV region, making it harder to detect photons of interest. For experiments conducted with argon, this is not a major limiting factor, as the Ly-α peak for Ar^{18+} and Ar^{17+} are ≈ 3 keV, however in future work with other elements, this will become so. The limit is caused not by the semi-conductor crystal, itself capable of detecting photons below 500 eV [ORT07], but by the beryllium detector window. The window allows 80 - 90% transmission, but only for photon energies above 2 keV. The solution is to operate a window-less detector, however this places stringent requirements on the cleanliness of the vacuum within the chamber, to avoid contaminating the crystal.

3.5   Charge Exchange Experiments

3.5.1   Overview of Method

For the charge exchange experiments discussed in this work the EBIT was prepared and optimised for the production of bare and hydrgogen-like argon ions. The main EBIT parameters, the electron beam current and its energy were tuned to produce high charge states of argon efficiently. In this case the electron beam current was set to 300 mA (a
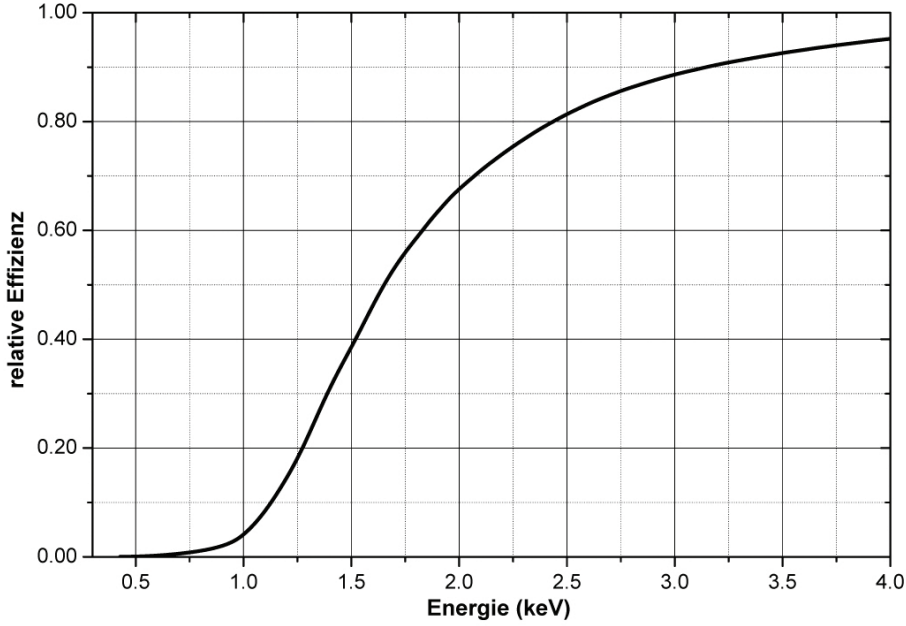
Figure 3.16: IGLET X-ray detector efficiency as a function of photon energy, due to beryllium detector window. Figure from Epp [Epp07].

relatively high value for the Heidelberg EBIT), which results in high electron impact rates and therefore the fast production of high charge states.

The energy of the incident electrons must exceed the ionisation potential of the charge state required. For Ar^{18+}, $E_{bind} = 4426$ eV is required to ionise the last K-shell electron. The beam energy is 11.5 keV, as shown in section 3.1.1, comfortably above the required value. Argon gas can be injected directly into the trapping region and within less than 30 seconds Ar^{18+} can be identified using a germanium X-ray detector mounted directly on top of the trapping region. Figure 3.17 shows two spectra taken before and after gas injection was turned on. The highlighted peak at ≈ 15.5 keV is caused by the radiative recombination of electrons captured from the electron beam into the argon K-shell. The energy of this transition is a sum of the kinetic energy of the incoming electron and the binding energy of this electron, as given by

$$E_\gamma = E_k + E_{bind} \tag{3.20}$$

where the electron kinetic energy is given as

$$E_k = U_{DT} + U_{cathode} + U_{gun} - U_{space} \tag{3.21}$$

The X-ray energy in this case derives to

$$E_\gamma \approx 10 + 1.5 + 0 - 0.35 + 4.4 = 15.5 \text{ keV} \tag{3.22}$$

where U_{dt} is the potential of the drift tubes, $U_{cathode}$ is the potential applied to the electron gun cathode, U_{gun} is the potential the gun sits on (in this case 0 V), and U_{space} is the
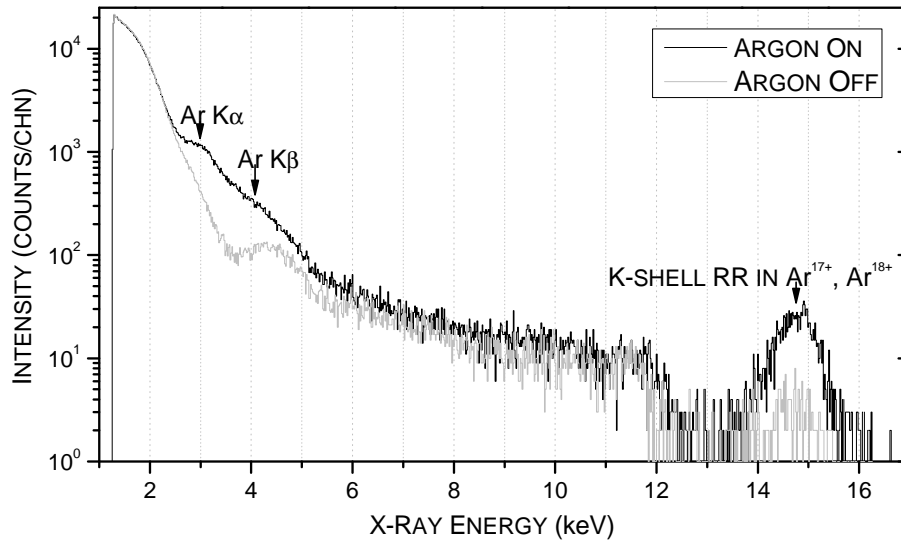
Figure 3.17: Two X-ray spectra taken in the EBIT before and after argon injection. The acquisition time was 400 seconds in both cases. The detector had been pre-calibrated using a radioactive reference source. The peak due radiative recombination of electrons into bare and hydrogen-like argon is marked, along with the positions of argon K-α and K-β transitions. Electronic noise caused a severe degradation of the X-ray detector resolution in this dataset.

reduction in the kinetic energy due to the electron beam, including compensation for the ion cloud space charge (see section 3.1.1 for further details).

The smaller peak seen in the spectra taken without argon is caused by residual argon leftover in the trap. Argon had been injected about 30 minutes before this spectra was taken. The structure in the 2.5 - 5 keV range, is due mainly to K-α and higher order transitions into the K-shell of argon. The spectra in this range, including the large continuum seen between $\approx$ 1.2 keV and 2.5 keV is difficult to determine due the high level of background X-rays from bremsstrahlung produced by the electron beam. The spectra is cut off below $\approx$ 1.2 keV, which corresponds to the set value of the lower level discriminator of the data acquisition system. This system is set to reduce device dead-time by suppressing low energy background counts.

After argon was identified in the trapping region the EBIT was then set to dump every 30 seconds and the 90° analysing magnet was scanned to produce a spectra of the different q/m states present in the trap.

The Ar^{18+}, and later Ar^{17+} were identified, selected, and sent through to the deceleration beamline, as described in 3.2. The beam was then optimised onto the deceleration beamline PSD, initially without any retarding potential, using the two Sikler lenses. The results of the simulation were used as a starting point for setting the potentials. The apertures mounted midway along the beamline were used as a diagnostic tool to identify the behaviour of the beam at this point. For example it cannot be assumed that the detector picture one sees on the computer screen is correctly orientated. In reality the detector had to be mounted rotated by 4.5° to the delay line axes due to the rotation of the chamber mounting flanges.

Once a circular beam could be detected in the central region of the PSD then the high-voltage platform was isolated from ground and the system and a retarding potential was applied incrementally to the chamber and deceleration lens. For these experiments the deceleration lens was connected to the same potential as the target chamber, however it can be independently varied, relative to the floating platform. A series of qualitative tests showed that in the range of $\pm$ 200 V this made no noticeable difference to the beam.

It is important to note however that a small beam spot seen on the deceleration beamline PSD (at around 7.2 kV) does not correspond to a small spot in the target region in the centre of the chamber. The detection plane lies $\approx$ 120 mm from the centre of the chamber and therefore the focal distance of the lens must be reduced by this amount to achieve a dense, small beam in the target region.

With a small beam spot, neutral argon gas is then injected into the target chamber. In order to increase the likelihood of striking the gas jet with the ion beam, the capillary injection tube is initially moved (by means of a three-dimensional, electrically isolated translation stage) so that the beam strikes its steel tip. An ion beam incident upon a metal results in the generation of many soft X-rays due to the neutralisation of HCIs at the surface. For a 20 kHz ion beam in the target chamber, an X-ray count rate of up to 100 Hz can be achieved by steering and focusing the beam. This count rate refers to X-rays produced from HCI - surface interactions. The count rate for X-rays of interest during the charge exchange experiments was much lower, as discussed later. The count rate for surface interactions agrees with solid angle seen by the detector of approximately 0.8% (as discussed in section 3.4.2), assuming that photons are emitted isotropically. Further reductions must be made to take into account the cross section for electron capture in the case of the charge exchange experiments.

Once the beam is known to be striking the tip of the capillary tube, the capillary is slowly withdrawn out of the beam from until the X-ray count rate suddenly drops as the beam no longer strikes the tube. It can then be assumed that the beam is striking the densest part of the gas jet (just after it leaves the capillary tube), thus giving the highest probability for interactions.

Data acquisition can then begin and the formation of peaks, can typically be observed within 2 hours. For the data presented here the experiments ran for approximately 48 hours, giving a useful X-ray count rate of approximately 0.02 Hz. The reasons for this low rate and suggestions for improving it are discussed later in section 6.

Figure 3.18 shows the arrangement of detectors. The window of the X-ray detector was approximately 20 mm from the target region and the PSD approximately 120 mm away. In this experiment the tip of the deceleration lens was brought forward so that it was approximately 30 mm from the centre of the chamber.

3.5.2 Coincidence Spectroscopy

Using the setup described above, it is possible to take spectra of X-rays being emitted in the target region, however there is still no guarantee that these photons originate from the desired interaction. Stray ions from the beam can still strike the metal capillary tip, the deceleration lens or detector mountings. These counts would distort the spectra as the interaction process of an HCI with a metal is different to the interaction with a neutral gas atom. In order to isolate the photons resulting exclusively from charge exchange, coin-

cidence spectroscopy is used. As shown in figure 3.18 there is a distance of approximately 120 mm between the target region and the PSD. The velocity of a decelerated HCI, which interacts with a neutral, is approximately unchanged by the interaction as the kinetic energy transferred is typically less than 1 eV [Mos09], compared to the $\approx$ 700 eV/q of the ion beam. It has a finite flight time between the target region and the PSD, which remains constant (within a given uncertainty). Any photons which are the result of charge exchange will have a corresponding projectile ion which strikes the PSD at a constant delay with respect to the photon detection, whilst photons from other sources will not have a corresponding ion. By correlating the counts from both the X-ray detector and the PSD, it is possible to identify those photons of interest, as they will always be followed by an ion count, a fixed period after the photon arrived. The ion count signal was intentionally delayed to ensure that it always arrived after the photon start signal.

The scheme for making a measurement is as follows:

1. A charge exchange event occurs.

2. The corresponding photon produced by the excited state decaying to the ground state of the HCI is detected.

3. The energy of this photon is recorded and a timer is triggered in the Time-to-Digital Converter.

4. This timer runs until a particle is detected upon the PSD, which triggers a stop signal.

5. The time difference and photon energy are recorded in coincidence.

Other parameters such as the energies from all photons and the position of the incident ion are also simultaneously recorded.
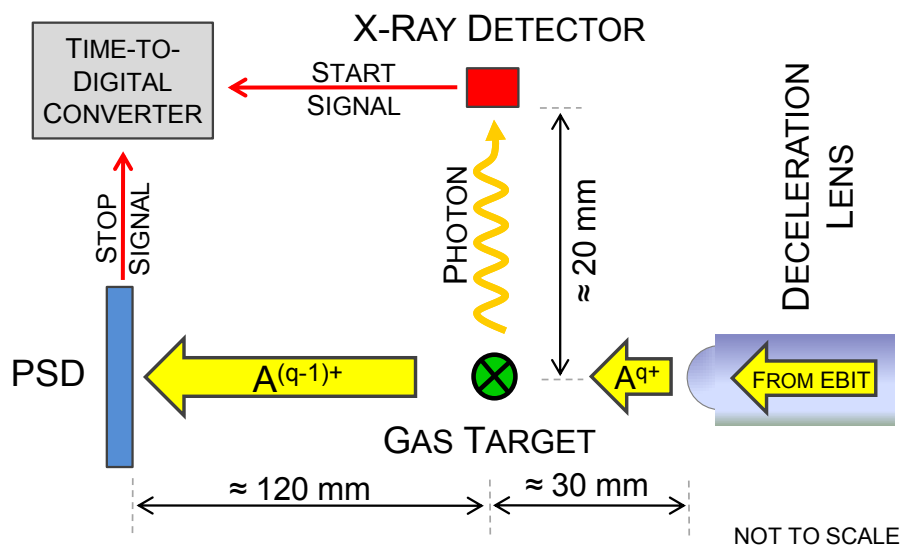
(a) As seen from above

(b) As seen looking into X-ray detector, PSD not shown

Figure 3.18: Above: Schematic of the detector layout in the experimental chamber. **Below:** Photo taken from the side of the chamber showing the tip of the deceleration lens, the X-ray detector and the gas capillary tube.

Chapter 4

Simulation

4.1 Introduction

One of the difficulties involved with diagnosing the behaviour of an ion guiding system, is understanding how ions move through the apparatus. Before and during its construction, the deceleration beamline was modelled in the ion simulation package SIMION 8.0 [DJM07], to help diagnose the behaviour of ions passing through the system. The main aims of the simulation were:

- to quantitatively estimate the ion optical properties of the beamline: including the kinetic energy, energy spread, angular divergence, and spatial distribution of the decelerated ions, as well as the beam profile size,

- to estimate for a given lens position, the voltage required to focus the beam into a specified target region,

- to visualise how ions move through the beamline, and the electric field they experience - particularly in the region of the deceleration lens.

4.2 Assumptions

The deceleration beamline simulation uses a number of assumptions to reduce the complexity of the model. Simplifying the model places emphasis on the components of the beamline that have the most significant influence on the ion beam and reduces the required processing time.

4.2.1 No Self-Induced Beam Repulsion

It can be estimated that there is only one ion travelling between the EBIT and the end of the beamline at any one time. For example Ar^{18+} leaves the EBIT with a kinetic energy of approximately 10 keV/q (disregarding the space charge reduction). Each ion has an energy in Joules given by

$$E_k \approx 3 \times 10^{-14} \text{ J}$$

where 1 eV $= 1.6 \times 10^{-19}$ J. The velocity of an ion travelling through the system is then

$$\nu = \sqrt{\frac{2E_k \text{ [J]}}{M \text{ [kg]}}} \approx \sqrt{10^{12}} = 10^6 \text{ ms}^{-1}$$

where ν is the velocity of the ion and M is the mass of an argon ion in kg. The distance d between the EBIT and the end of the deceleration beamline is approximately 10 m, thus giving a ion travel time of

$$t = \frac{d}{\nu} = \frac{10}{10^6} = 10^{-5} \text{ s.}$$

This can now be compared to the ion count rate measured at the end of the beamline, which for Ar^{18+} was typically f=20 kHz. This gives a time period between counts of

$$T = \frac{1}{f} = \frac{1}{20 \times 10^3} = 5 \times 10^{-5} \text{ s.}$$

Therefore the average number of ions in the beamline any one time is less than one, assuming equally distributed ion emission from the EBIT over time. This result is supported experimentally by observing the arrival of ions on the PSD. Simultaneous counts are rarely seen, and so it can be taken that the assumption of single arrival is true, and not that the ions arrive in bunches for example.

4.2.2   Ion Beam Only Affected by Electric Fields

In the following it is assumed that only electrostatic forces act upon ions within the experiment, and that these forces arise purely from the electrostatic fields of the ion lenses, the deceleration lens and the experimental chamber. Other effects are negligible, for example the gravitational force acting on an ion with a mass of $m \approx 10^{-25}$ kg is on the order of $F_{grav} \approx 10^{-18}$ N, and for the earth's magnetic field $F_{mag} \approx 10^{-16}$ N.

Possible sources of electromagnetic interference are also considered unimportant in this treatment. The turbo-molecular pumps used to pump the beamline produce a stray magnetic field [Vac08], however are located further than ≈ 200 mm from the central beamline axis, and therefore have no noticeable effect on the ion beam.

Likewise the electric fields produced by the high operating voltages of the pressure measuring ion gauges in the beamline are also not considered, as these are again sited far from the beam and are partially shielded, by steel mounting tubes.

4.2.3   Gaussian Distributed Particle Source

The starting distribution of particles entering the simulation was modelled by a 3D Gaussian position distribution located 400 mm along the beam axis, before the first ion optic. The choice of this starting coordinate corresponds to the position of a vacuum gate valve, which isolates the experiment from the switch magnet, and is considered the limit of the beamline. It assumes ions leaving the switch magnet do so with a similar distribution. As there is no method available to measure this in reality, this assumption is a source of uncertainty in this simulation.

The initial velocity of each is parallel to the beamline axis, before the elevation (θ) and azimuthal (Φ) of the ion was randomised between $+89° \leq \theta \leq +91°$, and $-1° \leq \Phi \leq +1°$

respectively. This 2° beam divergence was based upon knowledge obtained from the other experimental beamlines at the EBIT. It is an over-estimation of the actual beam, which is shown to be approximately parallel in section 5.

4.3 Limitations

The simulation program is ignorant of the processes that occur when ions come into contact with surfaces. It simply considers that an ion has 'died' and removes it from further calculations. The interactions of ions with residual gas in the the system is also not considered. In reality many different processes can take place, such as neutralisation, charge exchange, or the production of secondary particles (electrons, ions) and X-rays. In this way, lower charge state ions can be formed before reaching the deceleration lens, as explained in more detail in section 5.

Finally, the quantitative data obtained from a simulation should always be treated with caution. The validity of the values generated in this simulation and comparison to experimental results is discussed later.

4.4 Method

4.4.1 SIMION

SIMION 8 was used for the simulation[1], a program which models particle trajectories through electromagnetic fields.

Whilst the native program interface is fine for small numbers of individual simulations, it becomes problematic when the user wishes to test multiple electrode values, or ion parameters. This would require altering the electrode potentials individually and then re-running the simulation, a process which is highly time consuming. It also results in the generation of many small data files, one for each simulation, which are difficult to assimilate and analyse. The answer in this case is to extend SIMION using a scripting language, allowing multiple simulations for multiple parameters to be more efficiently and unattended.

SIMION has built in support for Lua, a lightweight scripting language [RI06]. The software interacts with Lua using a system of program segments. These are special functions, that are called by SIMION during different stages of the simulation. User programs can influence SIMION and access data through a small number of reserved variables (which describe parameters such as an ions properties or the voltage applied to an electrode) of which only a few can be accessed in each program segment. Within these program segments Lua script can be used to process and record data, as well as alter and re-run the simulation. User programs can also define new variables, allowing the user to specify new simulation parameters. This was used to provide an interface for defining quantities such as upper and lower electrode voltages. Further discussion of the interaction of SIMION and Lua will be avoided here, as this is already well-documented elsewhere [DJM07].

---

[1]See `http:\simion.com` for further information.
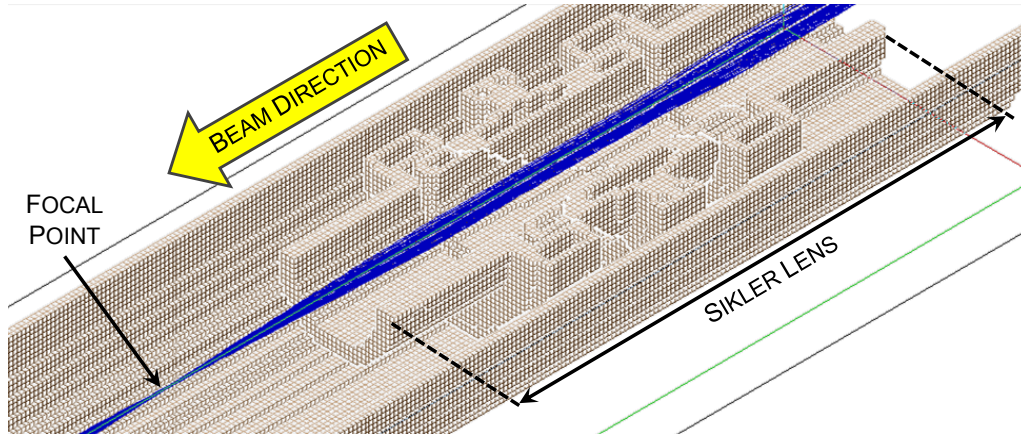
Figure 4.1: The software allows the trajectory of ions that pass through the beamline to be visualised. In this case the focusing effect of the first Sikler lens is shown.

4.4.2   Run Process

The process of preparing and running the simulation consists of the following stages:

1. **Simplification:** Complicated CAD elements of the design are replaced with simple geometric shapes which in the simulation create a similar electric field. Trial simulations showed that the effect of the simplifications made here on the ion trajectories was negligible. The potential field seen by ions in the centre of the target region was unchanged.

2. **Conversion:** the simplified CAD data of the beamline and the electrodes of the ion optics are converted into SIMION's native format. The quality and resolution of the conversion performed directly affect the accuracy of the simulated trajectories [DJM07] and the processing time required. Lower qualities introduce asymmetries into the electrode geometry, which are later manifested as subtle deflections of the trajectories.

3. **Refining:** SIMION solves Laplace's equation numerically for the given electrode geometry.

4. **Assembly:** These electrodes are assembled in a 3D workbench where the resulting solutions of the potentials are superimposed by SIMION. This provides an environment in which the ion trajectories and potential fields can be viewed, as shown in figure 4.1 .

5. **Define simulation parameters.**

6. **Run simulation:** this could take anything from a few seconds for a simple 100 ion run, or up to 5 days for multiple batch simulations.

7. **Analysis:** Data is automatically written, labelled, and exported by the Lua code when the simulation is run. These data files can then be directly imported into the

analysis software. A log file is also written by the Lua code, detailing all the initial parameters, when parameters where changed during the runs, any warnings about ion flight paths, or error messages if the simulation or controlling algorithm failed.

4.5 Simple Optimisation Algorithm

A simple optimisation algorithm was used to investigate the relationship between the focal distance of the deceleration lens and different deceleration voltages. The algorithm is designed to quickly minimise the average beam spot size in a given detection plane, by changing the deceleration voltage. The beam spot area is estimated by finding the standard deviation in the x and y position of 100 simulated ions and then by using the formula for the area of an ellipse,

$$\text{Area } = \pi ab \ , \tag{4.1}$$

where a and b are the semi-major and semi-minor axes respectively. The values used for a and b were the standard deviation of the x and y distribution of the ions, giving an overall major and minor axes that were inclusive of two standard deviations of the data (95% of all ions hits). This method was developed after testing the algorithm, in order to reduce the impact of outliers artificially inflating the spot size.

During the first run of the algorithm, detailed in figure 4.2, a crude scan is made across a user-specified voltage range for the deceleration lens. The algorithm then assigns the centre of the next scan to the voltage determined to have produced a minimum in the previous run. The scanned voltage range is reduced to this new central voltage plus or minus the previous step size, ΔU. The new step size is then defined as half or a third of the previous. The division factor depends upon whether the iteration number is even or odd. This is particularly important to avoid sampling the same parameter selection twice, which might cause the algorithm to decide it had found a minimum, because the relative difference in size between two consecutive spots would be approximately zero. The program then rescans across this new region and repeats the entire process until the relative difference between subsequent spot size minimum falls below a specified threshold (for example 0.1%). The program then declares this to be the spot size minimum and outputs the corresponding deceleration voltage.

Advantages

The code is quick to run, taking typically < 60 seconds to find a focal spot. In comparison, testing all possible permutations systematically to the same degree of accuracy would take 1 - 2 hours. The total number of simulations is low, and so this method generates very small (< 100 kb) data files, which are quick to process.

Disadvantages

It must be stressed that this is a very simple and naive algorithm. There exist far better algorithms, designed for finding the minima of a functions, however due to time constraints and the relative importance of other areas of the project, there was not the opportunity for further development.
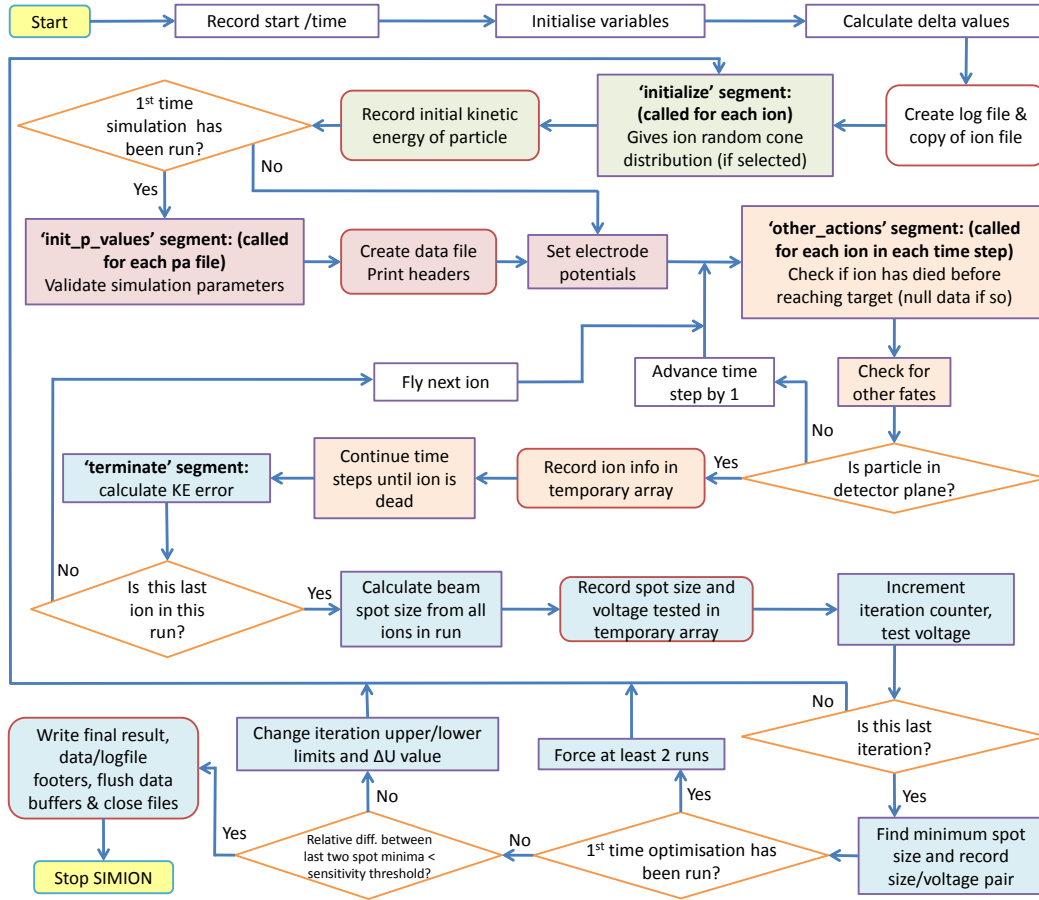
Figure 4.2: Flow diagram of the optimisation algorithm. The coloured shading shows processes which belong to the same SIMION program segment, rounded boxes indicate data operations. Further information about the program segments can be found in the SIMION 8 user manual [DJM07].

The algorithm is simple, and will only work effectively for simple functions with just one minimum. It is dangerous to use this algorithm on more complicated functions with multiple minima, which occur in a range less than the initial ΔU value, as these could be missed by the algorithm. Fortunately in the context of the focal distance simulation, this is not a problem, as the original beam can be perfectly defined - there is no need to introduce statistical uncertainty (such as an initial kinetic energy distribution), as we are only interested in the deceleration voltage that works best for the majority of the incoming ions (i.e. an average ion). The simulation is a closed, controllable environment. We know for example that a simple converging lens (such as the deceleration lens) may only produce one focal point, hence the test function for the algorithm only has one minimum[2].

Care must be taken to ensure that the initial voltage test range is large enough, however

---

[2]The optimisation algorithm does not consider what has happened to the beam before it reaches the deceleration lens.

given the speed of the algorithm, it is reasonable to specify the full current working range of the lens, 0 - 10 kV, as a starting point.

4.6   Programming

General good coding practices, as described in [JN03], were followed to keep the code as efficient as possible. A separate Lua function library was written, containing general purpose mathematical functions which can be used in future projects (a code listing is given in appendix B.2). These included functions for finding the mean, standard deviation, and lowest value of a dataset, as well as extracting values for the speed and kinetic energy from the ion velocity vectors. Custom functions for outputting data to the screen, log and data files were also created.

An error handling system was written, in order to validate variables input by the user, as well as for monitoring the simulation for potential problems. If, for example, too many or indeed all of the ions are scattered before they reach the target detection plane, the program will halt the simulation, as opposed to looping infinitely. All steps the program makes are also logged, to allow for quick debugging, as well as providing a record of the user-defined parameters.

An extension of the error system is the ability to specify target thresholds for the number of ions that reach the detection plane. In the case of most simulations, in which a statistically variant source of ions is used, there will always be some ions that collide with electrodes, and never reach the detection plane. In this case the user can specify the percentage of ions required to reach the detection plane for the simulation to be considered valid. It could be decided for example that a permutation that results in less than 50% of the original beam reaching the target region is useless. In this case the program will nullify all data (except the combination of electrode potentials for which this occured) for this run. This reduces the risk of meaningless numbers appearing in the datafile, which could inadvertently be included in the data analysis.

Fully-commented code listings for the simulation algorithm and batch operation scripts are included in appendix B for reference.

4.7   Simulation Results

Figure 4.3 shows the results from the simulations of 400,000 ions (corresponding approximately to a 24 hour observation period - typical ion count rates in the beamline are 20 kHz). The parameters for this simulation are shown in table 4.1. For a deceleration voltage of 8990 V the kinetic energy spread of the decelerated ions is reduced from 10 eV/q to 8.8 eV/q. This is unusual, and could possibly be the result of rounding errors within the simulation which result in the loss of kinetic energy. Rounding errors on this scale however do not affect the main conclusion from this result, that the deceleration lens does not significantly broaden the spread of the kinetic energy distribution of the incoming ion beam.

The mean azimuthal and elevation distributions show slight deviations (2.1° and 0.2° respectively) from the expected mean of 0° for a cylindrically symmetric system. These

(a) Kinetic energy spread

(b) Velocity magnitude spread

(c) Elevation spread

(d) Azimuthal spread
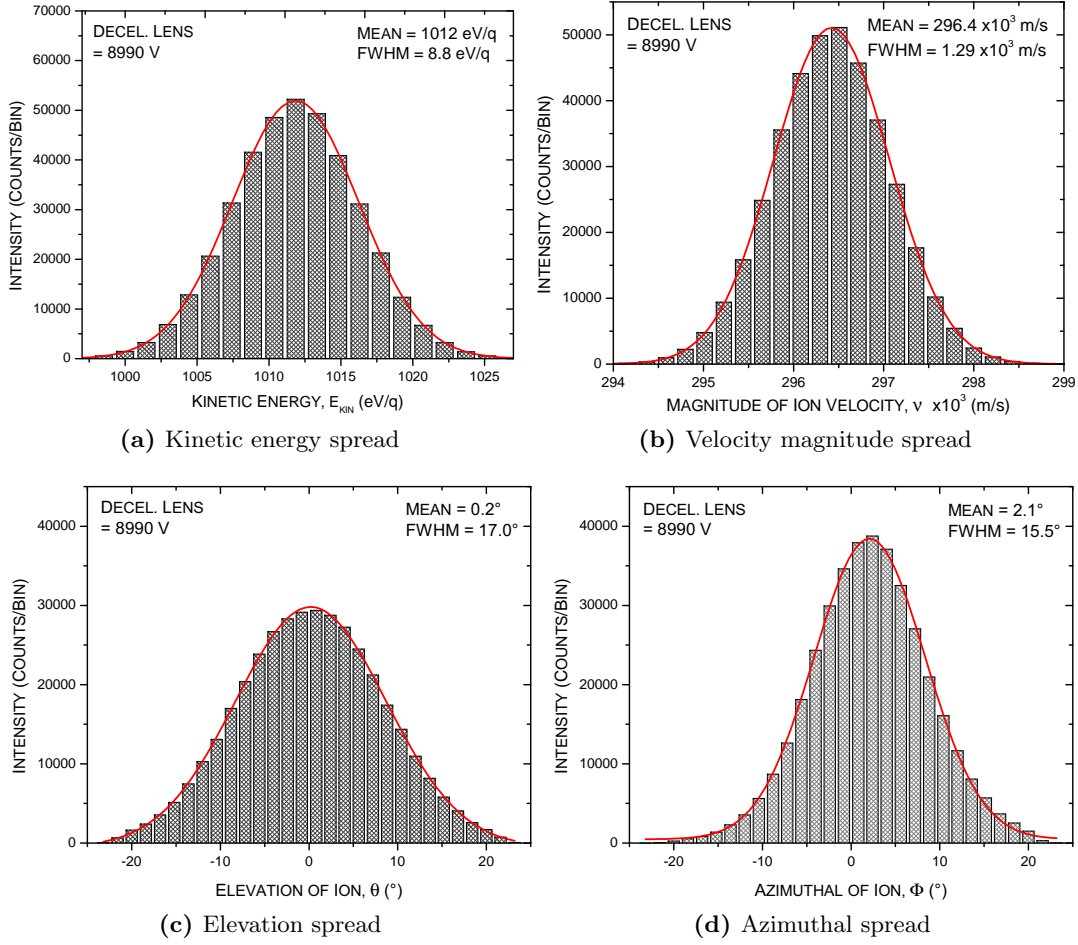
Figure 4.3: Four typical simulated distributions of the ion beam in the target region, using a deceleration voltage of 8990 V. For reference, the numerical results of the fits performed here are shown in table A.3 in appendix A.4.

deviations are the result of asymmetries in the electrode geometry introduced by the conversion process, as mentioned previously.

The culminated results from simulations at different deceleration voltages are shown in figure 4.4. Figures 4.4a and 4.4b show the relationship between deceleration voltage and mean kinetic energy and mean velocity magnitude as a function of deceleration voltage. Linear and power fits of the data show reasonable agreement between the simulated data and the expected physical relationship between these quantities, although there is some deviation in the case of the velocity magnitude from the expected relationship of $\nu \propto U_{decel}^{1/2}$. Tests showed that at 9990 V, significant scattering of the beam occurs as the kinetic energy of the decelerated ions (10 eV/q) tends to zero. This scattering is likely to affect the distribution of ions that reach the detection plane.

Figure 4.4c shows the Full Width Half Maximum spread of the angular distribution of the ion beam and its kinetic energy as a function of deceleration voltage. Between

Initial Beam Parameters	
Number of Ions	400,000
Ion Mass Number	40
Ion Charge State	18+
Initial Beam Divergence	2°
Kinetic Energy Distribution	Gaussian
- Mean	10 keV/q
- FWHM	10 eV/q

Table 4.1: Parameters used for the simulation of beam characteristics for different deceleration voltages.

8990 and 9750 V the kinetic energy distribution remains approximately constant, however the distribution quickly widens as the kinetic energy of the ion decreases, as a result of the scattering process described before[3]. Both the azimuthal and elevation distributions increase with deceleration voltage, and the fitting of the data points show both are in good agreement with reciprocal functions, although the reasons for this are still not well understood.

Figure 4.5 shows an example of the optimisation algorithm with each iteration indicated by a data point. At these voltages the algorithm has run a simulation of 100 ions, before calculating the corresponding spot size. The higher density of data points around ≈ 9000 V show where the algorithm has increased the number of iterations made to locate the minimum. In this simulation the detection plane was 30 mm from the tip of the deceleration lens, the same distance as used in the experiment. This optimisation was confirmed by running a separate simulation with the voltage suggested by the algorithm. The spot minimum was observed to be < 1 mm away from the detection plane.

Using the optimisation algorithm the relationship between the deceleration voltage and focal distance was investigated, as shown in figure 4.6. The algorithm operates by testing different voltages for a given focal distance. The uncertainty in the deceleration voltage is given as ± 50 V, after tests showed the error in correctly locating the spot size minimum was approximately this value. The data appears to follow a parabolic relationship, and there is still uncertainty as to whether this accurately reflects the true nature of the lens, as further testing with the real lens remains to be completed. However the result appears to agree qualitatively with the work of Cerezo and Miller [CM91], who have simulated and measured the behaviour of an Einzel lenses (of which the deceleration lens is similar in operation).

Preliminary experimental evidence supports the simulation in figure 4.6. During performance testing it was noted that with the deceleration lens approximately 150 mm away from the PSD, the beam is focused by a voltage of 7.2 kV, compared to 7.5 kV, as suggested by the simulation. The ≈ 300 V discrepancy is probably because the simulation fails to account for the -350 eV/q space charge reduction in the initial energy of the ions (as discussed in section 3.1.1). Ions were simulated with an initial kinetic energy of 10 keV/q, when experimentally the ions had 9.65 keV/q. Assuming the focusing power of the decel-

---

[3]The last data point in figure 4.4c was removed from the fit to avoid distorting the near constant fit for values below 9750 V.

(a) Mean kinetic energy

(b) Mean velocity magnitude

(c) FWHM spread of ion parameters
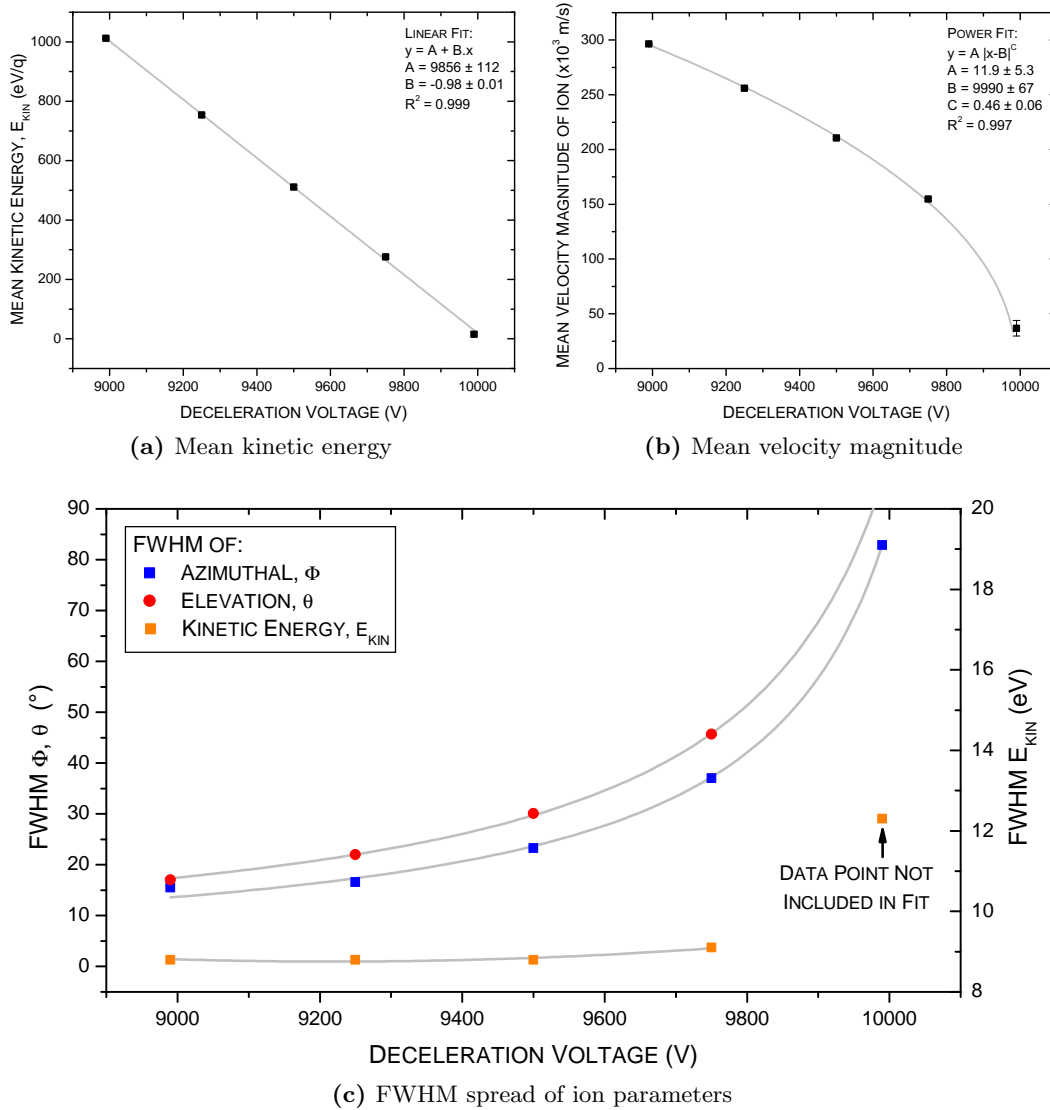
Figure 4.4: Summarised results of the simulations of the ion optical properties of the beamline as a function of deceleration voltage. The mean value of $\approx 400,000$ ions is shown, with the Full Width Half Maximum (FWHM) represented by the y-error bar in figures 4.4a and 4.4b. Figure 4.4c shows the change in FWHM with deceleration voltage. The fitting functions can be found in table A.3 of appendix A.4.

eration lens scales directly with the kinetic energy of the incoming ion, then the simulation and experiment are in agreement.

Figure 4.7 shows a comparison of a simulated beam profile (in the plane of the PSD) and the real experimental data for the same deceleration voltage (7.2 kV). The real image shows the physical limit of the detector (diameter 40 mm), as shown by uniform background counts which are not present in the simulation. The number of ions simulated is approximately the same that were incident upon the PSD, and the intensity count is
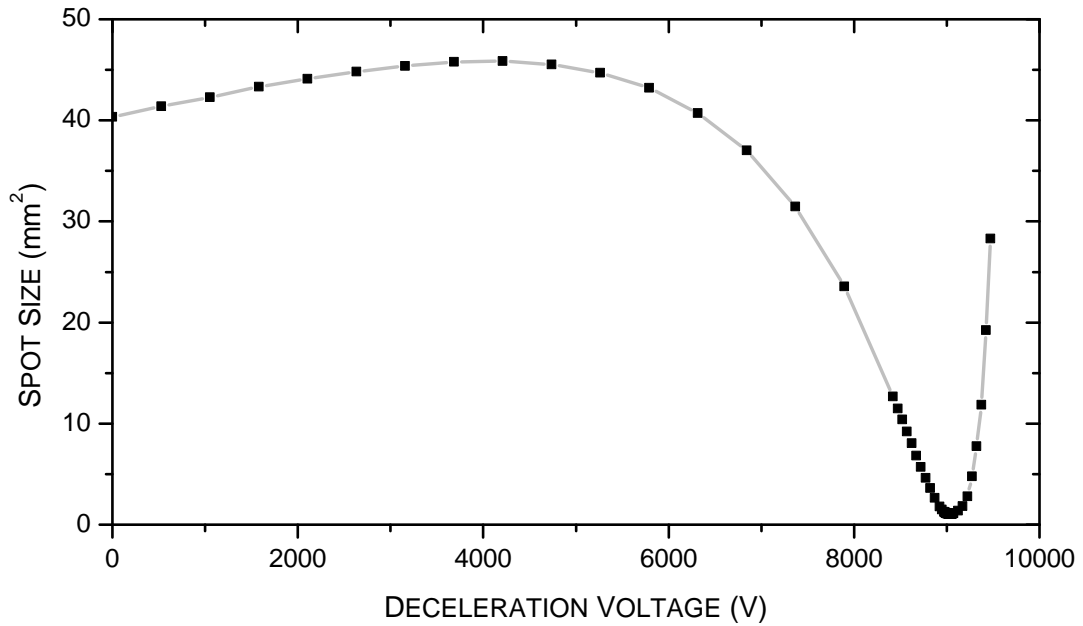
Figure 4.5: Example of the sampling process of the optimisation algorithm. The line drawn between data points is to guide the eye.
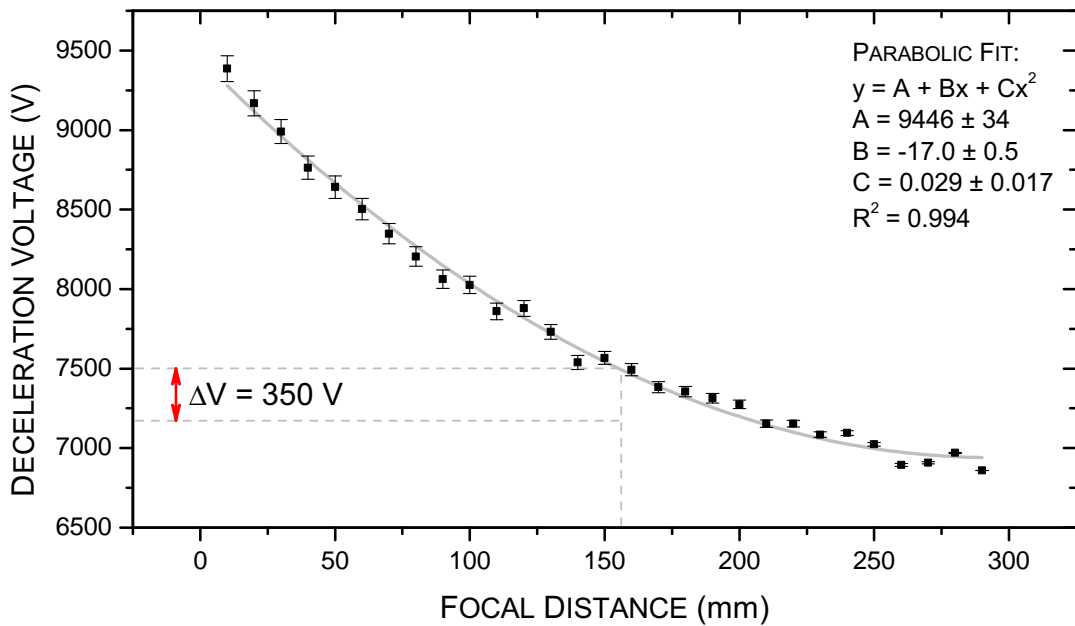
Figure 4.6: Simulation of the focal distance of the deceleration lens as a function of deceleration voltage. The focal distance is defined as the perpendicular distance along the beam axis from the tip of the lens to the focal point.

standardised for comparison. A slight asymmetry of the simulated beam spot is again

likely to be caused by a slight offset in electrode geometry.

(a) Simulated spot in detection plane   **(b)** Real spot seen on detector (PSD)
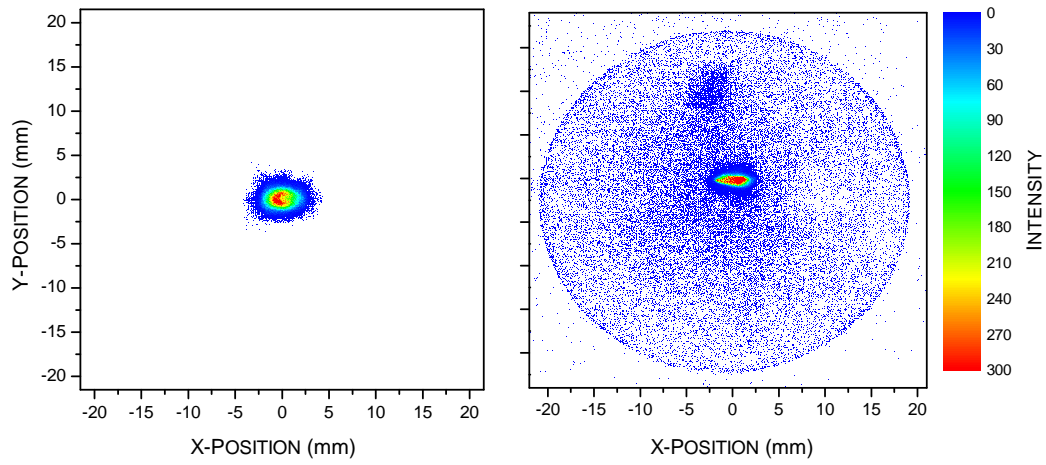
Figure 4.7: Comparison of simulated beam profile and optimised beam profile.

Chapter 5

Results & Conclusions

The first part of this chapter presents qualitative results of the ion optical properties of the beamline, obtained during performance testing, and comparisons to the simulation. In the latter part the results from the first two experiments of argon ions incident upon a neutral argon gas are given. Comparison of this data to existing experiments, and comments on their significance is discussed.

5.1 Performance Testing

In the following tests, the ion optical properties of the beamline were examined by comparing observed ions incident on the PSD. In the cases where intensities are directly compared, the same exposure time was used. Ion count rates in Hertz were calculated from the data's region of interest, where quantitative comparisons have been made.

(a) Before   (b) After
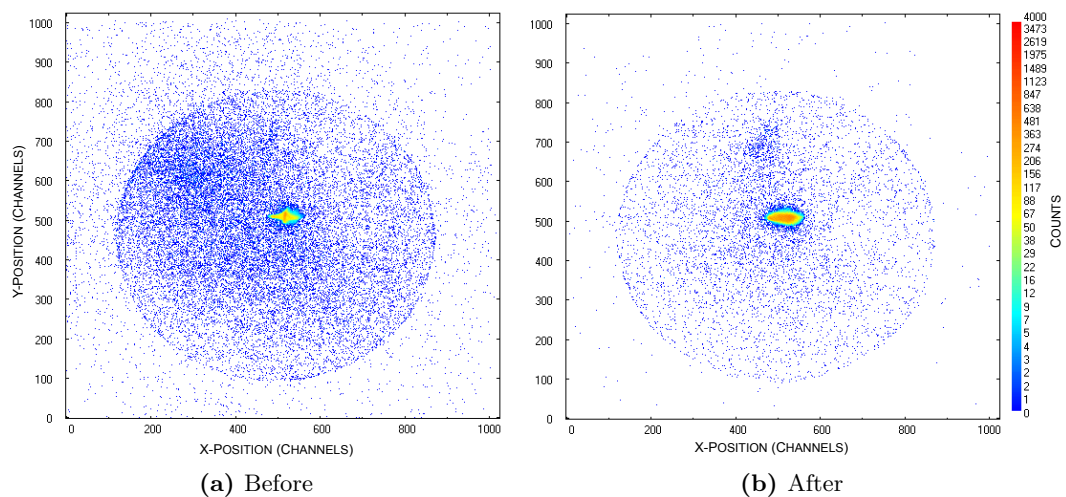
Figure 5.1: The effect of the Sikler lenses in correcting scattering and astigmatism of the beam.

The ability of the Sikler lenses to pre-focus and correct for astigmatism of the beam is shown in figure 5.1. In these two examples a 7.2 kV decelerated beam was tuned by

altering just the voltages applied to the two Sikler lenses. The before image shows strong astigmatism of the beam in both axes, and also a wide range of scattering to the top left of the image. Focusing the beam with the lenses resulted in improved count rates within the region of interest from 2.7 kHz to 3.9 kHz[1], with fewer scattered ions. Varying the astigmatic control of the lenses produced a more circular beam profile.

(a) Shadow at 0 kV   **(b)** Shadow at 8.6 kV
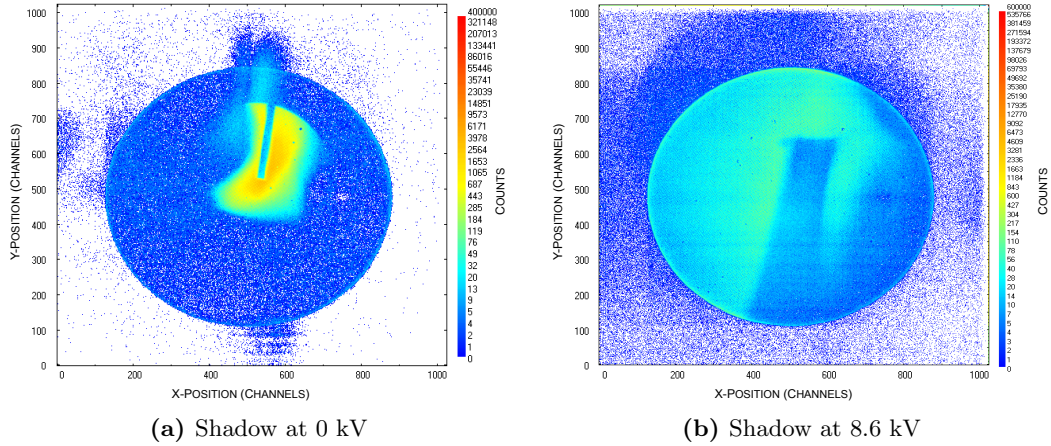
Figure 5.2: Moving the tip of the capillary gas tube into the beam casts a shadow upon the PSD. By increasing the deceleration voltage, it is possible to change the focal length of the lens to be shorter than the distance to the detector, causing the image of the tip to be inverted.

Figure 5.2 shows two images taken from the PSD. The first, figure 5.2a, is without deceleration and shows the shadow of the capillary tube, which was deliberately moved in front of the beam. The width of the capillary shadow is ≈ 1.3 mm in comparison to the real diameter of 2 mm. This suggests that beam is approximately parallel at this point, otherwise the resolution of the shadow would be poorer. The cutting of the beam on the left side of this image is the likely result of the beam striking a surface earlier in the beamline, as the sudden drop in beam intensity is well-defined. In comparison the right edge of the spot shows a more gradual decrease in counts, which would be expected as a result of the statistical nature of the beam.

Figure 5.2b provides evidence that the behaviour of the deceleration lens can be treated similarly to an optical lens. By increasing the potential applied to the lens, the shadow can be made to initially shrink as though using a converging lens. Beyond a voltage of 7.2 kV the image is inverted as the focal distance of the lens decreases to less than the distance between object (capillary tube) and real image. A rough approximation of the the focal length can be made using the thin lens magnification formula

$$\mathcal{M} = \frac{f}{f - d} \tag{5.1}$$

where $\mathcal{M}$ is the magnification, in this case ≈ 2.75, f is the focal distance and d is the distance between the object and the image. This gives a value of $f \approx 47$ mm for the

---

[1]Due to time constraints this test was performed with a less than average count rate, however similar results were experienced with a 20 kHz ion beam.

deceleration voltage of 8.6 kV. This value agrees approximately with the 8.4 kV (space charge corrected) value predicted by the simulation, as shown in figure 4.6 in section 4.7.

(a) Ion gauge off

(b) Ion gauge on

Figure 5.3: The chamber mounted ion gauge provides a significant source of background counts (these images each taken over an approximately 2 hour period). The comparative background count rates differ by three orders of magnitude, at 3.7 Hz and 2.1 kHz respectively.

Figure 5.3 shows two measurements of the background counts by the PSD over a two hour period. The left observation was obtained with all ion gauges switched off and the beamline vacuum gate valve (which isolates the deceleration beamline from the switch magnet) closed. The detector records a statistically distributed background at a rate of ≈ 3.7 Hz. This is four orders of magnitude less than ion count rates, observed to be ≈ 20 kHz, showing this background can be considered negligible.

With the ion gauge switched on however, the count rate rises to 2.1 kHz and the background becomes significant. The direct consequence of this test, was that all later experiments were performed with the chamber mounted ion gauge switched off. These observations also show that the detector is in good condition with few dead regions. The gradient in counts for figure 5.3b is a consequence of the geometry of the ion gauge in relation to the detector.

The effect of the deceleration lens on the beam is shown explicitly in figure 5.4. Increasing the voltage decreases the spot size accordingly until the focal distance matches the distance between lens and detector. Beyond this the inverse image of the beam is seen, which is then deflected away from the detector as the ion is decelerated to < 100 eV/q. This effect was often observed in the simulations: as the focusing power of the lens is increased near to the retarding potential limit, any asymmetries in the incident beam are magnified which can often result in the beam being scattered non-uniformly into the chamber walls.

The source of the counts found in the centre of the detector at 10 kV in figure 5.4i is unknown. The PSD is sensitive to soft X-rays and electrons [Epp07] so it is possible that X-rays or secondary particles emitted during ion-metal collisions in the beamline or the deceleration lens are being detected, however the interpretation of this phenomenon

(a) 0 kV   **(b)** 4 kV   **(c)** 5 kV

(d) 6 kV   **(e)** 7 kV   **(f)** 7.2 kV

(g) 8 kV   **(h)** 9 kV   **(i)** 10 kV

Figure 5.4: Testing the focusing effect of the deceleration at different voltages, each with an exposure time of 90 seconds. The transition from blue to yellow indicates increasing intensity. 1 - 3 kV are omitted, as there is no major difference in the beam profile until 4 kV. The voltage 7.2 kV is also included in the set as this is the point of minimum spot size before the focal distance of the lens becomes less than distance between the tip of the lens and the detector. As the voltage approaches 9 kV the beam is diffusely scattered over the top right edge of the detector, and at 10 kV is no longer visible, as expected for ions with an initial kinetic energy of 9.65 keV/q.

is still unclear.
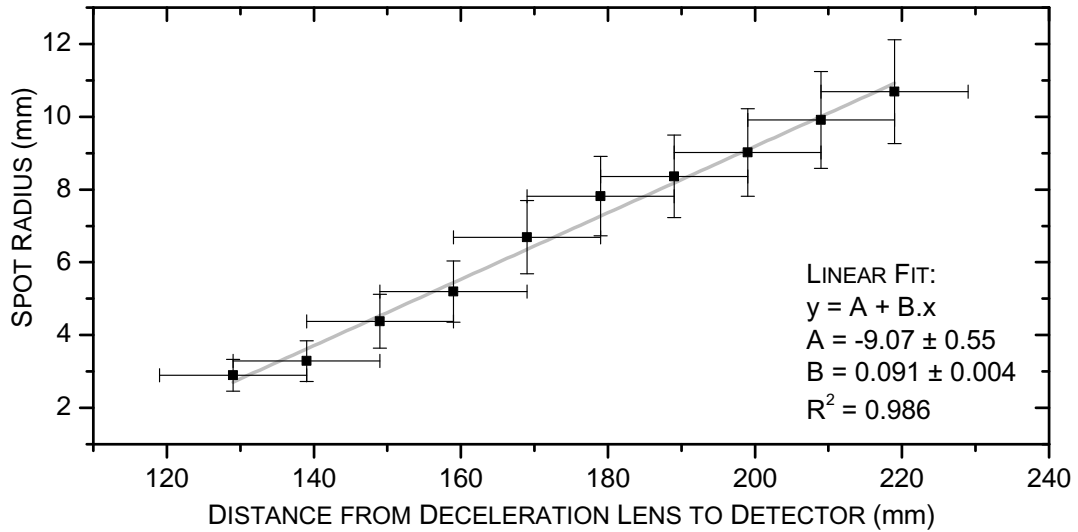
Figure 5.5: The beam spot radius scales linearly with the lens distance from the detector, providing evidence that the beam enters the deceleration beam approximately collimated. This test was carried out with a 7.2 kV deceleration voltage.

Figure 5.5 shows the results of a test to determine how the spot size changes as the position of the deceleration lens is altered. The deceleration lens is mounted on a transition stage, allowing it travel along the beam axis and the distance between lens tip and PSD to be altered. In this test the spot size on the PSD was measured as a function of the distance of the lens from the detector, defined as the distance from the tip of the lens to the first MCP. A distance of 120 mm corresponds to the tip of the lens directly in the centre of the target chamber. This test was conducted beginning with a focused beam at 7.2 kV on the detector. As expected, moving the lens away from the detector causes the spot size to increase. The data points exhibit a linear relationship, which suggests the angular divergence of the beam after it passes through the focal point is constant, as

$$\tan\left(\frac{\theta}{2}\right) = \frac{r_s}{d}$$

where θ is the angular divergence of the beam, r_s is the radius of the spot seen and d is the distance from the focal point to the detector. It therefore follows that $r_s \propto d$ when θ is a constant. This adds further evidence that the beam entering the deceleration lens is well collimated. From a linear fit of the data shown in figure 5.5 the angle θ is estimated to be

$$\theta = \arctan(2B) = 0.180 \pm 0.008 \text{ rad} = 10.3 \pm 0.5° \tag{5.2}$$

where B is the slope of the linear fit shown in the figure.

The x-error bar shows indicate the uncertainty in the distance, as only relative differences between lens positions are known accurately. The accuracy in determining the absolute distance between lens tip and PSD is limited by the uncertainty in determining the plane of detection in the PSD. However this uncertainty would affect all data

points equally and the subsequent calculation of θ from the slope of the linear fit would be unaffected.

5.2   Charge-exchange with Bare Argon Ions

The following offers a proof-of-principle for the deceleration beamline, and although data analysis and further experiments are ongoing, the first results are presented here.

The first experiment carried out with the new beamline used was Ar^{18+} incident on a neutral argon target. The results of coincidence spectroscopy between detected photons and ions, as described in section 3.5.2, are shown in figure 5.6. This data was collected over approximately 48 hours. Events were collected and recorded in a matrix according to photon energy, as shown along the x-axis, and the relative time interval between incoming photon and its corresponding ion, as shown on the y-axis.
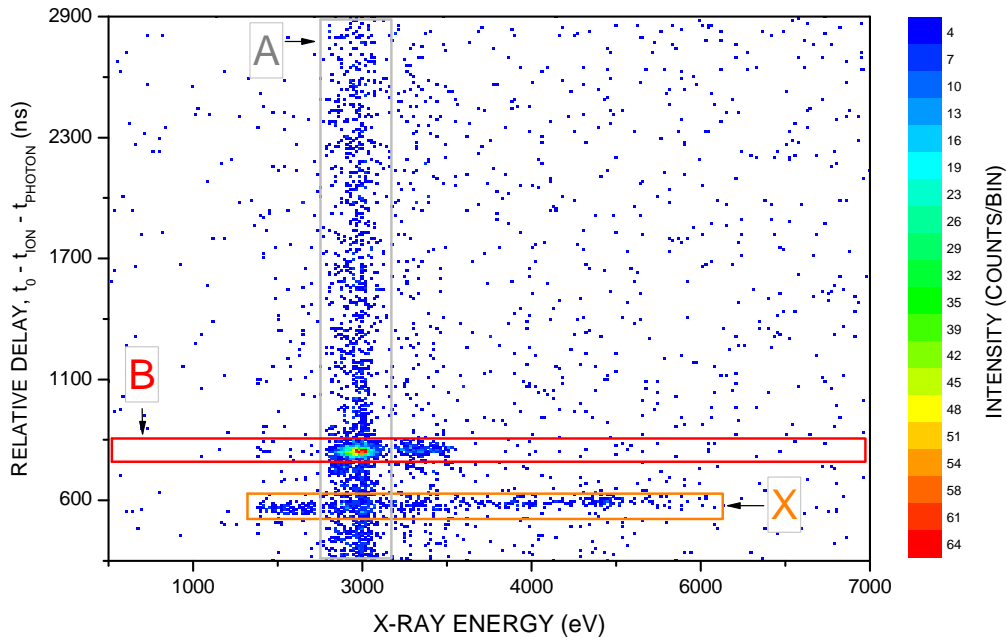
Figure 5.6: Coincidence spectra for Ar^{18+} incident upon neutral argon. The regions of interest are indicated by A, B and X.

Using figure 5.6 the photons of interest are isolated by defining a region of interest over the structures in the spectrum and projecting the data onto the x- and y- axes. Figures 5.8 and 5.7 show the resulting energy and time spectra respectively. Figure 5.7 shows the time difference between a detected photon and the next detected ion on the PSD. The absolute time delay t_0 cannot be determined as there are unknown time delays introduced by the detectors and the subsequent signal processing electronics, notated t_{ion} and t_{photon}.

In the time spectra a clear peak can be detected at ≈ 1050 ns, which is produced by the constant time delay between an ongoing projectile ion and charge exchange and the corresponding photon produced as it decays. As well as this peak there are two further
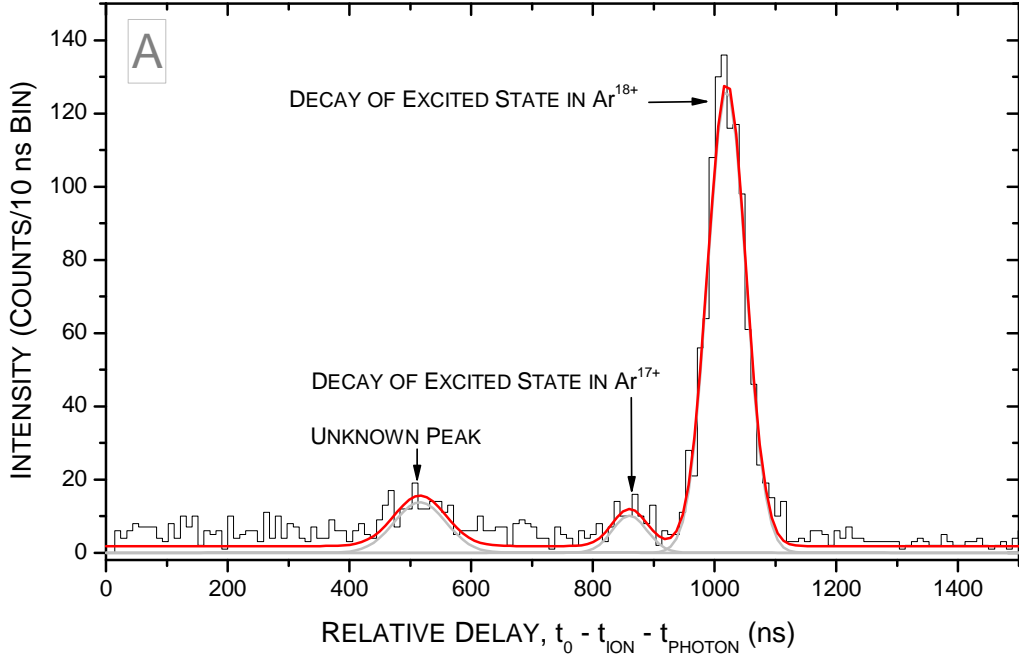
Figure 5.7: Time spectra showing the relative time difference between a photon detected by the X-ray detector and the next ion to be detected by the PSD. Events of interest occur at the same relative time interval.

smaller observed in the time spectra. The smallest, which lies close to the Ar^{18+} events is probably charge exchange between Ar^{17+} and neutrals. It is possible that Ar^{17+} is formed in the deceleration beamline, before reaching the deceleration lens. This could occur during charge exchange with residual gas in the vacuum, or more likely with neutral argon which moves into the beamline from the target chamber. Evidence that this peak is Ar^{17+} is given by calculating the theoretical time delay between two ions of differing charge states that are decelerated by the same retarding potential.

It is assumed that an Ar^{17+} ion formed in the beamline still has approximately the same kinetic energy it gained from escaping the EBIT as Ar^{18+}. The initial energy of the particle is given by

$$E_{init} = qeU_{EBIT} \tag{5.3}$$

where q is the initial charge state and U_{EBIT} is the effective potential seen by the ion gains leaving the trap, taking into account space charge losses.

After charge exchange in the beamline the ion then decelerated according to its new charge state q', as given by

$$E_{q'} = q'eU_{decel} \tag{5.4}$$

where U_{decel} is the retarding potential. Similarly an ion that did not undergo charge exchange loses kinetic energy

$$E_q = qeU_{decel} \tag{5.5}$$

during deceleration. The velocity of a particle with energy E is then given, as shown
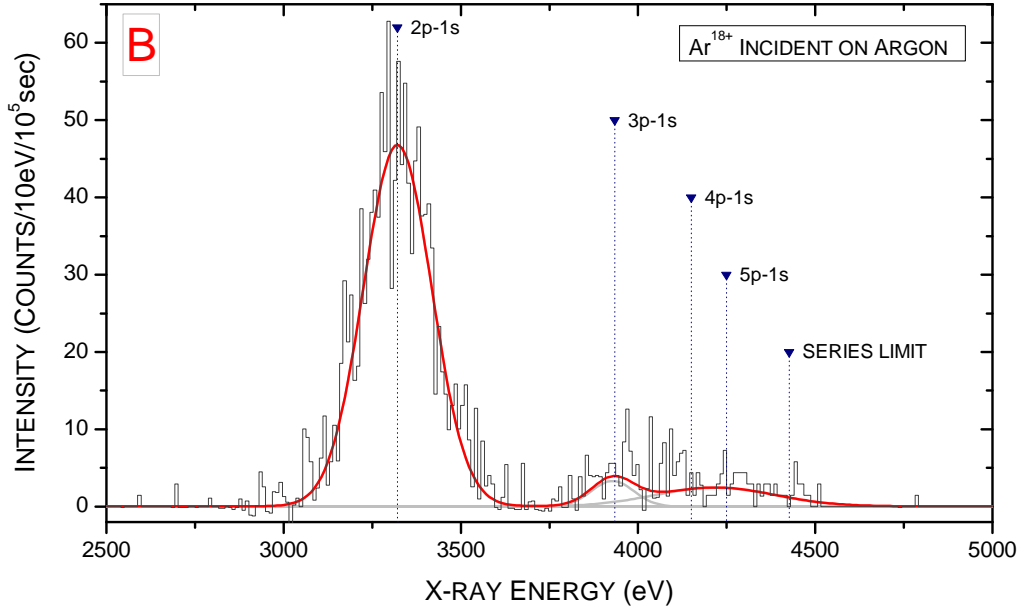
Figure 5.8: Energy spectrum of the region of interest marked in 5.6, showing the characteristic K series decays. The K-α peak indicated occurs at 3321 eV, in agreement with published emission energies for the Kα1 and Kα2 transitions, at 3318 and 3323 eV respectively [Bea67]. Other peaks are indicated for reference, with data taken from Ralchenko et al. [RKR09]. Non-zero intensities are due to corrections made to account for broadening of the original peak by a small number of captures by Ar^{17+} also occurring during the exposure.

previously, by

$$\nu = \sqrt{\frac{2E}{M}} \ . \tag{5.6}$$

Therefore Ar^{17+} formed in the beamline will have a greater velocity passing through the target chamber, as it experiences less deceleration than Ar^{18+}. This corresponds to a time of

$$t = \frac{d}{\nu} \tag{5.7}$$

to travel distance d between the region seen by the X-ray detector to the plane of ion detection. Therefore the time difference between decelerated ions of different charge states that have the same initial kinetic energy is given by

$$
\begin{aligned}
\Delta t =& d \left(\frac{1}{\nu_q} - \frac{1}{\nu_{q'}} \right) \\
=& d \left(\left(\frac{M}{2(E_{init} - E_q)} \right)^{\frac{1}{2}} - \left(\frac{M}{2(E_{init} - E_{q'})} \right)^{\frac{1}{2}} \right) \\
=& \left(\frac{d^2 M}{2} \right)^{\frac{1}{2}} \left(\frac{1}{(E_{init} - E_q)^{\frac{1}{2}}} - \frac{1}{(E_{init} - E_{q'})^{\frac{1}{2}}} \right)
\end{aligned}
\tag{5.8}
$$

where M, the mass of the ion in kg is related to atomic mass number m by equation 3.16,

thus giving

$$\Delta t = \left(\frac{d^2 m}{2u}\right)^{\frac{1}{2}} \left(\frac{1}{(E_{init} - E_q)^{\frac{1}{2}}} - \frac{1}{(E_{init} - E_{q'})^{\frac{1}{2}}}\right) \; . \tag{5.9}$$

For $q = 18$, $q' = 17$, $U_{EBIT} = 9650$ V (as according to section 3.1.1), $U_{decel} = 8990$ V and $d \approx 150$ mm this can be evaluated and gives a time difference of

$$\Delta t = 150 \pm 20 \text{ ns}$$

where the error arises from the uncertainty in the potential U_{EBIT}, and the detection distance d. This value agrees well with the 160 ± 5 ns relative time difference between the two peaks shown in figure 5.7, calculated using the fitting error of the Gaussians.

These time shifted events yield an energy spectrum with an apparent K-α peak, the energy of which is in an approximate agreement with the assumption that this peak reflects electron capture by Ar^{17+}. However the low level of statistics here make any definitive conclusion difficult.

The peak at approximately 500 ns on this figure, marked as region X in figure 5.6, is so far unexplained. Applying equation 5.9 for Ar^{16+} formed in the beamline gives a relative difference of ≈ 230 ns, which is too small for the relative delay seen here. Similarly the energy distribution of the these events does not support this proposal. The relatively high number of counts in this peak is also unusual. It could be an electronic artefact of the detection system, although further tests are required to prove or disprove this hypothesis.

5.3 Charge-Exchange with Hydrogen-like Argon Ions

Figure 5.9 shows the results from the same experiment, repeated using Ar^{17+} extracted from the EBIT. The time window used in this experiment is shorter than that used for Ar^{18+} at 0.5 μs and 5.0 μs respectively. This change was made along with adjustments to delays in the signal processing chain to increase the time resolution. The time spectra projected from figure 5.9 is shown in 5.10. Whilst it appears that the largest peak, identified from the energy spectra as Ar^{17+} K-shell transitions, has a lower peak intensity than that seen for Ar^{18+}, this is an artefact of the smaller binning used (0.5 ns compared to 10 ns).

The second peak shown in figure 5.10 probably originates from the decay of metastable Ar^{16+}, formed within the beamline. This is a different process to that seen in the Ar^{18+} coincidence spectra. Ar^{17+} travelling through the beamline captures an electron into an excited state, forming Ar^{16+}. If this electron then cascades to the 2s state, quantum angular momentum selection rules state the captured electron cannot decay via the E1 electric dipole transition, only via a forbidden M1, E2 or higher multipole transition. These have a much lower probability of occurring compared to the E1 transition, resulting in the Ar^{16+} ion existing as a metastable state, with a mean lifetime of 203 ± 12 ns [HT87]. This lifetime puts decelerated Ar^{16+} into the time window for detection. The energy spectrum for this state, shown in figure 5.12, provides further evidence that this a metastable state as only a single peak is present at 3107 eV, which agrees well with a decay from the $^3S_1$ state, which has a well known energy difference of 3104 eV [RKR09].
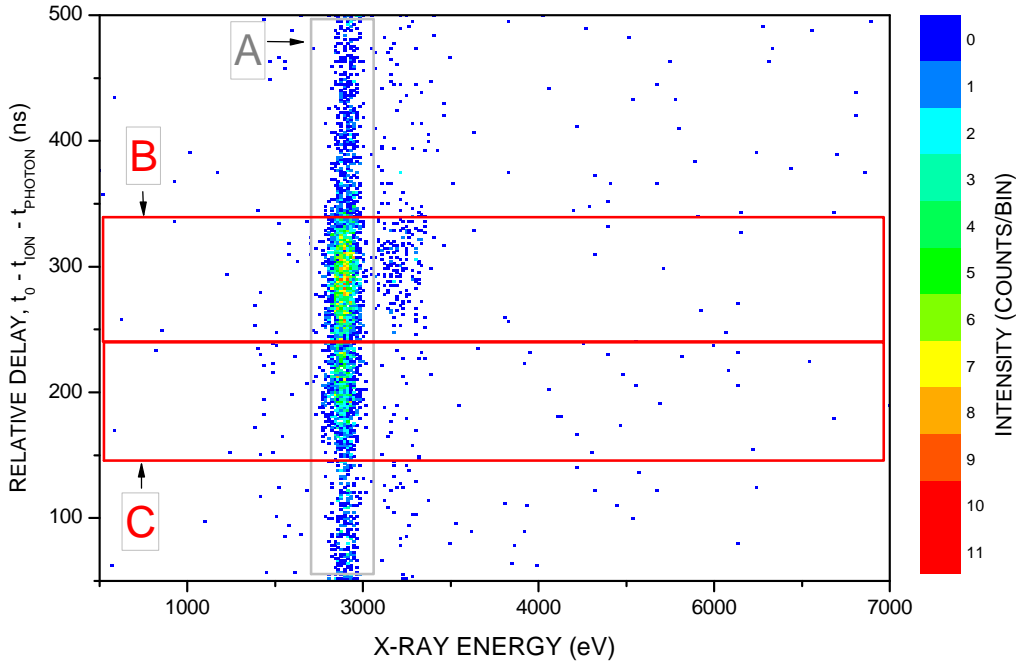
Figure 5.9: Coincidence spectrum for Ar^{17+} incident upon neutral argon. The regions of interest are indicated by A, B and C.

5.4   Comparisons to Existing Data

Results from other experiments provide a benchmark for the data collected here. Figure 5.13 shows a a spectrum from Allen et al. for Ar^{17+} incident upon neutral argon, for a projectile energy of 515 eV/q, compared to the same data collected here at 660 eV/q. The results show reasonable agreement, although the data collected here is limited by the low number of observed events.

From the energy spectra shown in the previous two sections it is possible to calculate a corresponding hardness ratio (as defined previously in section 2). This is defined as the total intensity of the higher order K transitions, normalised over the intensity of the K-α peak. Ratios of $\mathcal{H}(Ar^{18+}) = 0.186 \pm 0.010$ and $\mathcal{H}(Ar^{17+}) = 0.090 \pm 0.005$ for charge exchange with Ar^{18+} and Ar^{17+} respectively were calculated. These values are on average lower than those found by the Livermore, NIST and Berlin groups, as shown in figure 5.14.

This difference in ratios could provide evidence for further discrepancies in the CTMC model introduced in section 2, however given the relatively low event rates achieved experimentally (less than 0.02 Hz for photons of interest) and the relatively high signal-to-noise ratio of the spectra, further work has to be completed before any decisive comparison can be made.
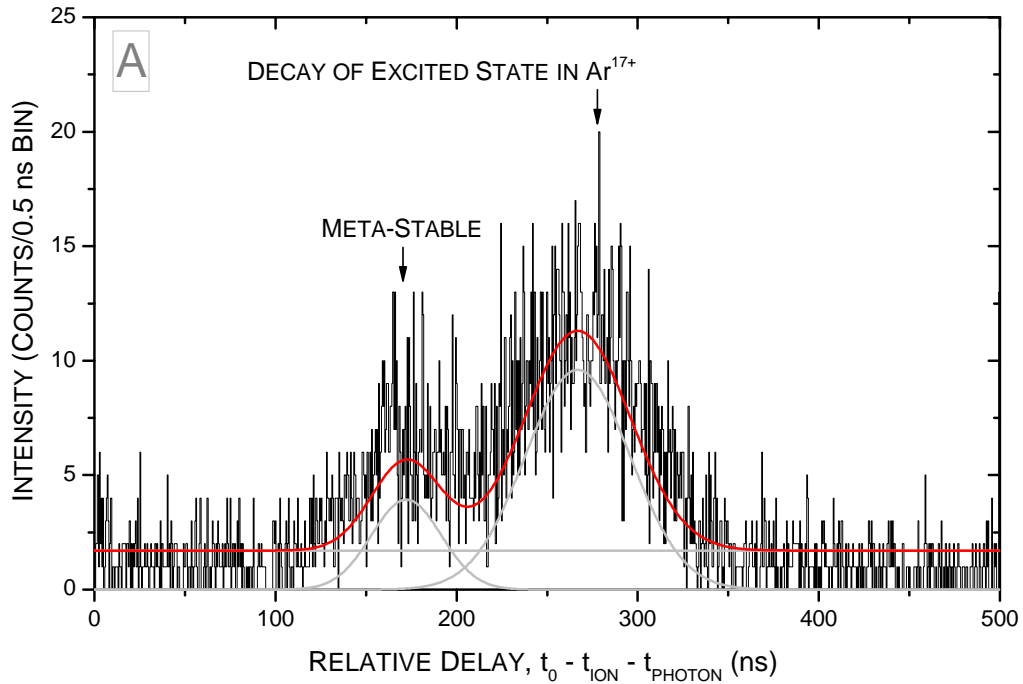
Figure 5.10: Time spectrum showing the relative time difference between a photon detected by the X-ray detector and the next ion to be detected by the PSD. Events of interest occur at the same relative time interval.

5.5 Conclusions

The hardness ratio $\mathcal{H}$ for the X-rays emitted as a result of electron capture by bare and hydrogen-like argon ions, from a neutral argon gas target has been calculated for projectile collisions at 660 eV/q, which lies in the relevant region for the interpretation of solar wind data.

Low background spectra can be obtained by using coincidence spectroscopy between X-rays and projectile ions. From the coincidence data it was possible to determine the photon energies of events of interest, which show excellent agreement with expected values for the Lyman-α and K-α transitions in Ar^{17+} and Ar^{16+} respectively.

Metastable ions were identified using time-of-flight information, supported by theoretical estimations. Corrections to the spectrum for electron capture by Ar^{18+} were also made as a result of this information, to remove a broadening of the Lyman-α peak due to a superposition of K-α events from electron capture by Ar^{17+}, occurring in the beamline before the target region.

Discrepancies with data from other groups could be explained if they had underestimated the influence of their X-ray background in their analysis. The coincidence spectroscopy method used here suffers far less from background giving confidence that the data presented here is reliable within its given error bars.
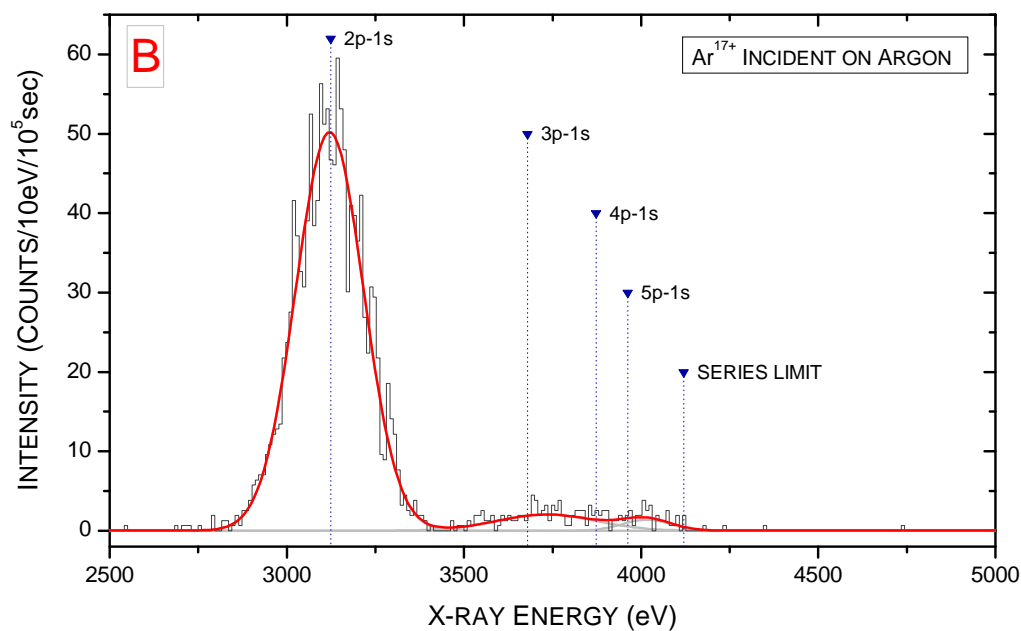
Figure 5.11: Energy spectrum of the region of interest marked in 5.6, showing the characteristic K series decays. The K-α peak indicated occurs at 3121 eV, in agreement with published emission energies for the Kα1 and Kα2 transitions, at 3124 and 3140 eV respectively [RKR09].
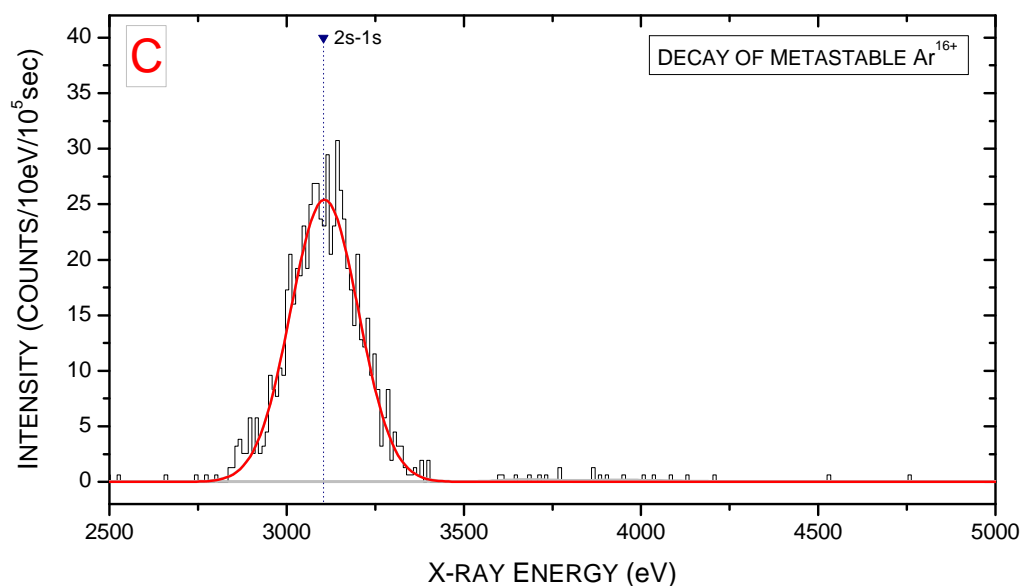
Figure 5.12: Energy spectrum for metastable Ar^{16+} formed in the beamline. The peak occurs at 3107.0 eV, compared to the 3104.1 eV published value [RKR09]. The lack of higher order K transitions also provides further evidence for this being the decay of a metastable state.
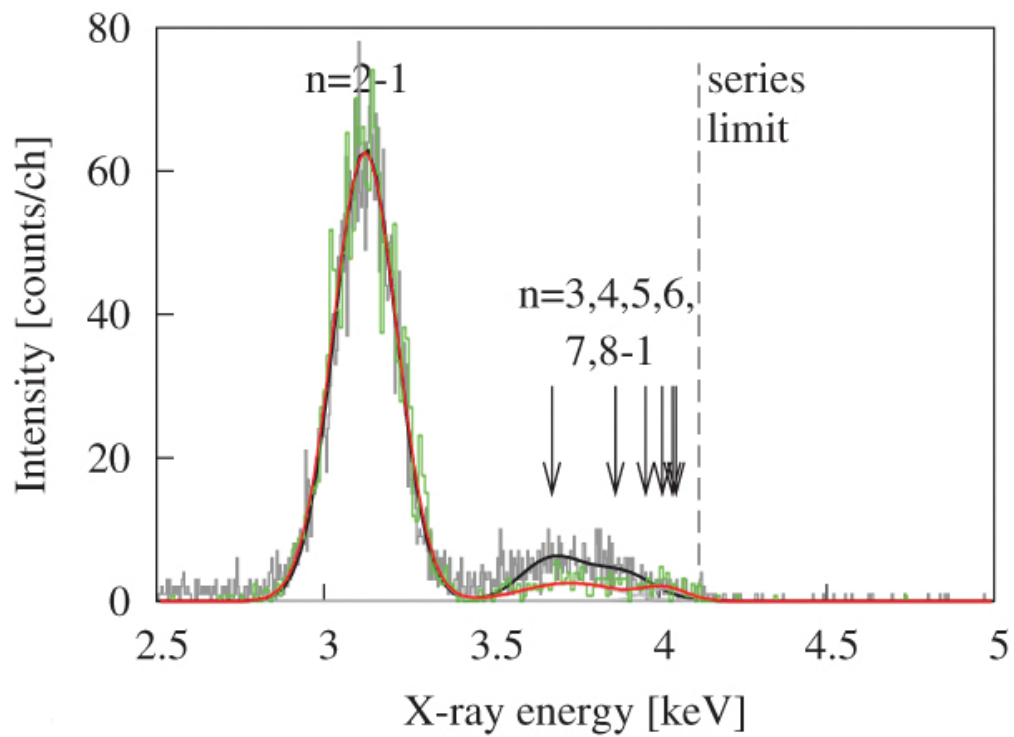
Figure 5.13: Ar^{17+} at 515 eV/q spectrum taken in in Berlin by Allen et al. [ABR$^+$08] (in grey and black) overlaid with the corresponding spectrum made here in Heidelberg at 660 eV/q (in green and red). Figure adapted from Allen et al. [ABR$^+$08], © The American Physical Society.
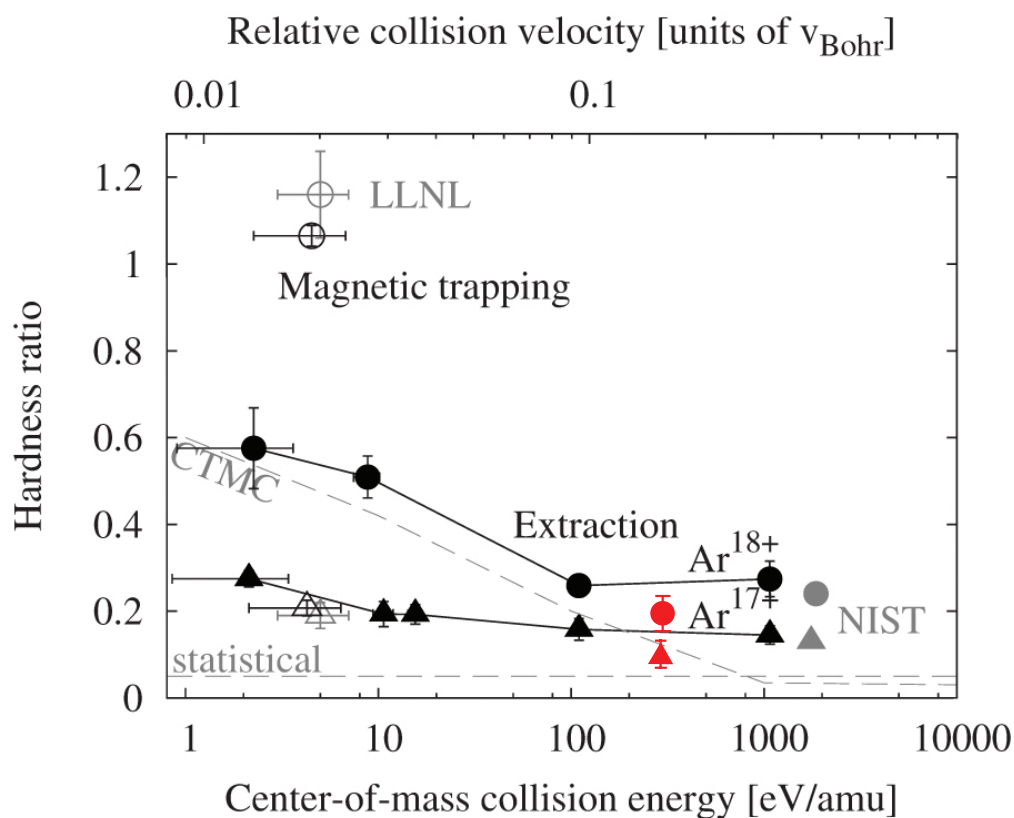
Figure 5.14: Experimentally observed hardness ratios versus collision energy from groups at Livermore and NIST (shown in grey), the Berlin EBIT (shown in black), and the new data presented here from Heidelberg (shown in red). The expected hardness ratio from CTMC calculations and statistical assumptions are shown with dashed lines. Figure adapted from Allen et al. [ABR+08], © The American Physical Society.

Chapter 6

Outlook & Evaluation

6.1   Outlook

During the next few months further experiments by colleagues and myself will be carried out with the new beamline, aiming to repeat the argon measurements over longer periods to improve statistics. Further performance testing will be carried out, including an experimental determination of the kinetic energy of the decelerated ions.

Plans are currently being made to improve the gas injection system. One proposal is to construct a gas cell inside the target chamber to increase the target gas density, and therefore the likelihood of charge exchange occurring. A time-of-flight spectrometer will also be installed in the target chamber, giving access to the recoil ion (the neutral from which an electron was captured). Measurements of the time of flight of this ion through a known distance and electric potential can be used to distinguish between single and multiple electron capture events.

Upon achieving better X-ray intensities, various projectile ions will be investigated, including carbon, magnesium and silicon. These ions are typically found in high abundance in the solar wind [G$^+$04], and the aim is to generate spectral data that can be used directly to interpret astrophysical observations.

6.2   Evaluation

It was soon realised after beginning, that the quantity of tasks required to install and bring the beamline to fruition, would mean not all of the original project aims could be fulfilled. For example constructing the time-of-flight spectrometer, initially one of the aims for this project, has consequently become a further thesis project for another colleague in the group, due to the amount of work involved. Whilst fortunately the work here has passed with few setbacks, the time-scales involved - such as the length of time required to assemble the ion optic and vacuum components in clean-room conditions, and the availability of EBIT beamtime, placed constraints on far the project could progress in the available time.

One area unfortunately unable to be included in this report was a further simulation algorithm written for the beamline. Unlike the optimisation algorithm, this was designed to test all possible permutations of a wide range beamline variables. An example of the results obtained by this algorithm is shown in figure A.4 in appendix A.4, a matrix of beam

spot sizes as a function of the two Sikler ion lens potentials. Whilst this data shows some interesting features, such as the difference in potential required to operate a symmetrical lens with either positive or negative polarity, a flaw in the logic of the algorithm was discovered in the shortly before the end of the project. The algorithm assumed that the focal strength of the deceleration lens is independent of divergence of the incoming beam, however this was recently shown not to be true. Hence artificially large or small spot sizes are recorded by the algorithm, which are just artefacts of the sampling plane of the simulation. As the processing time required to generate this and the nine further matrices not shown here was approximately 5 weeks, it was not possible to re-write the algorithm and run the simulation again. The algorithm will be corrected and developed further over the coming two months, to allow this data to be obtained.

However despite this, the project has progressed well overall and the first results show promising signs of the potential of the experiment to provide data that can be used to better interpret astrophysical spectra, and general understanding of charge exchange processes.

Appendix A

Technical Reference

A.1 Analysing Magnet Calibration

Figure A.1 shows the calibration data for converting between magnet control voltage and magnetic field. This relationship was derived from five settings of the control voltage, spread over the normal operating range. The plot shows strong linear correlation, and the slope, intercept and goodness of fit are shown.
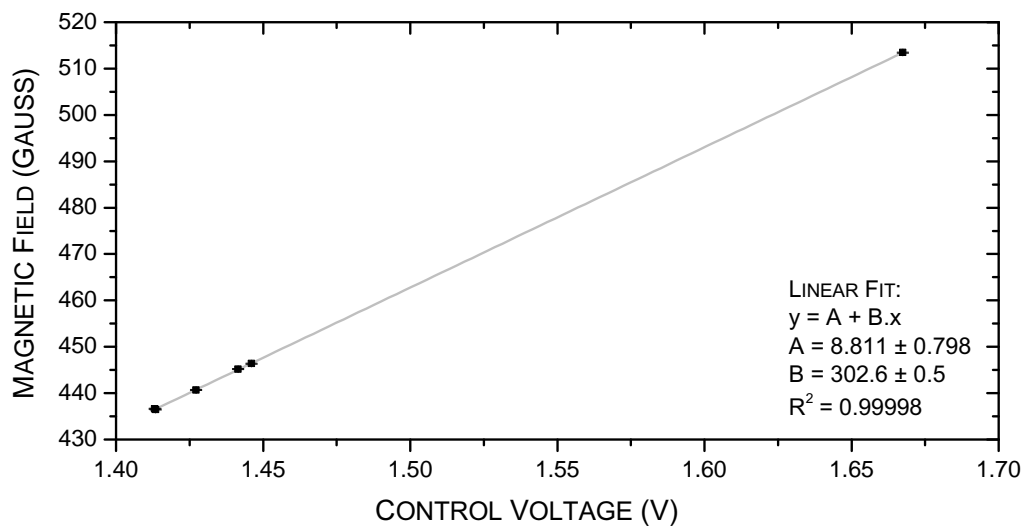
Figure A.1: Calibration graph for the analysing magnet scans. The data shows a strong linear relationship between magnet control voltage and the resultant magnetic field.

The constant given in equation 3.17 in section 3.2.2 for the relationship between q/m, U and B^2 was derived using the constants shown in table A.1.

A.2 X-ray Detector Calibration

Figure A.2 shows the spectra taken using a ^{57}Co source in order to calibrate the energy spectra for the Ar^{18+} and Ar^{17+} on neutral argon. Two spectra were taken over different

Quantity	Value	Unit
u	1.66×10^{-27}	[kg]
e	1.60×10^{-19}	[J]
r	0.522	[m]

Table A.1: Constants used in the derviation of equation 3.17 in section 3.2.2.
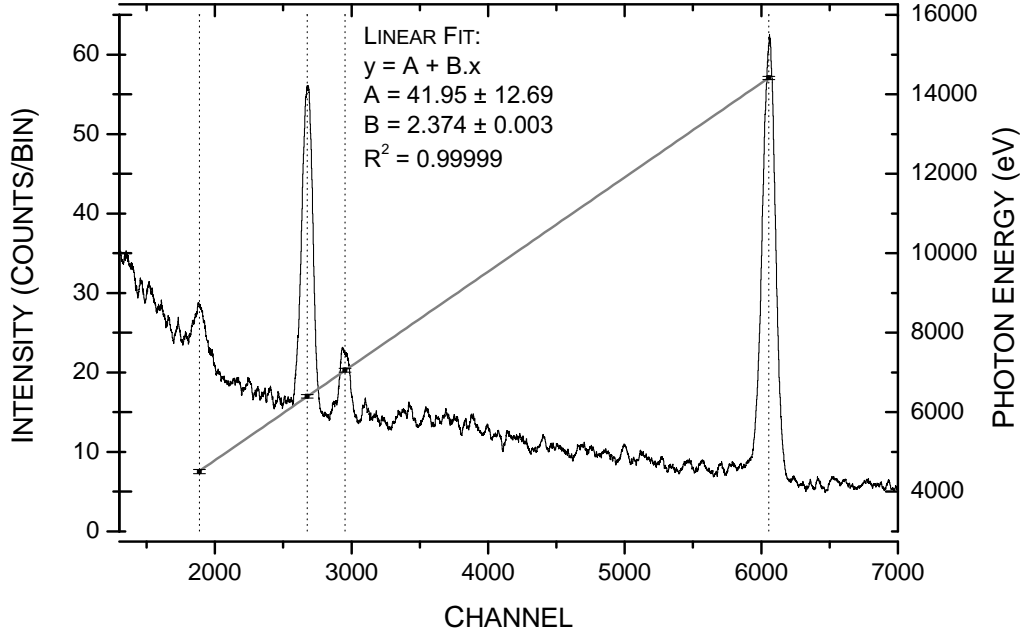
Figure A.2: Calibration spectra taken usin a ^{57}Co source.

sampling ranges of the data acquisition system to achieve better resolution in the lower energy range. The peaks were identified using data from Martinez [Mar05] and Gaussian fitted, the corresponding linear fit of these data points is shown. Table A.2 shows the peaks identified from the spectra.

A.3 Beamline Control Software

The EBIT, extraction beamline and deceleration beamline are all controlled using LabView programs[1]. During this project the deceleration beamline software, originally written by H. Bruhns was customised to allow remote monitoring of the beamline pressures. A pressure safety system was written, which monitors the beamline pressures. If any of the three pressure gauges report a pressure above a user-defined threshold, the system automatically reduces the voltage supplied to the high-voltage experimental platform to a user-specified value (typically 0 Volts). High-voltage breakdowns are detected by sudden increases in the beamline pressure and so this system acts as a spark detection fail-safe for protecting the

---

[1]See http://www.ni.com/labview/ for further information.

Peak	Energy (keV)
Ge escape peak	4.508
Fe K-α	6.398
Fe Kβ	7.058
Co^{57}	14.4129

Table A.2: Constants used in the derviation of equation 3.17 in section 3.2.2.
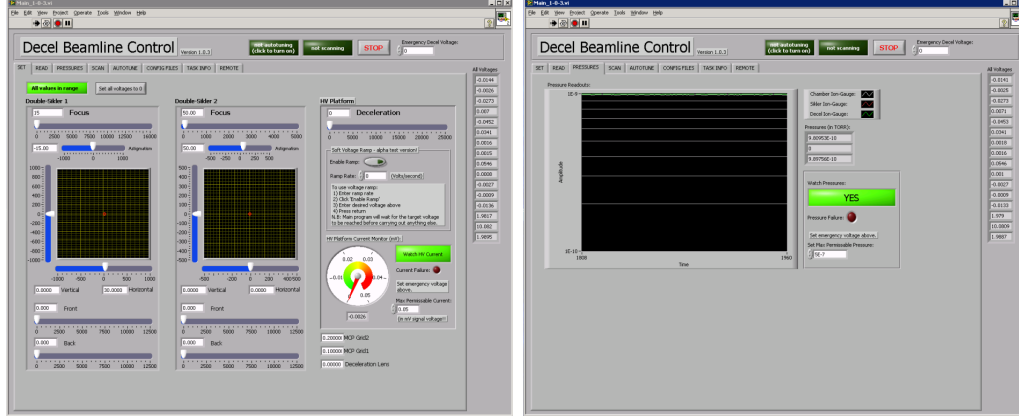
Figure A.3: Leak current and pressure monitoring safety systems were incorporated into the deceleration beamline control software.

beamline vacuum and electrodes against high-voltage arcing. This facilitates unattended operation of the beamline. A similar version of the code was implemented to monitor the current drawn by the high-voltage platform power supply. This typically remains below $< 25\ \mu A$, however rises during arcing or due to a leakage current i.e. an electrical fault or short circuit. Upon exceeding a user-defined threshold, the program again shuts the power supply down.

A.4   Simulation Numerical Values

Table A.3 shows the fitting functions used in figure 4.4c in section 4.7.

Figure A.4 shows an example result from a further optimisation algorithm written to

Variable	Equation	A	B
Φ	$y = \frac{A}{1+Bx}$	2.08 ± 0.04	$-9.79 \pm 0.01 (\times 10^{-5})$
θ	$y = \frac{A}{1+Bx}$	1.59 ± 0.06	$-9.82 \pm .01 (\times 10^{-5})$
E_{KIN}	$y = A + Bx^2$	108.3 ± 46.5	$1.17 \pm 0.53 (\times 10^{-6})$

Table A.3: Fitting functions and corresponding values for the simulation data shown in figure 4.4c in section 4.7.

investigate the effect of the Sikler lens potentials on beam spot size. A flaw in one of
the assumptions for this algorithm means however, that it is not possible to determine
whether the change in spot size shown here is a direct result of changing the Sikler lens,
or as the combination of other variables.
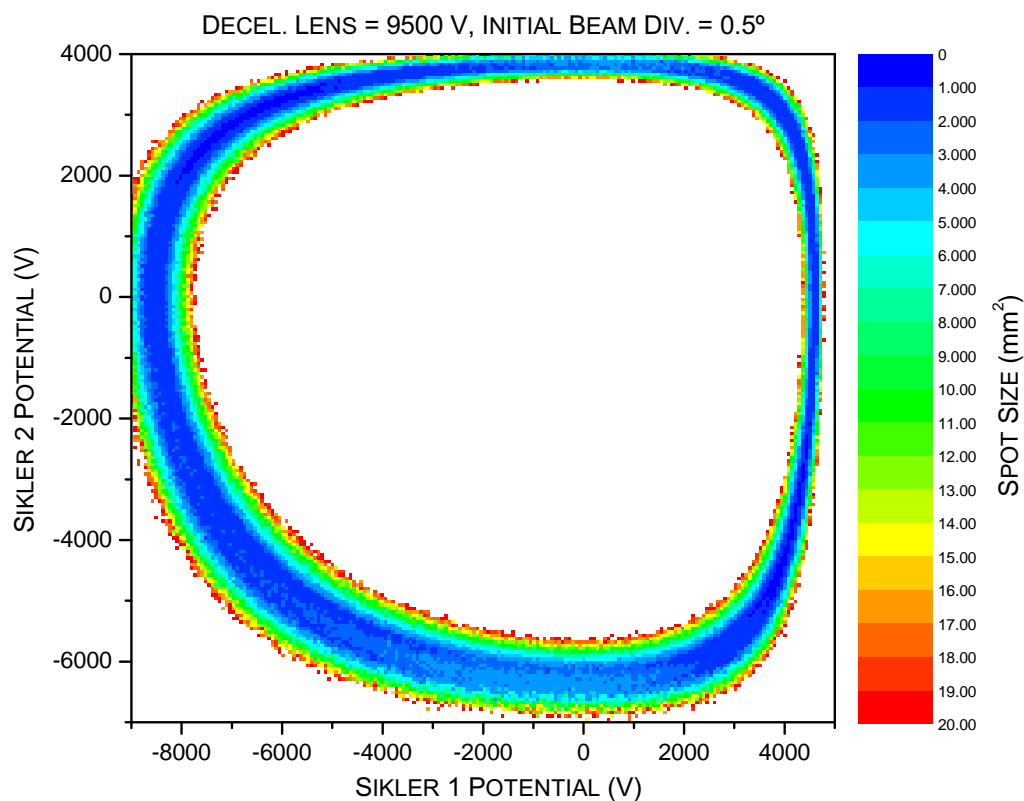
Figure A.4: Sample results from a further simulation algorithm, showing beam spot size as a
function of the two Sikler lens potentials. A flaw in this algorithm make it difficult to derive specific
information from the data.

Appendix B

Code Reference

The following appendix is included as a reference for the code used for the simulations.

Appendix B.1 contains the optimisation algorithm discussed in section 4.5 and the functions (program segments) which directly interact with SIMION. Appendix B.2 contains general Lua functions written for this project which are independent of the simulations. Appendix B.3 contains the scripts written to run SIMION in a batch operation mode.

B.1 Main Code

```
1  simion.workbench_program()
2
3  -- Record start time, import function library
4  start_time = os.time()                      -- Record start time (number of seconds since system defined epoch)
5  simion.import("SIM_funct_lib.lua")          -- Imports lua file of functions called in this program
6  date = format_date(os.date("*t"))           -- Format the current date and time into more usable form
7
8  -- Define user adjustable variables (and default values)
9  adjustable n_runs                           -- Number of desired iterations between Sikler 1 max/min potentials
10  adjustable n2_runs                          -- Number of desired iterations between Sikler 2 max/min potentials
11  adjustable n3_runs                          -- Number of desired iterations between decel max/min potential
12  adjustable n4_runs                          -- Number of desired iterations between angular divergence max/min angles
13  adjustable u_min                            -- Start test voltage (Sikler 1)
14  adjustable u_max                            -- Final test voltage (Sikler 1)
15  adjustable u2_min                           -- Start test voltage (Sikler 2)
16  adjustable u2_max                           -- Final test voltage (Sikler 2)
17  adjustable u3_min                           -- Start test voltage (decel)
18  adjustable u3_max                           -- Final test voltage (decel)
19  adjustable u4_min                           -- Start test angular divergence of source beam (degrees)
20  adjustable u4_max                           -- Final test angular divergence of source beam (degrees)
21  adjustable num_ions = 100                   -- Used to tell lua how many ions in each run (there is no direct link between particle definition file in SIMION and
       lua, but two values must be equal)
22  adjustable decel_flag                       -- Option to simulate with a varying (flag=1) or non varying (flag=0) decel lens potential
23  adjustable display_traj_flag                -- Option to view the flight paths of ions in the simulation window (on flag=1; off flag=0; default is off)
24  adjustable ang_div_flag                     -- Option to vary (flag=1) or non-vary (flag=0) the angular divergence of the source beam
25  adjustable success_percentage               -- Percentage of ions that must reach the target region for run to be considered successful
26  adjustable z_target                         -- The distance along the z axiz (mm), beyond which the ion is considered to be in the target region
27  adjustable mode                             -- Select run-mode (2-sikler, decel, ang div mode OR decel optimisation mode)
28  adjustable mode_pod                         -- Select the Point Of Detection, i.e. record data about the particles when they splat beyond the z_target plane, or as
        soon as they pass it
29  adjustable opt_sensitivity                  -- Specifies the maximum absolute difference between the spot size minimas (in mm^2) of consecutive optimisation runs
30                                              -- Smaller values means the minima search is finer (greater confidence that minima has been found). Should be used in
                                                   conjunction with the sample frequency (n3_runs)
31
32  -- Define derived global variables
33  u_delta = (u_max - u_min)/(n_runs-1)        -- Value to increment Sikler 1 potential by after each run
34  u2_delta = (u2_max - u2_min)/(n2_runs-1)    -- Value to increment Sikler 2 potential by after each series
35  u3_delta = (u3_max - u3_min)/(n3_runs-1)    -- Value to increment decel potential by after each set
36  u4_delta = (u4_max - u4_min)/(n4_runs-1)    -- Value to increment angular divergence by between successive trials
37  fail_fraction = 1-(success_percentage/100)  -- Calculates fraction of ions in a run required for the run to be declared a failure
38
39  -- Define counter-related variables
40  n_current = 1                               -- Current run counter
41  n2_current = 1                              -- Current series counter
42  n3_current = 1                              -- Current set counter
43  n4_current = 1                              -- Current trial counter
44  n5_current = 1                              -- Current round counter
45  n2_runs = n_runs                            -- Maximum number of runs/series (program only generates square potential matrices for the 2 siklers)
46  u_current = u_min                           -- Set current sikler 1 potential to user-inputted minimum voltage
47  u2_current = u2_min                         -- Set current sikler 2 potential to user-inputted minimum voltage
48  u3_current = u3_min                         -- Set current decel test voltage to user-inputted minimum voltage
49  u4_current = u4_min                         -- Set current angular divergence to user-inputted minimum
50  file_number = 1                             -- Used for indicating current results file number
51  fail_count = 0                              -- Counter for the number of ions that have failed to reach target region
52  min_spot_feedback = 0                       -- Initialise the minimum spot size feedback variable - allows for comparisons, has the spot size got bigger or smaller
       ?
```

```
53
54   -- Define flags
55   first_run_flag = 1                              -- Used to flag that the simulation has just started (do extra statements in initialize segment)
56   first_fail_flag = 1                             -- Used do determine whether first occurrence of a success_percentage failure (should one occur)
57
58   -- Define any other variables
59   pi = math.pi                                    -- Define global pi value
60   fly2_filename = 'SIM_VarDecel_Main.fly2'        -- Filename of the fly2 file used to define the beam in this simulation (NB: This is not perfect, ideally lua could
         read this value directly from SIMION, but this does not seem to be possible)
61   x_data = { }                     -- Create temporary results tables, populated with zeroes
62   y_data = { }
63   x_ke = { }
64   x_div = { }
65   vz = { }
66   spot_area_record = { }
67   ke_ions = { }
68   ke_error = { }
69   detect_ion = { }
70
71   logfile, lfname = create_file(2, date)          -- Create a log file
72   ifname = create_ionfile(fly2_filename, date)    -- Create a file with details of the ion definitions
73
74   function segment.initialize()                   -- initialize segment is called for each ion just after its creation, before flying, before init_p_values segment
75       first_fail_flag = 1                         -- Reset fail flags and counters for new run
76       fail_count = 0
77       if ang_div_flag == 1 then                   -- If selected, applies a cone distribution to the intialised particles
78           ion_vx_mm, ion_vy_mm, ion_vz_mm = cone_distribute_particle(ion_vx_mm, ion_vy_mm, ion_vz_mm, u4_current)
79       end
80       table.insert(detect_ion, ion_number, 1)     -- Creates a table of flags used to record whether a particle has already been detected
81       table.insert(ke_ions, ion_number, (vel_to_ke(ion_vx_mm, ion_vy_mm, ion_vz_mm, ion_mass)))  -- Records the KE of each initial ion
82       if display_traj_flag == 1 then
83           sim_trajectory_image_control = 1        -- Tells SIMION to draw the flight path of each ion in the window view (useful for debugging, but slow)
84       elseif display_traj_flag == 0 then
85           sim_trajectory_image_control = 3        -- Tells SIMION to not draw or store the flight path of the ion during the simulation (faster)
86       end
87   end
88
89   function segment.init_p_values()                -- init_p_values segment called for each instance (PA file) just after all the ions have been created, but before
         they are flown.
90
91       if first_run_flag == 1 and ion_instance == 1 then                   -- If first run of first series then set all electrodes to starting potential
92           validate_adj_var()                                              -- Calls function that validates the user inputted values, to catch errors
93           datafile, dfname = create_file(1, date, decel_flag, ang_div_flag, n3_current, n4_current)           -- Create first results file
94           if decel_flag == 0 then n3_current, n3_runs = 1, 1 end          -- Causes section of code in terminate segment to be ignored if decel potential not being
             varied
95           if ang_div_flag == 0 then n4_current, n4_runs = 1, 1 end        -- Causes section of code in terminate segment to be ignored if ang div not being varied
96
97           print_headers(decel_flag, ang_div_flag)                         -- Prints header information to screen/files
98           print_table_header(datafile)                                    -- Prints labels for table columns to the results file
99           first_run_flag = 0                                              -- After first run, clear flag so this code is not repeated
100      end
101
102      if ion_instance == 1 and mode == 1 then                             -- Only affects electrodes in PA instance 1 - The Sikler lenses
103          adj_elect01 = u_current                                         -- Fast adjusts electrode potentials
104          adj_elect02 = u_current
105          adj_elect03 = u_current
106          adj_elect04 = u_current
107          adj_elect07 = u2_current
108          adj_elect08 = u2_current
109          adj_elect09 = u2_current
```

```lua
110         adj_elect10 = u2_current
111         printx('Sikler 1 = ' .. u_current .. ' V', 1)
112         printx('Sikler 2 = ' .. u2_current .. ' V', 1)
113     elseif ion_instance == 2 then                          -- Only affects electrodes in PA instance 2 - The Decel Lens
114         adj_elect01 = u3_current
115         adj_elect02 = 0                                   -- Keeps the inner cylinder of the decel lens trumpet on earth
116         adj_elect03 = u3_current
117         if mode == 1 then
118         printx('Decel   = ' .. u3_current .. ' V', 1)
119         printx('Ang div = ' .. u4_current .. ' deg', 1)
120         end
121     end
122 end
123
124 function segment.other_actions()            -- other_actions segment is run by SIMION during every time step of the flight of every ion
125
126     -- Fail safe system - Checks if ion has splatted outside of target region
127     if ion_splat == -1 and ion_pz_mm <= z_target then
128         fail_count = fail_count + 1          -- Counts number of failed ions
129         if fail_count > (fail_fraction*num_ions) and first_fail_flag == 1 then  -- If number of failed ions exceeds threshold:
130             printx('* Warning: Percentage success threshold for this run was not met; data for this run will be nullified.', 1)
131             x_data, y_data, x_ke, x_div, vz = { }, { }, { }, { }, { }          -- Set results tables to 0 - ensures that false data won't be recorded
132             first_fail_flag = 0                                               -- Only do this once for each run
133         end
134     end
135
136     -- Check the other possible fates of an ion, recording if such an event occurs (rare)
137     if ion_splat == -2 then dead_in_water = 1
138     elseif ion_splat == -3 then out_wb = 1
139     elseif ion_splat == -4 then ions_killed = 1
140     end
141
142 -- ********************************************************
143 -- * mode_pod 0: Detecting particles only after they splat *
144 -- ********************************************************
145     if mode_pod == 0 then
146
147         if ion_splat == -1 and ion_pz_mm > z_target and first_fail_flag == 1 then   -- Only counts ion if no longer flying, and beyond the z_target limit, and if
148                 the fail threshold hasn't been exceeded
149             ke = speed_to_ke((v_mag(ion_vx_mm, ion_vy_mm, ion_vz_mm)),ion_mass)      -- calculates kinetic energy of ion from velocity vector
150             div = v_to_div(ion_vx_mm, ion_vy_mm, ion_vz_mm)                          -- Calculates angular divergance from velocity vector
151             table.insert(x_data, ion_px_mm)                                          -- Writes ion data to temporary result arrays
152             table.insert(y_data, ion_py_mm)
153             table.insert(x_ke, ion_number, ke)
154             table.insert(x_div, div)
155             table.insert(vz, ion_vz_mm)
156         end
157
158 -- ************************************************************************
159 -- * mode_pod 1: Detecting particles as soon as they pass a certain plane *
160 -- ************************************************************************
161     elseif mode_pod == 1 then
162
163         if ion_pz_mm >= z_target and detect_ion[ion_number] == 1 and first_fail_flag == 1 then
164             ke = speed_to_ke((v_mag(ion_vx_mm, ion_vy_mm, ion_vz_mm)),ion_mass)      -- calculates kinetic energy of ion from velocity vector
165             div = v_to_div(ion_vx_mm, ion_vy_mm, ion_vz_mm)                          -- Calculates angular divergance from velocity vector
166             table.insert(x_data, ion_px_mm)                                          -- Writes ion data to temporary result arrays
167             table.insert(y_data, ion_py_mm)
168             table.insert(x_ke, ion_number, ke)
169             table.insert(x_div, div)
```

```lua
169            table.insert(vz, ion_vz_mm)
170            detect_ion[ion_number] = 0                                    -- Flags that this ion has already been detected and recorded, so that it's
                    ignored during subsequent time steps
171            ion_color = 1                                                 -- Change the colour of the ion trajectory beyond the detection plane, useful
                    for debugging/visualisations
172          end
173       end
174    end
175
176    function segment.terminate()                 -- Terminate segment run by SIMION at the end of each flight of each ion, for each ion
177
178       if dead_in_water == 1 then printx('* Warning: Some ions were left dead-in-water during last run.', 1) dead_in_water = 0 -- Check if any of the other possible
                    ion fates occurred
179       elseif out_wb == 1 then printx('* Warning: Some ions ended up out of the workbench during last run.', 1) out_wb = 0     -- Print a warning if this is the case
180       elseif ions_killed == 1 then printx('* Warning: Some ions were killed during the last run.', 1) ions_killed = 0
181       end
182
183       -- Calculate error in KE energy i.e. the difference between the particles initial and final KE (simulation is fully elastic)
184       energy_loss = ion_charge*u3_current                          -- Take into account the loss of KE as a result of climbing decel potential hill
185       if x_ke[ion_number] ~= nil then                              -- Disregards ions that failed to reach target region - not of interest
186          theory_end_ke = ke_ions[ion_number] - energy_loss         -- Theoretical end KE  that the ion should have (start KE minus energy los due to potential
                    change)
187          simion_end_ke = x_ke[ion_number]                          -- Reads the actual KE of the ion at the point of detection
188          table.insert(ke_error, (theory_end_ke - simion_end_ke))   -- Records the discrepancy in a table
189       end
190
191       -- If last ion in the run then calculate spot size and record results
192       if ion_number >= num_ions then
193          spot_area = (stdev(x_data) * stdev(y_data) * pi)          -- Calculate ellipsoidal spot area inclusive of 2 st dev of all points(95%)
194          datafile:write(u3_current, '\t', u_current, '\t', u2_current, '\t', spot_area, '\t', mean(x_data), '\t', stdev(x_data), '\t', mean(y_data), '\t', stdev(
                    y_data), '\t', mean(x_ke), '\t', stdev(x_ke), '\t', mean(x_div), '\t', stdev(x_div), '\t', mean(vz), '\t', stdev(vz), '\t', mean(ke_error), '\t',
                    stdev(ke_error), '\n') -- Write result of run to datafile
195          theory_end_ke = { }                                       -- Delete temporary results tables to free up memory/reset for next run
196          simion_end_ke = { }
197          ke_error = { }
198          x_data = { }
199          y_data = { }
200          x_ke = { }
201          x_div = { }
202          vz = { }
203       end
204
205    -- ********************************************
206    -- * Brute-force Sikler/Decel Simulation Mode *
207    -- ********************************************
208
209       if mode == 1 then
210          -- If last ion in this run
211          if ion_number >= num_ions then
212             printx('Trial: ' .. n4_current .. ' Set: ' .. n3_current .. ' Series: ' .. n2_current .. ' Run: ' .. n_current .. ' completed.', 1) -- Print run
                    finished message to screen/log
213             n_current = n_current + 1                 -- Increment run counter
214             u_current = u_current + u_delta           -- Increment test voltage by u_delta
215          else
216             sim_rerun_flym = 1                        -- If not finished, flag simulation for rerun
217          end
218
219          -- If all runs but not all series completed
220          if n_current == n_runs+1 and n2_current ~= n2_runs then
221             sim_rerun_flym = 1                        -- Mark SIMION rerun flag
```

```lua
222             u_current = u_min                                      -- Reset electrode potentials/run counter
223             n_current = 1
224             n2_current = n2_current + 1                            -- Increment series counter
225             u2_current = u2_current + u2_delta                     -- Increment series test voltage (sikler 2 potential)
226         end
227
228         -- If all runs, all series, but not all sets completed
229         if n_current == n_runs+1 and n2_current == n2_runs and n3_current ~= n3_runs then
230             sim_rerun_flym = 1                                     -- Mark SIMION rerun flag
231             u_current = u_min                                      -- Reset sikler electrode potentials/run counters
232             n_current = 1
233             u2_current = u2_min
234             n2_current = 1
235             n3_current = n3_current + 1                            -- Increment set counter
236             u3_current = u3_current + u3_delta                    -- Increment set test voltage (decel potential)
237             datafile:flush()                                      -- Flush datafile - writes any data waiting in the buffer to the file
238             datafile:close()                                      -- Close the datafile
239             datafile, dfname = create_file(1, date, decel_flag, ang_div_flag, n3_current, n4_current)   -- Create a new results file for new decel potential
240             file_number = file_number+1                           -- Increment the file number counter
241             datafile:write('File ' .. file_number .. ' of ' .. (n3_runs*n4_runs))
242             if ang_div_flag == 1 then
243                 datafile:write('\n\nCurrent angular divergence (inital beam, degrees) = \t' .. u4_current)
244             end
245             print_table_header(datafile)
246             printx('- New results file created (next decel voltage), filename: ' .. dfname, 1)
247         end
248
249         -- If all runs, all series, all sets, but not all trials completed (i.e. Sikler1,2,decel finished, but not angular divergence)
250         if n_current == n_runs+1 and n2_current == n2_runs and n3_current == n3_runs and n4_current ~= n4_runs then
251             sim_rerun_flym = 1                                     -- Mark SIMION rerun flag
252             u_current = u_min                                      -- Reset sikler electrode potentials/run counters
253             n_current = 1
254             u2_current = u2_min
255             n2_current = 1
256             u3_current = u3_min
257             n3_current = 1
258             n4_current = n4_current+1                              -- Increment the trial counter
259             u4_current = u4_current + u4_delta                    -- Increment the trial test angle
260             datafile:flush()
261             datafile:close()
262             datafile, dfname = create_file(1, date, decel_flag, ang_div_flag, n3_current, n4_current)   -- Create a new results file for new ang divergence
263             file_number = file_number+1
264             datafile:write('File ' .. file_number .. ' of ' .. (n3_runs*n4_runs))
265             datafile:write('\nCurrent angular divergence (inital beam, degrees) = \t' .. u4_current .. '\n')
266             print_table_header(datafile)
267             printx('- New results file created (next angular div), filename: ' .. dfname, 1)
268             printx('- Max angular divergence of inital beam has been changed to ' .. u4_current .. ' degrees.', 1)
269         end
270
271         -- If all runs, series, sets and runs finished, i.e. Simulation is finished
272         if n_current == n_runs+1 and n2_current == n2_runs and n3_current == n3_runs and n4_current == n4_runs then
273             sim_rerun_flym = 0                                     -- Clear SIMION rerun flag - SIMION will then stop after this segment is finished
274             sim_retain_changed_potentials = 1                     -- Causes SIMION to leave electrodes at Umax setting
275             print_footers(start_time)                             -- Print information about duration of simulation to screen/log
276             datafile:close()                                      -- Close open files, releasing them for use by other programs
277             logfile:close()
278         end
279
280 -- ********************************
281 -- * Decel Lens Optimisation Mode  *
```

```
282   -- ********************************
283
284       elseif mode == 2 then
285
286           -- If last ion in the run
287           if ion_number >= num_ions then
288               spot_min = { u3_current, spot_area }              -- Create a record of the spot size at this test voltage
289               table.insert(spot_area_record, spot_min )          -- Insert this record into overall results table
290               printx("Decel test voltage: " .. u3_current, 1)
291               printx("Spot area:\t" .. spot_area, 1)
292               printx('Run ' .. n3_current .. ' completed.', 1)    -- Print run finished message to screen/log
293               n3_current = n3_current + 1                         -- Increment run counter
294               u3_current = u3_current + u3_delta                  -- Increment test voltage by u_delta
295           else
296               sim_rerun_flym = 1
297           end
298
299           -- If specified number of iterations are finished
300           if n3_current == n3_runs+1 then
301               min_result = search_spot_min(spot_area_record, n3_runs)      -- Search the spot size table to return minimum spot size and corresponding voltage
302
303               if min_result["voltage"] == 10000000 then          -- The search minimum function returns a voltage of 10,000,000 if all of the runs failed to detect
                      enough particles (according to fail parameters)
304                   printx("* error: No runs in the previous round fulfilled the successful run criteria - i.e. all ions ended up outside of target region - check
                          settings.", 1)
305                   printx('Simulation aborted.', 1)               -- This is a fatal error, stops simulation - the user needs to look more carefully at the settings
                          they've given
306                   error('No runs in the previous round fulfilled the successful run criteria - i.e. all ions ended up outside of target region - check settings.')
307               else
308                   printx("Min spot (" .. min_result["spot"] .. ") at " .. min_result["voltage"], 1)
309               end
310               printx("End of Round " .. n5_current, 1)
311
312               -- If the first pass (round) of the optimisation algorithm
313               if n5_current == 1 then
314                   diff = 1000000                                  -- Ensures that program does at least two passes
315               else
316                   diff = math.abs((min_result["spot"] - min_spot_feedback)/min_spot_feedback)      -- Otherwise find relative difference between this round and last
317                   printx("# Relative difference to previous round minimum: " .. diff, 1)
318               end
319
320               n5_current = n5_current + 1
321
322               -- If relative difference is less than specified sensitivity then algorithm is finished
323               if diff <= opt_sensitivity then
324                   print("# Relative difference is below threshold, minimum found")
325                   sim_rerun_flym = 0
326                   sim_retain_changed_potentials = 1              -- Causes SIMION to leave electrodes at Umax setting
327                   print_footers(start_time)                      -- Print information about duration of simulation to screen/log
328                   datafile:close()                               -- Close open files, releasing them for use by other programs
329                   logfile:close()
330               else
331                   min_spot_feedback = min_result["spot"]          -- Otherwise record this rounds value for comparison in next loop
332                   printx("# Continuing search...", 1)
333                   u3_min = min_result["voltage"] - u3_delta        -- Define new min/max test voltages, centered around the voltage that produced the last smallest
                          spot
334                   u3_max = min_result["voltage"] + u3_delta
335
336                   if u3_min < 0 then                              -- Stops the min test voltage from going below 0
337                       u3_min = 0
```

```lua
338                    printx("* Warning Previous run decided that minima lies near to 0, u3_min has been capped at 0 (<0 not allowed).", 1)
339                end
340
341                n3_current = 1                              -- Reset counter, set next test voltage
342                u3_current = u3_min
343
344                if (n3_runs%2) == 0 then                    -- Determines whether number of iterations is even, which causes problems as the same middle value
                        is sampled twice
345                printx("* Warning: n3_runs is even, one more run will be added to avoid sampling the same middle voltage", 1)
346                n3_runs = n3_runs+1
347                end
348
349                u3_delta = (u3_max - u3_min)/n3_runs        -- Calculate new delta value from new limits
350                min_result = { }                            -- Wipe temporary results tables
351                spot_area_record = { }
352                printx('# New u3_min = ' .. u3_min, 1)
353                printx('# New u3_max = ' .. u3_max, 1)
354                printx('# New u3_delta = ' .. u3_delta, 1)
355                sim_rerun_flym = 1                          -- Run the simulation again
356            end
357        end
358    end
359 end
360
361 function print_headers(d, a)
362    -- NB: This is not a self-contained function, as it prints variables that are assumed to already exist globally
363    printx('==================================', 1)           -- Print header information to screen/files
364    printx('Simulation started: ' .. os.date(), 1)
365    printx('==================================', 1)
366    printx('Warning this script will fail if ions are deflected by the first sikler lens. Consider Sikler potentials carefully!', 1)
367    printx('', 1)
368    printx('Logfile: ' .. lfname)
369    printx('Copy of fly2 file for this simulation: ' .. ifname, 1)
370    printx('', 1)
371    printx('User adjustable parameters:', 1)
372    printx('n_runs=' .. n_runs .. '\tn2_runs=' .. n2_runs .. '\tn3_runs=' .. n3_runs .. '\tu_min=' .. u_min .. '\tu_max=' .. u_max .. '\tu2_min=' .. u2_min .. '\
            tu2_max=' .. u2_max .. '\tu3_min=' .. u3_min .. '\tu3_max=' .. u3_max, 1)
373    printx('u4_min=' .. u4_min .. '\tu4_max=' .. u4_max .. '\tn4_runs=' .. n4_runs .. '\tnum_ions=' .. num_ions .. '\tdecel_flag=' .. decel_flag .. '\
            tdisplay_traj_flag=' .. display_traj_flag, 1)
374    printx('ang_div_flag=' .. ang_div_flag .. '\tsuccess_percentage=' .. success_percentage .. '\tz_target=' .. z_target, 1)
375    printx('', 1)
376    printx('Derived parameters:', 1)
377    printx('u_delta=' .. u_delta .. '\tu2_delta=' .. u2_delta .. '\tu3_delta=' .. u3_delta .. '\tu4_delta=' .. u4_delta .. '\tfail_fraction=' .. fail_fraction, 1)
378    printx('', 1)
379    if mode == 1 then string = "Brute-force Sikler/Decel simulation" elseif mode == 2 then string = "Decel Lens optimisation" end
380    printx('Mode: ' .. string, 1)
381    if mode_pod == 0 then string = "Record splats that occur beyond z_target plane" elseif mode_pod == 1 then string = "Record particles as soon as they pass the z
            -target plane" end
382    printx('Point-of-Detection: ' .. string, 1)
383    printx('', 1)
384    printx('File 1 of ' .. n3_runs*n4_runs, 3)
385    printx('Angular divergence of source beam = \t' .. u4_current .. ' degrees', 3)
386    if a == 0 then
387        printx('ang_div_flag = 0, initial angular divergence of beam will not be varied.', 1)
388    end
389    if d == 0 then              -- Check to see if decel lens potential is being investigated
390        printx('decel_flag = 0, decel lens potential will not be varied.', 1)
391    end
392    printx('==================================', 1)
393    printx('- New results file created, filename: ' .. dfname, 1)
```

```
394  end
395
396  function validate_adj_var()          -- Validates inputted adjustable variables to ensure within acceptable ranges
397      -- NB: This is not a self-contained function, it reads the values direct from the globally existing ones
398      if n_runs <= 0 then                                      -- Catches error of running simulation without stating how many runs are required
399          printx('error: The variable n_runs must be > 0 (cannot have a simulation without any runs)', 1)
400          printx('Simulation aborted.', 1)
401          error('The variable n_runs must be > 0 (cannot have a simulation without any runs)')
402      end
403      if decel_flag ~= 0 and decel_flag ~= 1 then              -- Catches error of having a non-boolean decel_flag
404          printx('error: The variable decel_flag may only be boolean (1=vary decel potentials or 0=leave decel fixed at preset potential)', 1)
405          printx('Simulation aborted.', 1)
406          error('The variable decel_flag may only be boolean (1=vary decel potentials or 0=leave decel fixed at preset potential)')
407      end
408      if decel_flag == 1 and n3_runs <= 0 then                 -- Catches error of trying to vary the decel potential for 0 runs
409          printx('error: The variable n3_runs must be > 0 as you have selected to vary the decel potential (decel_flag = 1)', 1)
410          printx('Simulation aborted.', 1)
411          error('The variable n3_runs must be > 0 as you have selected to vary the decel potential (decel_flag = 1)')
412      end
413      if display_traj_flag ~= 0 and display_traj_flag ~=1 then    -- Catches error of having non-boolean display_traj_flag
414          printx('error: The variable display_traj_flag may only be boolean (1=show the flight paths of ions, 0=hide flight path of ions)', 1)
415          printx('Simulation aborted.', 1)
416          error('The variable display_traj_flag may only be boolean (1=show the flight paths of ions, 0=hide flight path of ions)')
417      end
418      if ang_div_flag ~= 0 and ang_div_flag ~=1 then           -- Catches error of having non-boolean ang_div_flag
419          printx('error: The variable ang_div_flag may only be boolean (1=vary the initial beam divergence, 0=use predefined settings from fly2 file)', 1)
420          printx('Simulation aborted.', 1)
421          error('The variable ang_div_flag may only be boolean (1=vary the initial beam divergence, 0=use predefined settings from fly2 file)')
422      end
423      if u4_min < 0 then                                       -- Catches error of having a negative angular divergence
424          printx('error: u4_min < 0, i.e. min beam divergence is negative - not allowed.', 1)
425          printx('Simulation aborted.', 1)
426          error('u4_min < 0, i.e. min beam divergence is negative - not allowed.')
427      end
428      if u3_max < u3_min then                                  -- Catches error of having max beam divergence smaller than min beam divergence
429          printx('error: u3_max < u3_min, please check user inputted values for decel potentials.', 1)
430          printx('Simulation aborted.', 1)
431          error('u3_max < u3_min, please check user inputted values for decel potentials.')
432      end
433      if u4_max < u4_min then                                  -- Catches error of having max beam divergence smaller than min beam divergence
434          printx('error: u4_max < u4_min, please check user inputted values for initial beam divergence.', 1)
435          printx('Simulation aborted.', 1)
436          error('u4_max < u4_min, please check user inputted values for initial beam divergence.')
437      end
438      if u2_max < u2_min then                                  -- Catches error of having max sikler voltage smaller than min sikler voltage
439          printx('error: u2_max < u2_min, please check user inputted values for Sikler 2 max/min potentials.', 1)
440          printx('Simulation aborted.', 1)
441          error('u2_max < u2_min, please check user inputted values for Sikler 2 max/min potentials.')
442      end
443      if u_max < u_min then                                    -- Catches error of having max sikler voltage smaller than min sikler voltage
444          printx('error: u_max < u_min, please check user inputted values for Sikler 1 max/min potentials.', 1)
445          printx('Simulation aborted.', 1)
446          error('u_max < u_min, please check user inputted values for Sikler 1 max/min potentials.')
447      end
448      if ang_div_flag == 1 and n4_runs <= 0 then               -- Catches error of trying to vary ang div without giving a valid number of attempts
449          printx('error: The variable n4_runs must be > 0 as you have selected to vary the angular divergence (ang_div_flag = 1)', 1)
450          printx('Simulation aborted.', 1)
451          error('The variable n4_runs must be > 0 as you have selected to vary the angular divergence (ang_div_flag = 1)')
452      end
453      if num_ions <= 0 then                                    -- Catches error of trying to run simulation with less than one ion
```

```
454        printx('error: num_ions <= 0, cannot run a simulation without any ions!', 1)
455        printx('Simulation aborted.', 1)
456        error('num_ions <= 0, cannot run a simulation without any ions!')
457    end
458    if success_percentage < 0 or success_percentage > 100 then  -- Catches error of inputting success <0% or >100%
459        printx('error: success_percentage < 0% or >100%, please check inputted value', 1)
460        printx('Simulation aborted.', 1)
461        error('success_percentage < 0% or >100%, please check inputted value')
462    end
463    if z_target > 2715 or z_target < 0 then                    -- Catches error of setting z_target area outside of workbench
464        printx('error: z_target is outside of workbench, please check inputted value', 1)
465        printx('Simulation aborted.', 1)
466        error('z_target is outside of workbench, please check inputted value')
467    end
468    if opt_sensitivity <= 0 and mode == 2 then                 -- Catches error of setting opt_sensitivity <= 0
469        printx('error: opt_sensitivity is <= 0. Must be greater than 0 unless you really want to do an infinite number of iterations...', 1)
470        printx('Simulation aborted.', 1)
471        error('opt_sensitivity is <= 0. Must be greater than 0 unless you really want to do an infinite number of iterations...')
472    end
473    if mode ~= 1 and mode ~=2 then
474        printx('error: Incorrect mode selected. valid options are: 1 (Brute-force Sikler/decel mode) or 2 (Decel lens optimisation mode).', 1)
475        printx('Simulation aborted.', 1)
476        error('Incorrect mode selected. valid options are: 1 (Brute-force Sikler/decel mode) or 2 (Decel lens optimisation mode).')
477    end
478    if mode_pod ~= 0 and mode_pod ~= 1 then
479        printx('error: Incorrect mode_pod (point of detection) selected. valid options are: 0 (detect when ions splat beyond z_target limit) or 1 (detect when ions
               pass plane specified by z_target).', 1)
480        printx('Simulation aborted.', 1)
481        error('Incorrect mode_pod (point of detection) selected. valid options are: 0 (detect when ions splat beyond z_target limit) or 1 (detect when ions pass
               plane specified by z_target).')
482    end
483    if u_min == u_max or n_runs == 1 then u_delta = 0 end      -- Protects delta values from returning infinite errors
484    if u2_min == u2_max or n2_runs == 1 then u2_delta = 0 end
485    if u3_min == u3_max or n3_runs == 1 then u3_delta = 0 end
486    if u4_min == u4_max or n4_runs == 1 then u4_delta = 0 end
487 end
```

B.2   Function Library

```
1  function format_date(t)                      -- Function for reformatting date table into more user friendly format
2      if t["month"] < 10 then
3      t["month"] = 0 .. t["month"]
4      end
5      if t["day"] < 10 then
6      t["day"] = 0 .. t["day"]
7      end
8      if t["hour"] < 10 then
9      t["hour"] = 0 .. t["hour"]
10     end
11     if t["min"] < 10 then
12     t["min"] = 0 .. t["min"]
13     end
14     return t
15 end
```

```lua
16
17  function create_file(t, da, d, a, n3, n4)    -- Creates data file, prints header and returns file reference
18      if t == 1 then ext = ".txt" elseif t == 2 then ext = "_LOG.log" elseif t == 3 then ext = ".fly2" end
19      if d == 1 then sect = ("_D" .. n3) else sect = "" end
20      if a == 1 then sect2 = ("_A" .. n4) else sect2 = "" end
21      local filename = "SIM_" .. da["year"] .. da["month"] .. da["day"] .. "_" .. da["hour"] .. da["min"] .. sect2 .. sect .. ext
22      local file = io.open(filename,"a+")
23      return file, filename
24  end
25
26  function printx(string, x)                   -- Customised print function, that uses argument x to determine where string should be printed
27      -- NB: This is not a self contained function, it requires that the globals 'logfile' and 'datafile' already exist.
28      if x == 1 then
29      print(string)
30      logfile:write('\n', os.date(), '\t', string)
31      logfile:flush()
32      elseif x == 2 then
33      print(string)
34      datafile:write(string, '\n')
35      datafile:flush()
36      logfile:write('\n', os.date(), '\t', string)
37      logfile:flush()
38      elseif x == 3 then
39      datafile:write(string, '\n')
40      datafile:flush()
41      else
42      print(string)
43      end
44  end
45  function print_footers(t)                    -- Prints information about the duration of the simulation to the screen/log
46      printx('===================================', 1)
47      printx('Game Over.', 1)
48      printx('Start time:\t' .. os.date("%x %X", t), 1)
49      printx('End time:\t' .. os.date("%x %X"), 1)
50      printx('Program duration:\t' .. os.difftime(os.time(), t) .. ' seconds', 1)    -- Calculates the time the simulation took to run
51      printx('===================================', 1)
52  end
53
54  function print_table_header(f)               -- Prints column titles, plus units row to the file given as argument
55          f:write('\ndecel lens potential', '\t', 'sikler1 potential', '\t', 'sikler2 potential', '\t', 'spot area', '\t', 'x pos mean', '\tx pos stdev', '\ty pos
                 mean', '\ty pos stdev', '\tke mean', '\tke stdev', '\tdiv mean', '\tdiv stdev', '\tvz mean', '\tvz stdev', '\tKE error mean', '\tKE error stdev')
56          f:write('\nV\tV\tV\tmm^2\tmm\t \tmm\t \teV.q\t \tdegrees\t \tmm/microsec\t\teV\n')
57          f:flush()
58  end
59
60  function search_spot_min(t, y)
61      min = { ["voltage"]=10000000, ["spot"]=10000000 }        -- Initial comparison values at +"infinity"
62      for x=1,y,1 do
63      temp = t[x][2]
64          if temp < min["spot"] and temp ~= 0 then             -- NOT equal to 0 required as 0 is defined as missing value
65              min = { ["voltage"]=t[x][1], ["spot"]=t[x][2] }
66          end
67      end
68      return(min)
69  end
70
71  function mean(t)                             -- Accepts a table of values as argument and returns the mean of these values
72      local sum = 0
73      for i, v in ipairs(t) do
74      sum = sum + t[i]
```

```
75      end
76      if sum ~= 0 then return sum/(table.maxn(t)) else return 0 end   -- Returns a 0 (as opposed to an inf error) if table was empty
77  end
78
79  function stdev(t)                       -- Accepts a table of values as argument and returns the sample standard deviation of these values
80      local sum = 0
81      local avg = mean(t)
82      for i, v in ipairs(t) do
83      sum = sum + (math.pow((t[i] - avg),2))
84      end
85      if sum ~= 0 then return math.sqrt(sum/(table.maxn(t)-1)) else return 0 end -- Note: N-1 used as simulation is a sample of infinite parent population. Returns 0
            if table was empty
86  end
87
88  function v_to_div(vx, vy, vz)           -- Returns angle between inputted vector and the experiment's defined direction vector
89      local nvx, nvy, nvz = 0, 0, 1       -- Axis of beamline is defined as +z direction
90      return math.deg( math.acos( ((vx*nvx) + (vy*nvy) + (vz*nvz) )/((v_mag(vx, vy, vz))*(v_mag(nvx, nvy, nvz))) ) ) -- Dot product
91  end
92
93  function v_mag(vx, vy, vz)              -- Returns the magnitude of an inputted vector
94      return math.sqrt( ((vx)^2) + ((vy)^2) + ((vz)^2) )
95  end
96
97  function vel_to_ke(x, y, z, m)
98      return speed_to_ke((v_mag(x, y, z)),m)
99  end
100
101 function cone_distribute_particle(x, y, z, ang)     -- Random cone distribution code adapted from SIMION 8.0 example 'Random' (credit D.Manura)
102         local speed, az, el = rect3d_to_polar3d(x, y, z)               -- Convert cartesian coords into polar coords
103         local new_el = 90 + ang * (2*rand()-1)                         -- Randomise elevation angle: (90 +- ang)
104         local new_az = 90 * (2*rand()-1)                               -- Randomise azimuth angle: (0 +-90)
105         local x, y, z = polar3d_to_rect3d(speed, new_az, new_el)       -- Convert back to rectangular velocity components.
106         x, y, z = elevation_rotate(-90 + el, x, y, z)                  -- Rotate back to defined elevation.
107         return azimuth_rotate(az, x, y, z)                  -- Rotate back to defined azimuth.
108 end
109
110 function create_ionfile(i, da)          -- Copies the fly2 definitions file used for this run and saves it under a new name
111     local f, n = create_file(3, da)
112     for line in io.lines(i) do
113         f:write(line)
114     end
115     f:close()
116     return n
117 end
118
119 function empty_table(n)
120     for x=1,n,1 do
121         local t = { }
122         t[x] = 0
123     end
124     return t
125 end
```

B.3   Batch Scripts

SIMION can be run in batch mode, if the software is called using Lua (which itself must run inside a handling program[1]). The following scripts facilitate the unattended conversion of CAD data to PA files and also the sequential running of multiple instances of SIMION, in cases where different electrode geometries required the complete reloading of a workbench. These codes significantly reduced the need for the system to be attended, were able to monitor and log errors, and can easily be reused in the future for other not necessarily beamline-specific simulations, carried out using SIMION.

```lua
1  -- Start SIMION in lua interactive mode, and use commands stored in SIMION_batch_flym.lua
2
3  commandstring = [[C:\simion.exe lua SIMION_batch_flym.lua]]
4  os.execute(commandstring)
```

```lua
1  -- Batch STL2PA conversion, followed by refine in SIMION
2  -- Must be run in same root folder as simion.exe and sltools.exe
3
4  path = [[C:\test\]]
5
6  function refinepa(file)
7      commandstring = [[C:\simion.exe refine --convergence=1E-3 ]] .. path .. file       -- can change refine convergence here
8      return os.execute(commandstring)
9  end
10
11 function stl2pa(file)
12     commandstring = [[sltools.exe stl2pa --scale 1.0 --quickview 0 --nogui ]] .. path .. file
13     os.execute(commandstring)
14 end
15
16 for filenumber=1951,2241,10 do              -- stl files should be sequentially numerically numbered
17
18     filename = filenumber .. "_%.STL"
19     stl2pa(filename)
20
21     filename = filenumber .. "_.PA#"
22
23     z = refinepa(filename)
24     if z==0 then
25         print("Refine successful")
26     elseif z==1 then
27         print("Refine failed")
28     end
29 end
```

---

[1]SciTe http://www.scintilla.org/SciTE.html, an open-source code editor, was used as the coding and run-time environment.

```lua
-- Run multiple workbench simulations in SIMION (Batch mode)

simion.import("SIM_funct_lib.lua")          -- Imports lua file of functions called in this program

date = format_date(os.date("*t"))
path = [[C:\test\]]                          -- Change to appropriate path where .iob files are found
logfile = create_file(4, date)

function runflym(file)
    commandstring3 = "fly " .. path .. file
    simion.command(commandstring3)

end

for s=1,10,1 do
    for filenumber=1971,2211,240 do

        filename = filenumber .. "_.iob"
        printx("Attempting to start fly'm: " .. filename, 1)
        z = runflym(filename)
        if z==0 then
            printx("Fly'm successful", 1)
        elseif z==1 then
            printx("Fly'm failed", 1)
        end
    end
end
```

Appendix C

Formalities

C.1 Acknowledgements

Figure C.1: EBIT Group Seminar, November 2008, Xonrupt-Longemer, France.

C.2 Description of Work Completed

The design and fabrication of the components of the beamline had already been completed before I started my work. The beamline was designed by Rainer Ginzel, a PhD student of the Max-Planck-Institut, team leader for the deceleration beamline, and responsible for training me in preparation for the project.

Rainer Ginzel, Patrick Mrowcynski and myself were then responsible for the subsequent assembly and installation of the new experiment. A significant proportion of the preparation and assembly of the beamline was completed by myself. Minor roles, such as designing custom power supply units for the ion optical system were also performed. The detector electronics, including the threshold triggers were fine tuned by myself after guidance from José Crespo.

Ion trajectory simulations, conducted using SIMION, and all Lua code were written by myself specifically for this project. The electrode geometries for the simulation were created using beamline CAD data from Rainer Ginzel.

All performance tests was carried out alone, and this included the full preparation of the EBIT - energising the system, tuning the electron beam emission and injection of argon, followed by the extraction of and separation of ion species from the trap. For the charge exchange experiments extraction was completed together with Rainer Ginzel.

Upon completion of the testing, charge exchange experiments with Ar^{18+} and Ar^{17+} ions onto a neutral argon gas target were carried out together with Rainer Ginzel and Patrick Mrowczynski. The spectra presented here, including all calibration data, were calculated by myself for this project, with support from Rainer Ginzel in constructing the Gaussian fits. The two hardness ratios given were calculated together with Rainer Ginzel. Interpretations of the coincidence data drew from group discussions, supported by my own calculations.

Stuart Higgins
Heidelberg, June 2009.

Bibliography

[ABR+08] F. I. Allen, C. Biedermann, R. Radtke, G. Fussmann, and S. Fritzsche. Energy Dependence of Angular Momentum Capture States in Charge Exchange Collisions Between Slow Highly Charged Argon Ions and Argon Neutrals. *Physical Review A (Atomic, Molecular, and Optical Physics)*, 78(3):032705, 2008.

[Arn08] L. Arntzen. PSD - Some Remarks. Internal document with details of the Position Sensitive Detector used at the Heidelberg EBIT, July 2008.

[Aum09] F. Aumayr, 2009. Private communication.

[B+03] P. Beiersdorfer et al. Laboratory Simulation of Charge Exchange-Produced X-ray Emission from Comets. *Science*, 300:1558–1559, June 2003.

[Bea67] J. A. Bearden. X-ray Wavelengths. *Rev. Mod. Phys.*, 39(1):78, Jan 1967.

[Bei08] P. Beiersdorfer. A "Brief" History of Spectroscopy on EBIT. *Can. J. Phys.*, 86:1–10, 2008.

[BMN86] J Burgdöfer, R Morgenstern, and A Niehaus. Angular Momentum Distribution in the Classical Over-Barrier Model for Electron Capture into Highly Charged Slow Projectiles. *Journal of Physics B: Atomic and Molecular Physics*, 19(14): L507–L513, 1986.

[Bru05] H. Bruhns. *High Precision X-ray Spectroscopy on Highly Charged Argon Ions*. PhD thesis, Ruprecht-Karls-Universität Heidelberg, Heidelberg, Germany, 2005.

[BS03] H. F. Beyer and V. P. Shevelko. *Introduction to the Physics of Highly Charged Ions*. Institute of Physics Publishing, Bristol, UK, first edition, 2003.

[C+09] J. T. Costello et al., editors. *Recent Activities at the Tokyo-EBIT 2009*, Dublin City University, Ireland, 2009. Physics at EBITS and Advanced Research Light Sources (PEARL) 2009 Workshop, Dublin City University.

[CL78] M. Cardona and L. Ley, editors. *Photoemission in Solids I: General Principles*. Springer-Verlag, Berlin, 1978.

[CM91] A. Cerezo and M.K. Miller. Einzel Lenses in Atom Probe Designs. *Surface Science*, 246(1-3):450 – 456, 1991.

[Cra02]   T. E. Cravens. X-ray Emission from Comets. *Science*, 296:1042–1045, May 2002.

[Cur00]   F. J. Currell. The Physics of Electron Beam Ion Traps. In John Gillaspy, editor, *Trapping Highly Charged Ions : Fundamentals & Applications*, pages 28–30. Nova Science Publishers, 2000.

[DET97]   Konrad Dennerl, Jakob Englhauser, and Joachim Trumper. X-ray Emissions from Comets Detected in the Röntgen X-ray Satellite All-Sky Survey. *Science*, 277(5332):1625–1630, 1997.

[DGB+85]   D Dijkkamp, Yu S Gordeev, A Brazuk, A G Drentje, and F J de Heer. Selective Single-electron Capture into (n, l) Subshells in Slow Collisions of C6+, N6+, O6+ and Ne6+ With He, H2 and Ar. *Journal of Physics B: Atomic and Molecular Physics*, 18(4):737–756, 1985.

[DJM07]   D. A. Dahl D. J. Manura. SIMION 8.0 User Manual, March 2007.

[Don97]   E D Donets. 25 years with EBIS. *Physica Scripta*, T71:5–8, 1997.

[Epp07]   S. Epp. *Röntgen-Laserspektroskopie Hochgeladener Ionen in einer EBIT am Freie-Elektronen-Laser FLASH*. PhD thesis, Ruprecht-Karls-Universität Heidelberg, Heidelberg, Germany, 2007.

[G+04]   J. Geiss et al. The Apollo SWC Experiment: Results, Conclusions, Consequences. *Space Science Reviews*, 110:307–335(29), January 2004.

[Gin09]   R. Ginzel. Design of an Ion Deceleration Platform for the Investigation of Slow Ion-Surface Interactions and Ion-Atom Collisions. In *DPG Verhandlungen*, March 2009. Deutsche Physikalische Gesellschaft.

[Gre09]   Jason Greenwood. Electrostatic Charged Particle Optics. Private communication., March 2009.

[GWSC01]   J. B. Greenwood, I. D. Williams, S. J. Smith, and A. Chutjian. Experimental Investigation of the Processes Determining X-ray Emission Intensities from Charge-exchange Collisions. *Phys. Rev. A*, 63(6):062707, May 2001.

[HFB97]   V. P. Shevelko H. F. Beyer, H.-J. Kluge. *X-Ray Radiation of Highly Charged Ions*. Springer-Verlag, first edition, 1997.

[HT87]   G. Hubricht and E. Träbert. The Ar16+ 23S1 Lifetime from a Measurement on Recoil Ions. *Zeitschrift für Physik D Atoms, Molecules and Clusters*, 7:243 – 250, 1987.

[JN03]   P. Dauncey J. Nash. Introduction to C++. Internal document of Blackett Laboratory, Imperial College London, UK., September 2003.

[JW85]   R. K. Janev and Hannspeter Winter. State-selective Electron Capture in Atom-highly Charged Ion Collisions. *Physics Reports*, 117(5-6):265 – 387, 1985.

[KCK+02] V. A. Krasnopolsky, D. J. Christian, V. Kharchenko, A. Dalgarno, S. J. Wolk, C. M. Lisse, and S. A. Stern. X-Ray Emission from Comet McNaught-Hartley (C/1999 T1). *Icarus*, 160(2):437 – 447, 2002.

[KHH81] H. Knudsen, H. K. Haugen, and P. Hvelplund. Single-electron-capture Cross Section for Medium- and High-velocity, Highly Charged Ions Colliding With Atoms. *Phys. Rev. A*, 23(2):597–610, Feb 1981.

[KLR+09] D. Koutroumpa, R. Lallement, J. C. Raymond, , and V. Kharchenko. The Solar Wind Charge-transfer X-ray Emission in the 1/4 keV Energy Range: Inferences on Local Bubble Hot Gas at Low Z. *The Astrophysical Journal*, 696 (2):1517–1525, 2009.

[L+96] C. M. Lisse et al. Discovery of X-ray and Extreme Ultraviolet Emission from Comet C/Hyakutake 1996 B2. *Science*, 274(5825):205–209, October 1996.

[L+01] C. M. Lisse et al. Charge Exchange-Induced X-Ray Emission from Comet C/1999 S4 (LINEAR). *Science*, 292:1343–1348, May 2001.

[LMH+88] Morton A Levine, R E Marrs, J R Henderson, D A Knapp, and Marilyn B Schneider. The Electron Beam Ion Trap: A New Instrument for Atomic Physics Measurements. *Physica Scripta*, T22:157–163, 1988.

[LU09] J.R. Crespo López-Urrutia, 2009. Private communication.

[Mar05] A. González Martínez. *Quantum Interference in the Dielectronic Recombination of Heavy Highly Charged Ions*. PhD thesis, Ruprecht-Karls-Universität Heidelberg, Heidelberg, Germany, 2005.

[MEK94] R. E. Marrs, S. R. Elliott, and D. A. Knapp. Production and Trapping of Hydrogenlike and Bare Uranium Ions in an Electron Beam Ion Trap. *Phys. Rev. Lett.*, 72(26):4082–4085, Jun 1994.

[Mos09] R. Moshammer. Atomic and Molecular Reaction Dynamics, May 2009. Lecture course of the Max-Planck-Institut für Kernphysik, Heidelberg.

[Nie86] A Niehaus. A Classical Model for Multiple-electron Capture in Slow Collisions of Highly Charged Ions with Atoms. *Journal of Physics B: Atomic and Molecular Physics*, 19(18):2925–2937, 1986.

[OOB06] S. Otranto, R. E. Olson, and P. Beiersdorfer. X-ray Emission Cross Sections Following Charge Exchange by Multiply Charged Ions of Astrophysical Interest. *Physical Review A (Atomic, Molecular, and Optical Physics)*, 73(2): 022723, 2006.

[ORT07] ORTEC, 801 South Illinois Ave., Oak Ridge, TN 37831-0895 U.S.A. *IGLET and IGLET-X HPGe Detectors for Low and Very-Low Energy X Rays*, 1.0 edition, November 2007. Specification datasheet for the X-ray detector.

[RI06] W. Celes R. Ierusalimschy, L. H. de Figueiredo. *Lua 5.1 Reference Manual*. Lua.org, first edition, 2006.

[RKR09]   Yu. Ralchenko, A.E. Kramida, J. Reader, and NIST ASD Team (2008). NIST
           Atomic Spectra Database. Online, June 2009.

[Roe09]   RoentDek Handels Gmbh, Kelkheim-Ruppertshain, Germany.   *MCP Delay
           Line Detector Manual*, 9.17.905.2 edition, 2009.

[RSW80]   Hiroshi Ryufuku, Ken Sasaki, and Tsutomu Watanabe. Oscillatory Behavior
           of Charge Transfer Cross Sections as a Function of the Charge of Projectiles
           in Low-energy Collisions. *Phys. Rev. A*, 21(3):745–750, Mar 1980.

[Sep67]   A. Septier, editor. *Focusing of Charged Particles*. Academic Press, Inc., 1967.

[Tra05]   E Trabert. Spectroscopy of Argon Excited in an Electron Beam Ion Trap.
           Physica Scripta, 72(6):C42–C50, 2005.

[Vac08]   Pfeiffer Vacuum. Working with Turbopumps: Introduction to High and Ultra
           High Vacuum Production. Technical report, Pfeiffer Vacuum, 2008.

[WBB08]   B.J. Wargelin, P. Beiersdorfer, and G.V. Brown. EBIT Charge-exchange Mea-
           surements and Astrophysical Applications. *Can. J. Phys.*, 86:151–169, 2008.